Robotics and Media Institute (RMI)

To be the world leader in tangible media and robotics research

Wearable Robotic System
for People with Arm Weakness.

Microsurgical Robot
for Endonasal Skull Base Surgery

Exploratory Research
on Developing a Korean Lunar Rover

Augmented Reality

CAS

RMI Flagship Program : CAS4X   ($65M, KIST, 2015~2017)

CAS is defined as a human-centered smart and active space for future living, which improves the quality of life. CAS allows effective connections and interactions among humans, robots, smart devices and their environments by introducing advanced robotic, media and IC technologies.

Leading to the world of tomorrow

KISToday

Korea Institute of Science and Technology

Bio / Medical
- *Technical Review*
  Engineering of Biodegradable Mg Alloys: Tailoring the Electrochemical Properties and Microstructure of Constituent Phases
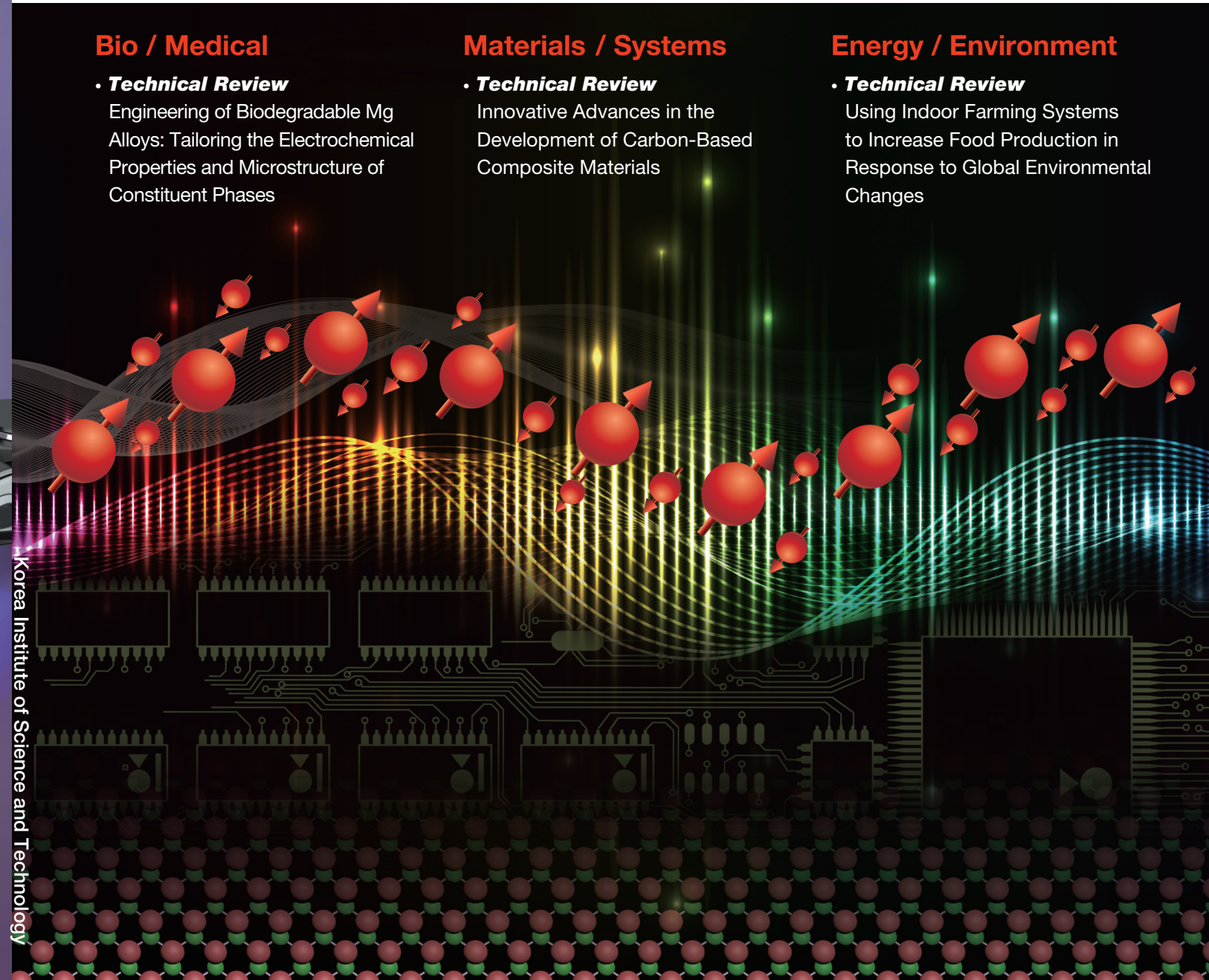
Materials / Systems
- *Technical Review*
  Innovative Advances in the Development of Carbon-Based Composite Materials

Energy / Environment
- *Technical Review*
  Using Indoor Farming Systems to Increase Food Production in Response to Global Environmental Changes

Korea Institute of Science and Technology

Contents

Foreword

In January 2015, two new research institutes were opened at KIST, the Post-Silicon Semiconductor Institute and the Robotics and Media Institute. As its name implies, the Post-Silicon Semiconductor Institute is leading the development of next-generation semiconductor devices and materials to move beyond the inherent limitations in silicon semiconductor technology. The Robotics and and Media Institute is at the center of developing robotic, media and ICT technologies which are expected to create new industries and re-invigorate existing ones.

The two institutes are already making remarkable progress in their fields by taking advantage of the synergy among existing research areas to create new research opportunities based on well-defined goals that support national economic policy initiatives. This edition's cover story on the technology to minimize signal loss of spintronic devices is a prime example of the groundbreaking research taking place at the Post-Silicon Semiconductor Institute. Similarly, the Robotics and Media Institute is attracting on notice for its research to develop a prototype for Korea's robotic exploration of the moon, technology to enjoy 3D visual effects without wearing glasses and technology to enable control of objects in virtual reality.

Korea is anticipating that its future economic growth will spring from R&D innovation. Government initiatives are designed to encourage innovation through strengthening strategic R&D investment while demanding the efficient use of these resources. In line with this government policy, KIST is fine-tuning and revamping its diverse systems to carefully plan its R&D projects in advance. KIST's research framework is now built around the broad fields of materials, systems, and bio/medical with efforts following clear national goals for R&D. Instead of a system segmented by single disciplines, research is increasingly multi-disciplinary, as exemplified by our two new institutes. This is one of the ways KIST is encouraging R&D innovation.

As we near our 50th anniversary, KIST is focusing on all out effort to develop original technologies. These types of innovative approaches will contribute to a strong nation and benefit the world at large.

Dr. Byung Gwon Lee
President of KIST

Engineering of Biodegradable Mg Alloys: Tailoring the Electrochemical Properties and Microstructure of Constituent Phases

Hyung-Seop Han

Center for
Biomaterials
hyuhan@kist.re.kr

Yu-Chan Kim

Center for
Biomaterials
chany@kist.re.kr

Hyun-Kwang Seok

Center for
Biomaterials
drstone@kist.re.kr

Introduction

Owing to their high strength, ductility, and good corrosion resistance, metallic materials such as stainless steels, titanium alloys, and cobalt-based alloys represent an important class of materials in hard tissue replacement. These materials are used as load-bearing implants for the repair or replacement of diseased or damaged tissues. These metallic materials are essentially neutral *in vivo* and remain inside the body after implantation as permanent fixtures, which must be removed by a second surgical procedure after the tissue heals sufficiently [1]. Additional surgery increases costs to the health care system and causes additional stress to the patient. Thus, a new domain of research in metallic implants focuses on biodegradable implants that can dissolve in the biological environment after a certain length of functional use. When applied as a biodegradable implant material, magnesium provides both biocompatibility and suitable mechanical properties.

Large amounts of Mg^{2+} are present in the human body. These ions are involved in many metabolic reactions and biological mechanisms, and excess Mg^{2+} is easily excreted via urine [2]. When compared to currently used implant materials, magnesium and magnesium-based alloys have a higher yield strength and a lower elastic modulus of about 45 GPa, which is close to that of natural bone (10–40 GPa). These characteristics provide magnesium-based alloys with the potential to avoid stress-shielding effects

[3-5]. Moreover, owing to its functional roles and presence in bone tissue, magnesium may actually have stimulatory effects on the growth of new bone tissue [6-10]. Thus, it is suggested that magnesium and its alloys can be applied as lightweight, degradable, load-bearing orthopedic implants that would remain in the body and maintain mechanical integrity over a time scale of 12–24 weeks while the bone tissue heals, eventually being replaced by natural tissue [11, 12]. Previous *in vivo* studies have shown that magnesium could be suitable as a degradable biomaterial for use in medical implants [13, 14].

However, some challenges prevent the practical use of biodegradable magnesium alloys. For example, commercial pure magnesium [15] and magnesium alloys can corrode too quickly at physiological pH (7.4–7.6) and under the high chloride conditions of the physiological environment. Rapid corrosion leads to the production of hydrogen gas in the corrosion process at a rate that is too fast for the host tissue to handle. Furthermore, such corrosion causes loosening of the mechanical integrity before the tissue can sufficiently heal [16-20]. Moreover, a much higher inherent strength of any developed alloys will be required because their strength would deteriorate gradually during the corrosion/degradation process [21]. Zhang et al. [21] reported that the bending strength of Mg-Zn alloy decreased rapidly during the initial corrosion stage, from about 625 MPa to 390 MPa with an approximately 6% loss of weight.

Zberg et al. [22] recently circumvented the above problems by using ternary Mg-Zn-Ca alloys in the form of bulk metallic glasses (BMGs). In their *in vitro* and *in vivo* degradation tests, these amorphous alloys showed tissue compatibility equivalent to that of their crystalline counterparts without clinically observable hydrogen production. Despite this, metallic glasses are brittle and particles can be released through wear processes, which might lead to antibody responses or inflammatory cascades, thereby reducing the overall biocompatibility [23-25]. Moreover, even though good cell viability has been reported in a cytotoxicity test [26], the high content of Zn in biodegradable Mg-Zn-Ca BMGs may be harmful to the human body [27, 28]. The sample dimension available for the formation of BMGs is also relatively small (on the order of several millimeters) when compared to their crystalline counterparts, which imposes a constraint on the application of Mg-Zn-Ca BMGs as biodegradable implants.

There have been several studies that considered crystalline Mg-Zn-Ca alloys as biodegradable implant materials [29-31]. However, they reported only limited phenomenological analyses, which showed that the macroscopic corrosion potential averaged over all constituent phases shifted to a more inert direction or that the ternary intermetallic compounds might be related to the increase of corrosion resistance. They could not find the optimal compositions of Mg-Zn-Ca alloys for clinical applications and failed to present any Mg based alloys with clinical significance. In this study, we developed new magnesium-based crystalline biomaterials with good mechanical properties and medically acceptable corrosion

Table 1. Actual compositions of the cast Mg-Ca-Zn alloys analyzed by ICP method.

Alloys	Ca (wt%)	Zn (wt%)	Mg (wt%)
Pure Mg	0	0	99.98 (Fe: 14ppm)
Mg-5wt%Ca	4.65	0	Bal.
Mg-5wt%Ca-0.5wt%Zn	4.62	0.50	Bal.
Mg-5wt%Ca-1.0wt%Zn	4.72	0.76	Bal.
Mg-5wt%Ca-1.5wt%Zn	4.51	1.63	Bal.
Mg-5wt%Ca-3.0wt%Zn	4.56	3.00	Bal.
Mg-5wt%Ca-5.0wt%Zn	4.65	4.12	Bal.

rates, which was achieved by tailoring the electrochemical properties and microstructure of constituent phases.

Preparation of the material

Commercially available pure Mg (99.98%) ingots, Ca (99.99%) metal grains, and Zn (99.99%) metal grains were used to prepare Mg-Ca and Mg-Ca-Zn alloys in a vacuum furnace. The atmosphere of the furnace was purged to 5 X 10^{-2} torr before high purity argon gas was applied (99.999%). The melting temperature was 750℃, and the melt was cast into a STS430 steel mold. The shape of each casting sample was a cylinder with a diameter of 50 mm and a height of 70 mm. The chemical compositions of the alloys (Table 1) were analyzed by the inductively coupled plasma (ICP) method. Mechanical extrusion was adopted for the microstructural tailoring. To accomplish this, the as-cast ingots were preheated to ~350℃ and then extruded into rods with an extrusion ratio of 25:1, after which the samples were cooled in air.

Immersion tests

Each sample used for the immersion test was machined to six plates (20 × 10 × 1.5 mm³), after which all of the surfaces were ground with SiC papers with up to 2000 grit. Each sample plate was immersed in Hank's solution with a pH of 7.4, which was controlled by HCl and NaOH and the pH was then allowed to change during the immersion test. The hydrogen evolution caused the water surface to descend with time in a funnel system. The amount of hydrogen evolution was measured by checking the variation in the height of the water surface with time.

As shown in Figure 1a, a hydrogen-evolution test revealed that increasing the Zn content generated a significant change in behavior. Specifically, Mg-5wt%Ca and Mg-5wt%Ca-0.5wt%Zn alloys featured strong gas evolution during degradation in Hank's solution, whereas increasing the Zn content to more than 1 wt% induced a remarkable reduction in the amount of hydrogen evolved, with the best corrosion resistance being observed at 1.5–3 wt%.
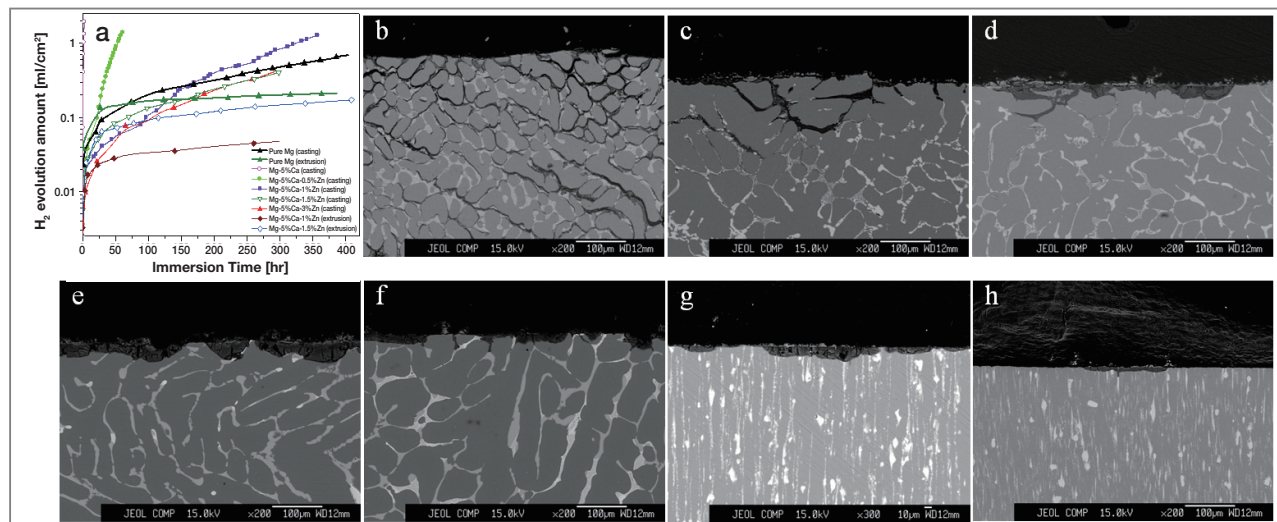
SEM observation

After the immersion test, the corroded samples were mounted using a mixture of resin and hardener. After hardening, the specimens were polished using 0.25 µm diamond powder and anhydrous ethanol (99.98%). The microstructures of the corroded samples were then observed by electron probe micro analyzer (JEOL JXA-8500F).

Figures 1b–f show the scanning electron microscopy (SEM) images of Mg-5wt%Ca-xwt%Zn alloy samples (x = 0, 0.5, 1, 1.5, 3) after the immersion test in Hank's solution. As shown in Figure 1a, severe corrosion of the Mg-5wt%Ca alloy occurred immediately upon immersion into Hank's solution.

The microstructure of the Mg-5wt%Ca binary alloy is composed of a primary Mg phase and an eutectic phase, which is a lamella structure composed of Mg and Mg_2Ca phases. A galvanic circuit forms when the alloy is immersed into Hank's solution owing to differences in the electro-chemical potentials of the Mg and Mg_2Ca phases. This galvanic circuit leads to swift and selective corrosion of the Mg_2Ca phase. The corroded microstructure shown in Figure 1b demonstrates this corrosion mechanism. This type of non-uniform corrosion can result in disintegration of the alloy or deterioration of its mechanical strength during the corrosion period.

As shown in Figure 1c, the selective corrosion of the Mg_2Ca phase caused by formation of the galvanic circuit was remarkably suppressed by the addition of a small amount of Zn. The addition of 0.5 wt% Zn modified the microstructure significantly. Specifically, the microstructure composed of primary Mg and eutectic phases changed to a mixture of primary Mg and Mg_2Ca (not lamella structure) with dissolved Zn. Mg_2Ca phases were disconnected at some places, whereas all eutectic structures in the Mg-Ca binary alloy were connected. Owing to the disconnected Mg_2Ca distribution and dissolved Zn, the selective corrosion of the Mg_2Ca phase was remarkably reduced.

When the Zn content increased to more than 0.5 wt%

(see Figures 1d-f), almost no corrosion occurred during the ~300 hours immersion test and the corrosion rates were comparable or lower than that of high purity Mg. This is the first reported observation of multi-phase Mg alloy with comparable corrosion resistance to that of high purity Mg. It is interesting to note that the Mg-Ca-Zn alloys did not experience pitting corrosion, which is a typical corrosion mode of Mg alloys. Rather, uniform and flat corrosion was observed, which implies that the alloys are free of abrupt disintegration and deterioration of mechanical strength during the corrosion/degradation process. The microstructures of as-cast Mg-Ca-Zn alloys with more than 1 wt% Zn did not differ greatly from that of the alloy with 0.5 wt% Zn, except for the white contrast phases connected by the Mg2Ca phases. X-ray diffraction analysis and wavelength dispersive spectroscopy (WDS) map analysis revealed that the white contrast phase was $Mg_6Ca_2Zn_3$ intermetallic compound. The volume fraction of this intermetallic compound increased as the Zn content increased. However, the corroded SEM images (Figures 1d-f) demonstrated that, rather than the $Mg_6Ca_2Zn_3$ intermetallic compound blocking the corrosion, the Mg_2Ca phase with dissolved Zn was not corrosive.

As shown in Figure 1a, the effect of extrusion on the corrosion rate was significant. The corrosion rate of extruded Mg-5wt%Ca-1wt%Zn alloy was much lower than that of high purity Mg, which was also confirmed by weight loss measurements. Figures 1g and 1h show the corroded microstructures of the extruded Mg-5wt%Ca-0.5wt%Zn and Mg-5wt%Ca-1wt%Zn alloys after being subjected to the immersion test for 299 hours and 408 hours, respectively. Despite these long immersion times, a flat corrosion surface persisted after a slight initial corrosion. There are various studies reporting that the corrosion rate of the Mg decreases with decreasing grain size [32]. The average grain size of the pure Mg was refined to ~25 µm by the extrusion whereas that of Mg-5wt%Ca-1wt%Zn alloy reduced to ~10 µm. Effective grain refinement of the ternary alloy was induced by the

Figure 1. Corrosion and corrosion microstructure measurements of crystalline Mg-Ca-Zn alloys. a. Hydrogen-evolution measurements showing a distinct drop in response to the addition of Zn and by mechanical extrusion. b–f. SEM images of Mg-5wt%Ca-xwt%Zn alloy samples (x = 0, 0.5, 1.0, 1.5, 3.0) after the immersion test in Hank's solution. g, h. SEM images of extruded Mg-5wt%Ca-xwt%Zn alloy samples (x = 0.5, 1.0) after the immersion test in Hank's solution.

particle pinning effect of the second phase and caused a larger drop of its corrosion rate compared to high purity Mg.

Work function calculation and WDS analysis

Density functional theory (DFT) calculations using the VASP program packages were used. The plane wave basis expansions with an energy cutoff of 300 eV and the generalized gradient approximation (GGA) with the PW91 exchange-correlation functional were used. The core-valence interaction is described by the projector-augmented wave (PAW) method. We constructed a Mg_2Ca slab structure with 96 Mg atoms and 48 Ca atoms to calculate work function. Vacuum sizes were given larger than 20 Å to minimize interaction between slabs. We first obtained the bulk Mg_2Ca structure applying Monkhorst-Pack sampling with a $8 \times 8 \times 4$ k-point grid and then constructed a slab structure with the resulting lattice constant and a $3 \times 3 \times 1$ k-point grid. The two-dimensional distribution of the Zn composition shown in Figure 2 was obtained by WDS analysis (JEOL JXA-8500F). The sample preparation was the same as that used for SEM analysis.

Figure 2 shows the SEM and the corresponding WDS images taken to investigate the distribution of the dissolved Zn. Non-uniform distribution of Zn was observed in the Mg ternary alloys with ≥ 0.5 wt% Zn (Figures 2b-d), which indicates that the dissolved Zn content is out of and within the solubility limit in the primary Mg and Mg_2Ca, respectively. In the SEM images shown in Figures 2b-d, dark gray indicates primary Mg and white reflects Mg_2Ca phase. Figure 2e shows the relationship between the biodegradation rate of the Mg-Ca-Zn alloys and the Zn concentration inside the Mg_2Ca phase obtained from WDS analysis. Obvious inverse proportionality was observed, which implies that the addition of Zn to Mg_2Ca prevents non-uniform corrosion by the formation of the galvanic circuit, that is, the addition of Zn to Mg_2Ca increases the corrosion potential of the Mg_2Ca phase. This is also supported by measurements of the open-circuit potential (OCP) of the immersed alloys.

OCP measurement

To understand the biodegradation behavior of each phase in the Mg-Ca-Zn alloy, the OCP of pure Mg (99.98%), Mg_2Ca, and $Mg_2Ca(Zn)$ was measured using the Autolab-GPES Version 4.8 corrosion measurement system. The sample preparation was the same as for the fabrication of Mg alloys described above, and Mg_2Ca samples with Zn were fabricated from Mg_2Ca ingot custom-made from R&D Korea. The chemical compositions of the samples were then determined by inductively coupled plasma (ICP, ARIAN 710-ES) analysis.

As shown in Figure 2f, the pure Mg is nobler (OCP versus standard hydrogen electrode (SHE) ≈ -1.58 V) than Mg_2Ca (OCP versus SHE ≈ -1.87 V), which demonstrates the non-uniform and rapid corrosion along Mg_2Ca by the formation of the galvanic circuit. However, the addition of Zn to Mg_2Ca pushed the OCP of Mg_2Ca up to that of the pure Mg, which prevented selective corrosion along the Mg_2Ca and induced the uniform corrosion seen in Figures 1d-f. The change in the work function of Mg_2Ca with Zn contents was investigated by using the first principle calculation to qualitatively understand the OCP increase of Mg_2Ca with Zn contents. It has been reported that the corrosion potentials of metals are proportional to their work functions [33] though they are a mixed potential and a function of various factors such as chemicals in Hank's solution, complexes of positive ions and so on. Figure 2g shows the variation of the work function with Zn contents for the (0001) surface of Mg_2Ca with lowest surface energy. The inset shows the atomic configuration of the (0001) surface. The work function of Mg_2Ca in the most stable (0001) surface is 3.16 eV, which is lower than that of pure Mg, say, 3.7 eV. This is consistent with OCP measurement where pure Mg has higher OCP than Mg_2Ca. The results also imply that the Zn atoms on the Mg_2Ca surface induce the increase of its work function, which is consistent with the OCP increase of Mg_2Ca with Zn concentration.

Radiographic analysis

Upon approval from the Animal Care and Use Committee of Chungnam National University, in vivo hydrogen evolution caused by the corrosion of newly developed magnesium alloys was investigated using eight adult male Sprague-Dawley rats weighing approximately 400 g (Orient Bio, Gyunggi, South Korea). Rats were anesthetized with 0.8 ml ketamine with 0.01 ml lumpun. Four types of 1 mm thick, 5 mm wide, and 20 mm long plates (cast and extruded Mg-5wt%Ca and Mg-5wt%Ca-1wt%Zn alloys) were implanted into the dorsal abdominal region. Daily observations were made and radiographic examinations of gas pockets were conducted at weeks 4 and 12.

Histological analysis

The in vivo evaluations, including histological analysis and micro-computed tomographic analysis, were performed at AccelLab (Quebec, Canada) in compliance with 21 CFR part 58 (FDA) Good Laboratory Practice for
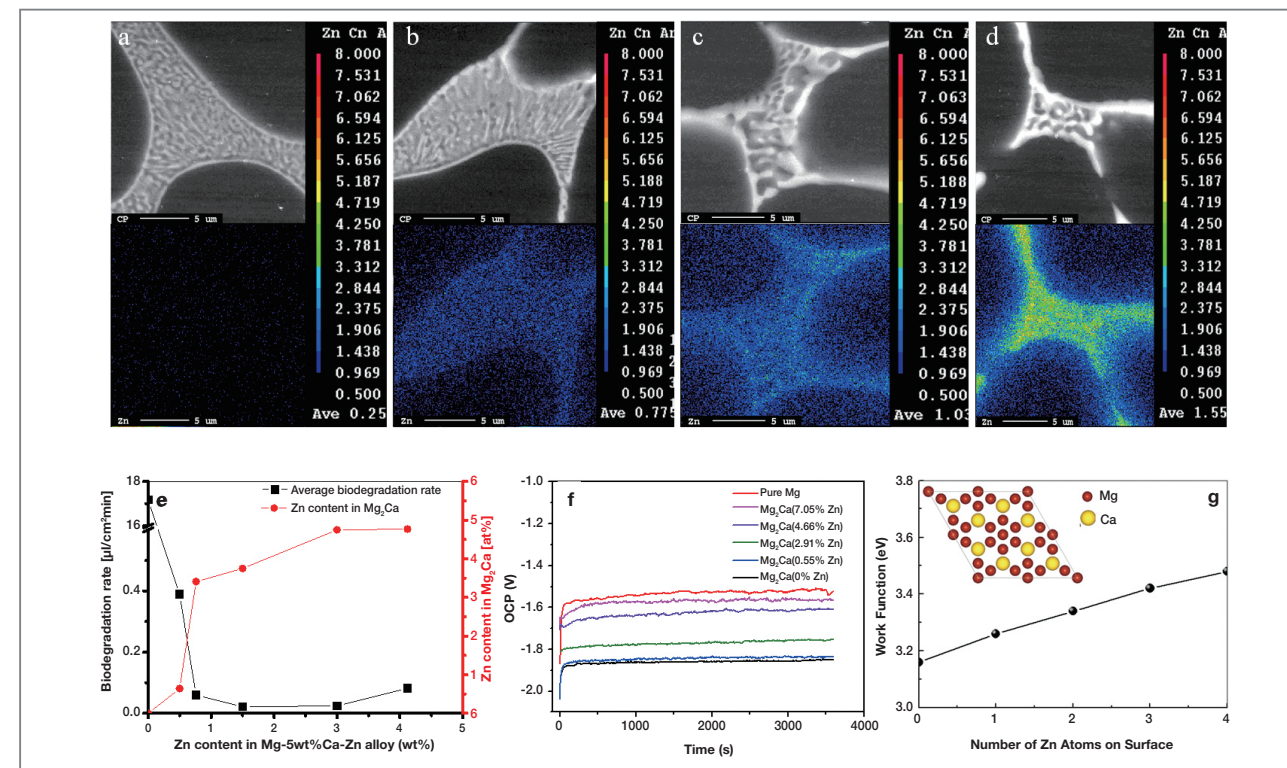

Figure 2. a–d. SEM and the corresponding WDS images showing the distribution of dissolved Zn in Mg-5wt%Ca-xwt%Zn alloys (x = 0, 0.5, 1.0, and 1.5 from the left). e. Relationship between the biodegradation rate of Mg-Ca-Zn alloys and the Zn concentration inside Mg_2Ca obtained from WDS analysis. f. Measurement of the open-circuit potential (OCP) of the immersed Mg_2Ca alloys with various Zn concentrations. g. Variation of the work function with Zn contents in the (0001) surface of Mg_2Ca (Inset. Atomic configuration of the (0001) surface where red spheres represent Mg atom and gold spheres represent Ca atom).

Nonclinical Laboratory Studies. Histological analysis was carried out to investigate the performance of the newly developed biodegradable Mg alloy screw of 2mm in outer diameter and of 10mm in length *in vivo* for 24 weeks. Twenty-one New Zealand white rabbits were assigned for this study and all animals received a bilateral implantation of Mg alloy screw in the femoral condyle. Animals were sacrificed at 24 weeks after the operation and the distal portions of the femurs containing the implantation sites were harvested and fixed in 100% ethanol. The bone blocks comprising the implant sites were processed, infiltrated with Technovit 7200, and polymerized. After embedding, the blocks were cut adjacent to the implant material by sawing along the longitudinal axis of the sample and sections were stained with Toludine blue.

Micro-computed tomographic analysis

Bone blocks from the histological study comprising implant units and surrounding bone were scanned using Skyscan Micro CT equipment. Images were used to
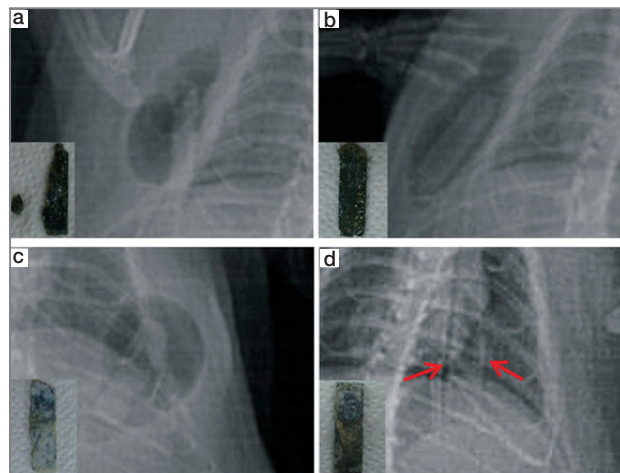

Figure 4. Histological analysis of extruded Mg-5wt%Ca-1wt%Zn alloy bone screw in femoral condyle of New Zealand white rabbit using Toludine blue staining at 24 weeks after operation. a. 3 x magnification. b. 10 x magnification. Insets: The cross sectional diagram (left) and finalized sample (right) of Mg-5wt%Ca-1wt%Zn alloy bone screw before implantation.

reconstruct a 3-D image of the implant unit and the long axis of the implant was aligned perpendicularly to the axis of the X-ray beam.

Animal experiments were performed in the dorsal abdominal region of eight adult male Sprague-Dawley rats to evaluate hydrogen evolution *in vivo*. Extruded Mg-5wt%Ca and cast and extruded Mg-5wt%Ca-1wt%Zn plates, together with a reference Mg-5wt%Ca cast alloy, were implanted in the rats and analyzed after 1, 2, 4, 8 and 12 weeks, respectively. Figure 3 shows the hydrogen evolution of Mg-Ca-Zn and Mg-Ca implants 12 weeks post-implantation. Rats implanted with cast and extruded Mg-Ca and cast Mg-Ca-Zn plates showed clinically and radiographically visible gas bubbles (Figures 3a-c). The gas bubbles were formed within the first week after surgery and persisted for the entire 12 week period. Rats implanted with extruded Mg-Ca-Zn plates did not show any visible gas bubbles clinically or radiographically (Figure 3d). Accordingly, there were no adverse effects caused by the gas bubbles.

The results from the series of extensive animal model studies has demonstrated the possibility of developed Mg-5wt%Ca-1wt%Zn extruded alloy as next-generation biodegradable orthopedic material. Histologic analysis (Figure 4a) of extruded Mg-5wt%Ca-1wt%Zn alloy bone screws implanted on the femoral condyles of New Zealand white rabbits for 24 weeks demonstrated new

Figure 3. X-ray images of hydrogen bubble pockets at 12 weeks after the implantation of Mg-Ca-Zn and Mg-Ca alloy samples into the dorsal abdominal region of eight adult male Sprague–Dawley rats. a. Cast Mg-5wt%Ca. b. Extruded Mg-5wt%Ca. c. Cast Mg-5wt%Ca-1wt%Zn d. Extruded Mg-5wt%Ca-1wt%Zn. Insets: The corresponding corroded implants removed from the rats at 12 weeks after implantation.
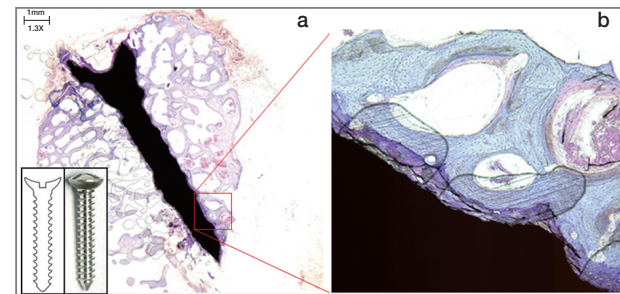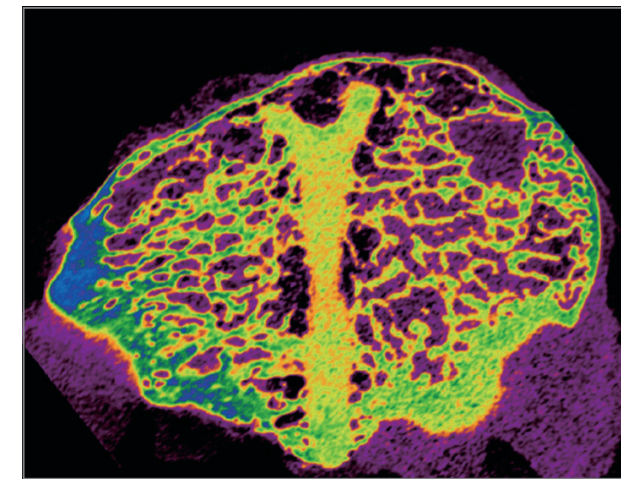

Figure 5. Micro-computed tomographic image of extruded Mg-5wt%Ca-1wt%Zn alloy bone screw in femoral condyle at 24 weeks after operation.

bone formation and bone remodeling without notable bubble formation and foreign body response around the implanted sample. An abundance of new bone depositions around the degraded bone screw was observed and a magnified image (Figure 4b) of the implantation site clearly displays active bone remodeling around the degraded implant sample. Further histomorphometric analysis of the slide confirmed a slight increase in the percentage of new bone with time, while the percentage of residual implants decreased. Micro-computed tomographic reconstruction image of the same specimen displayed similar characteristics. Superb direct bone deposition and new bone formation around the partly absorbed Mg-5wt%Ca-1wt%Zn alloy bone screw was observed after 24 weeks of implantation as shown in Figure 5. There was no adverse effect from the implant material and controlled slow corrosion rate of the alloy allowed the developed bone screw to remain in the implantation site while promoting direct new bone deposition and growth. Thus it is evident that new orthopedic implants made out of extruded Mg-5wt%Ca-1wt%Zn alloy will be slowly absorbed by the physiological surroundings while maintaining mechanical integrity over the implantation period until being completely replaced with new bone.

Conclusion

We identified a biodegradable Mg implant material that can reduce or control hydrogen evolution remarkably during *in vitro* and *in vivo* degradation. This effect was achieved by both microstructural and electrochemical tailoring; specifically, via a modified microstructure produced by mechanical extrusion and an increase in OCP of Mg_2Ca induced by dissolved Zn. The large reduction in hydrogen evolution to levels comparable to those of previously reported glassy Mg alloys [22] was shown in this study for the first time to represent a significant step toward the use of Mg in biodegradable implants. The further adequate tissue healing seen in conjunction with these alloys and their good mechanical properties indicate that the extruded Mg-5wt%Ca-xwt%Zn ($1 \leq x \leq 3$) alloys investigated are ideal candidates for biodegradable implant applications.

References

[1] Park JB, Bronzino JD. *Biomaterials: Principles and Applications* (Taylor & Francis, 2002).

[2] Saris NE, Mervaala E, Karppanen H, Khawaja JA, Lewenstam A. *Clinica Chimica Acta; International Journal of Clinical Chemistry* 2000; 294: 1-26.

[3] Ducheyne P, Hastings GW. *Functional Behavior of Orthopedic Biomaterials: Applications* (CRC Press, 1984).

[4] Davis JR. *Handbook of Materials for Medical Devices* (ASM international, 2003).

[5] Zhang E, Xu L, Yang K. *Scripta Materialia* 2005; 53: 523-527.

[6] Revell PA, Damien E, Zhang X, Evans P, Howlett CR. *Key Engineering Materials* 2004; 254: 447-450.

[7] Zreiqat H. et al. *Journal of Biomedical Materials Research* 2002; 62: 175-184.

[8] Yamasaki Y. et al. *Journal of Biomedical Materials Research* 2002; 62: 99-105.

[9] Yamasaki Y. et al. *Biomaterials* 2003; 24: 4913-4920.

[10] Li Z, Gu X, Lou S, Zheng Y. *Biomaterials* 2008; 29: 1329-1344.

[11] Witte F. et al. *Biomaterials* 2005; 26: 3557-3563.

[12] Wen C. et al. *Scripta Materialia* 2001; 45: 1147-1153.

[13] Hofmann G. *Archives of Orthopaedic and Trauma Surgery* 1995; 114: 123-132.

[14] Vormann J. *Molecular Aspects of Medicine* 2003; 24: 27-37.

[15] Atrens A, Liu M, Zainal Abidin NI. *Materials Science and Engineering*: B 2011; 176: 1609-1636.

[16] Staiger MP, Pietak AM, Huadmai J, Dias G. *Biomaterials* 2006; 27: 1728-1734.

[17] Song G. *Corrosion Science* 2007; 49: 1696-1701.

[18] Gu X, Zheng Y, Cheng Y, Zhong S, Xi T. *Biomaterials* 2009; 30: 484-498.

[19] Lambotte A. *Bull. Meˊm. Soc. Nat. Chir*. 1932; 28: 1325-1334.

[20] Troitskii V, Tsitrin D. *Khirurgiia* 1944; 8, 41-44.

[21] Zhang S. et al. *Acta Biomaterialia* 2010; 6: 626-640.

[22] Zberg B, Uggowitzer PJ, Löffler JF. *Nature Materials* 2009; 8: 887-891.

[23] Jacobs JJ, Hallab NJ, Skipor AK, Urban RM. *Clinical Orthopaedics and Related Research* 2003; 417: 139-147.

[24] Niki Y. et al. *Biomaterials* 2003; 24: 1447-1457.

[25] Ma E, Xu J. *Nature Materials* 2009; 8: 855-857.

[26] Gu, X. et al. *Biomaterials* 2010; 31: 1093-1103.

[27] Witte F. et al. *Current Opinion in Solid State and Materials Science* 2008; 12: 63-72.

[28] Isabel Post J, Karl Eibl J, Michiel Ross G. *Amyotrophic Lateral Sclerosis* 2008; 9: 149-155.

[29] Rad B. et al. *Applied Mechanics and Materials* 2012; 121: 568-572.

[30] Du H, Wei Z, Liu X, Zhang E. *Materials Chemistry and Physics* 2011; 125: 568-575.

[31] Zhang E, Yang L. *Materials Science and Engineering*: A 2008; 497: 111-118.

[32] Ralston K, Birbilis N. *Corrosion* 2010; 66: 075005-075005-075013.

[33] Yee S, Oriani R, Stratmann M. *Journal of the Electrochemical Society* 1991; 138: 55-61.

Polymers for Cell/Tissue Anti-Adhesion

Eugene Lih
Center for Biomaterials
eugene.lih@kist.re.kr

Yoon Ki Joung
Center for Biomaterials
ykjoung@kist.re.kr

Dong Keun Han
Center for Biomaterials
dkh@kist.re.kr

Introduction

Interfacial interactions between cell/tissue and polymers correlate with many important phenomena in biological systems and have been used to develop various artificial biomaterials and applications [1, 2]. While biomimetic materials that promote a favorable response from cells and tissues are required to fabricate scaffolds and implants for tissue engineering and regenerative medicine, bioinert polymers that suppress nonspecific adhesions that induce thrombosis and immunological responses are required for most biomedical devices and implants, such as blood- or tissue-contacting and biosensing devices [3, 4]. Cell anti-adhesion materials have been considered and developed for widespread applications such as cell sheet engineering, multicellular spheroid formation, cell encapsulation, and blood-contacting devices (Figure 1).

Tissue adhesion following surgery is one of the most common challenges in clinical practice [5]. Tissue adhesions commonly entail severe pain, functional obstruction of organs, and sometimes difficult reoperative surgery, which markedly increases healthcare costs [6]. Recently, tissue adhesion barriers that can physically isolate wounds, thus effectively preventing the formation of tissue adhesion, have been a hot topic in research as well as in industrial fields.
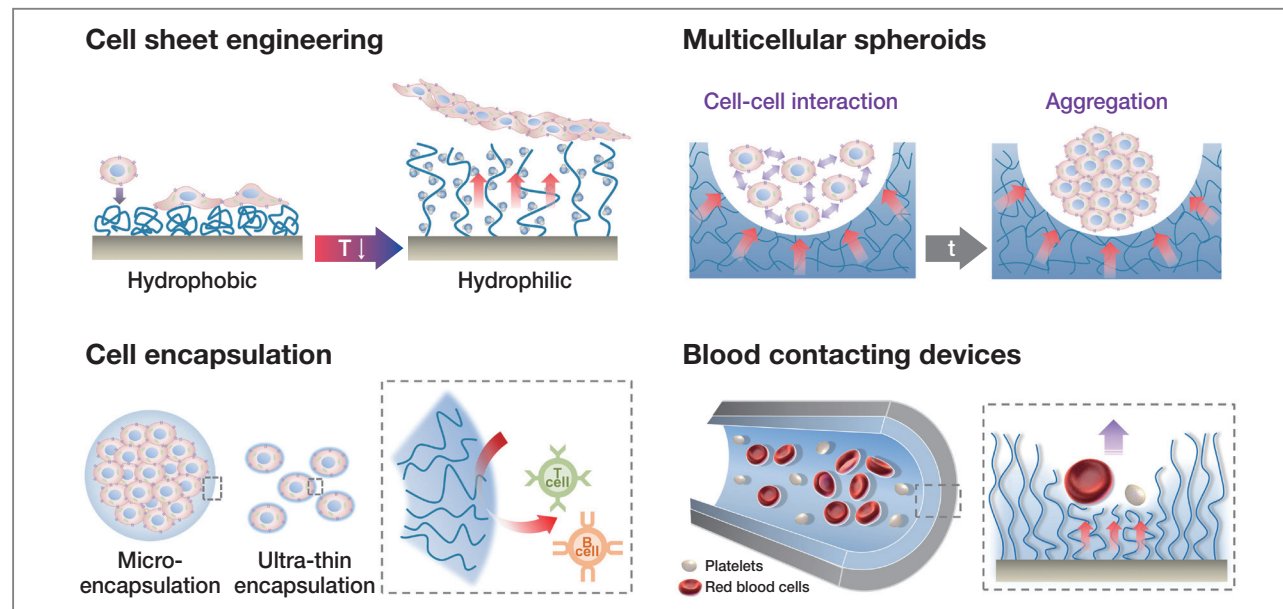
Figure 1. Biomedical applications of cell anti-adhesive polymers: cell sheet engineering, multicellular spheroids, cell encapsulation, and blood contacting devices.

Figure 3. (a) Schematic illustration of different methods for immobilizing polymer chains on solid surfaces: physisorption, "grafting-to" and "grafting-from" (surface initiated polymerization). (b) Basic designs of surfaces from homopolymer and mixed polymer brushes, films from functional particles, blockcopolymer films, layer-by-layer (LbL) films, hybrid (polymer and particles) films, crosslinked films, and membranes.

Polymers for cell anti-adhesion

Bioinert polymers such as polyurethane (PU), poly(tetrafluoroethylene) (PTFE), poly(dimethyl siloxane) (PDMS), polystyrene (PS), and poly(ethylene glycol) (PEG) were initially used as coating materials for blood-contacting medical devices. These surface modifications with polymer coating layers have been used to avoid uncontrollable interactions with cells and proteins in biomedical applications because protein adsorption and subsequent cell adhesion behavior are disadvantageous for the desired functions of these materials [1].

The mechanism of cell and surface interaction should be considered in the design of cell non-adhesive surfaces. When cells adhere to the surface of a material, a sequence of physicochemical reactions will happen between the cells and the material interface. Immediately after a biomaterial is implanted into an organism or comes into contact with cell culture environments, protein adsorption to its surface occurs, which mediates the cell adhesion and also provides signals to the cell through the cell adhesion receptors, mainly integrins [2]. Cells do not

interact directly with the surface but via proteins that they secrete, which are adsorbed on the surface adhesive, forming their own nonorganized layer [7]. Understanding the factors that influence cell adhesive ability is key in the development and application of cell anti-adhesion material.

Although cell adhesion is a complex process affected by numerous factors such as cell type and environmental factors, the surface physicochemical parameters known
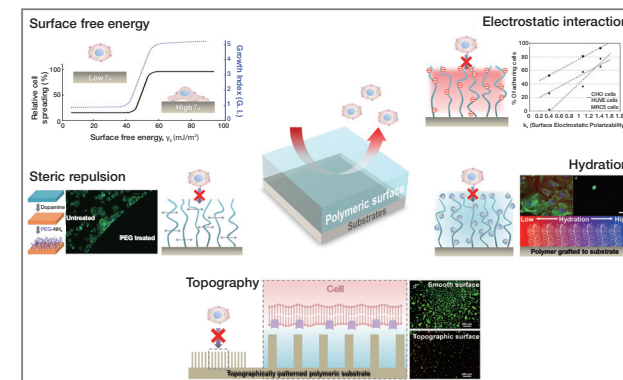

Figure 2. Schematic depiction of the different cell repellent models: electrostatic interaction, surface free energy, steric repulsion, hydration, and topography.
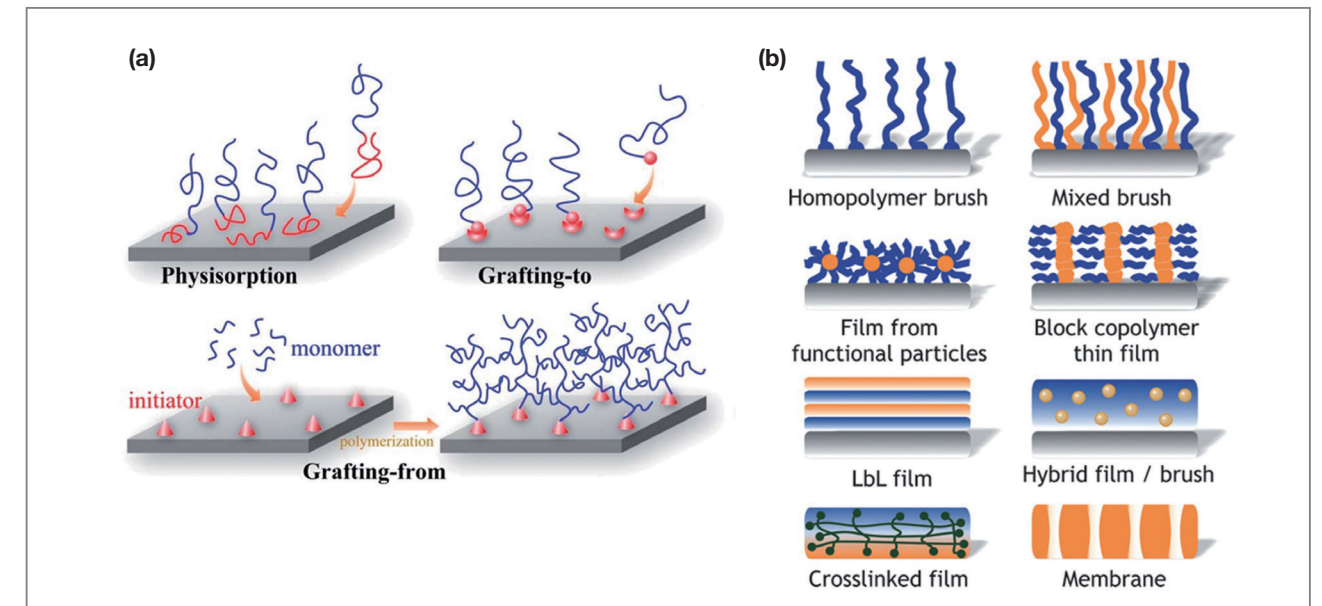
to influence the phenomenon can be summarized as follows [7]: surface free energy, electrostatic interactions, steric repulsion, hydration, and topography (Figure 2). Such surface design has been performed by thin coating, self-assembling, or physically/chemically grafting using several types of polymers (Figure 3).

Polymers for tissue anti-adhesion

Tissue adhesion is an undesirable result after surgery and is considered a big challenge in clinical fields [5]. It is well established that the formation of fibrous bands between injury sites and neighboring tissues or organs in response to trauma, infection, dehydration, ischemia, hemorrhage, and foreign bodies leads to tissue adhesion in many parts of the body [8, 9]. Pharmacological adjuvants such as nonsteroidal anti-inflammatory drugs (NSAIDs), corticosteroids, fibrinolytic agents, anticoagulants, antibiotics, antioxidants, hormones, anticancer drugs, vitamins, and growth factors have been considered as

effective strategies for tissue adhesion prevention (Figure 4).

Although a variety of surgical and pharmacological strategies to reduce tissue adhesion formation have been tried, the use of barrier materials that can physically isolate the injured tissues/organs during wound healing has been more extensively investigated and frequently applied in clinical fields. The essential requirements for ideal barrier materials are considered to be residence stability at the applied (injury) site during wound healing (7–10 days) without sutures or staples, the ease of handling in laparoscopic and open surgeries, biocompatibility, biodegradability, immunological inertness, and no interference in wound healing [10, 11]. To fulfill these criteria, numerous polymers have been adapted in various forms. The following section will discuss polymeric tissue adhesion barriers with different structures and functions such as sheet types, solution/hydrogel types, powder types, and controlled drug-releasing types of materials.

Recently, hydrogel-type barriers based on viscous, cross-linked, and *in situ* gel-forming synthetic or natural polymers have been extensively explored for
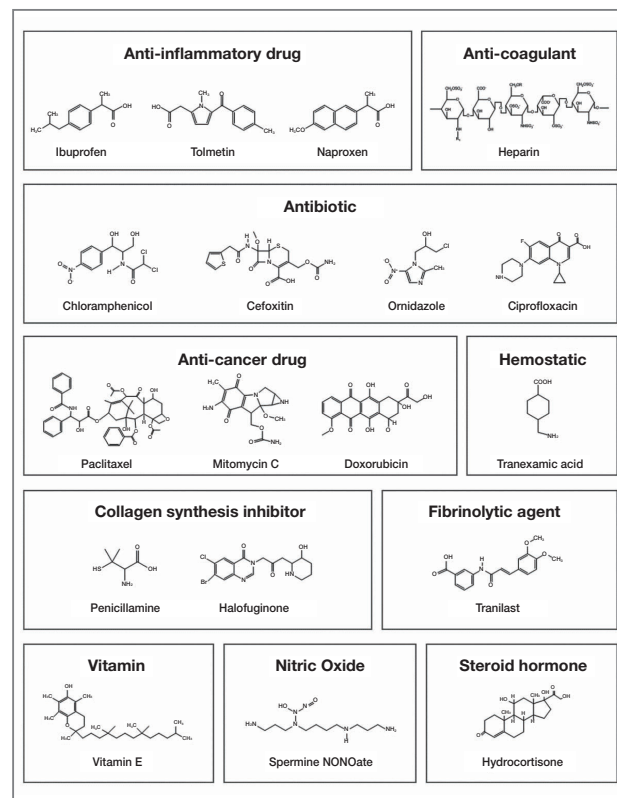
Figure 4. Chemical structures of representative pharmaceutical agents adapted in tissue adhesion barriers.
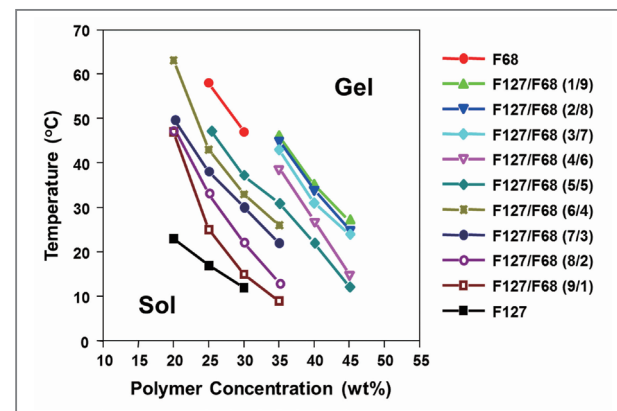

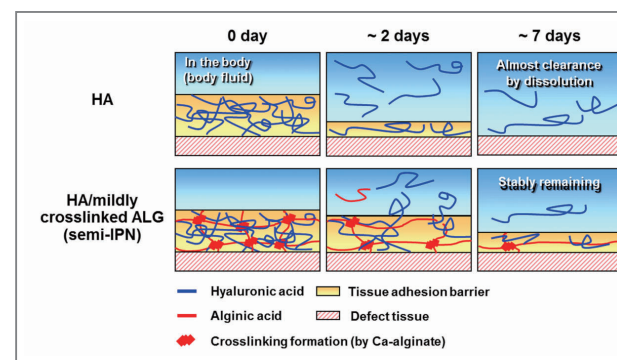Figure 5. Sol-gel transition behaviors of amphiphilic Pluronic F127/F68 mixtures.

Figure 6. Schematic diagrams showing the expected residence stability of HA solution and HA/mildly crosslinked ALG hydrogel (semi-IPN structure) in the body.

the prevention of adhesion formation as an alternative to the sheet type method. To prevent the flowing away of barriers from defect lesions, amphiphilic polymers (possessing both hydrophilic and hydrophobic properties) with thermosensitive properties (reversible sol-gel transition behavior) have been considered ideal materials. The amphiphilic polymer solutions are in a viscous liquid during application (≤ R.T.) and thus can be evenly coated on the injured sites. They change to a gel state within a few seconds in the body, and thus can firmly cover the injured tissue site without any of the solution flowing down (Figure 5). To compensate for the limitations of thermosensitive hydrogels composed of synthetic polymers, biodegradable hydrogels have been developed by using hyaluronic acid (HA), celluloses, alginate (ALG), chitosan, and their mixtures (Figure 6).

Conclusion and future perspectives

The development of biomaterials and surface coating methods for cell anti-adhesion is one of the emerging challenges for human applications in the biomaterial fields. Polymer properties such as surface free energy, electrostatic interaction, steric repulsion, hydration, and topography are widely utilized for effective cell anti-adhesion and applied in biomedical devices for diagnosis and therapy. The properties are generally assigned to biomedical devices individually or by combining at least two properties. Combination of molecular scale (surfaces grafted polymers) and nano/micro scale (topographical

structures) technologies has been used to significantly enhance the effect of cell anti-adhesion of polymeric substrates. The influence of the composition and structure of the polymeric surfaces on interactions with cells has been studied extensively and has been exploited to regulate the biological properties of biomaterials. Future developments may be achieved by utilizing peptide-blocking cell adhesion receptors, anti-integrin antibodies, and nitric oxide-inhibiting adhesion of platelets and proliferation of smooth muscle cells by activating guanylate cyclase. Moreover, the biofunctional polymers will make it possible to attach and detach a specific cell, e.g., adhesion of endothelial cells and anti-adhesion of smooth muscle cells in the re-endothelialization of stents.

Meanwhile, after the first report on tissue adhesion in an animal model in 1886, many strategies for the prevention of tissue adhesion formation, such as surgical techniques, pharmacological agent treatments, and various polymer barrier methods, have been investigated. However, finding ideal barriers still remains a big challenge. It is expected that the accumulation of experience and knowledge in laboratories and in clinical fields, as well as advanced technologies in biomaterials and drug delivery, might create reliable tissue adhesion barriers in the near future. It is also hoped that post-surgical tissue adhesions will no longer be troublesome in clinical practice.

The selection of a suitable polymer and methodology to impact effective anti-adhesion on a surface is of extreme importance in biomedical applications. The anti-adhesion approach utilizing polymers is a promising field, and it appears that these polymers will have increasing implications in the future.

Note

This article and images are drawn from "Polymers for cell/tissue anti-adhesion" in *Prog. Polym. Sci.*, 2015, Vol.44, pp.28~61.

References

[1] Nagase K, Kobayashi J, Okano T. *J. R. Soc. Interface* 2009; 6: S293-309.

[2] Vagaska B, Bacakova L, Filova E, Balik K. *Physiol. Res.* 2010; 59: 309-22.

[3] Worz A, Berchtold B, Moosmann K, Prucker O, Ruhe J. *J. Mater. Chem.* 2012; 22: 19547-61.

[4] Niepel MS, Peschel D, Groth T. *Int. J. Artif. Organs* 2011; 34: 185-91.

[5] Dunn R, Lyman MD, Edelman PG, Campbell PK. *Fertil. Steril.* 2001; 75: 411-6.

[6] Ray NF, Denton WG, Thamer M, Henderson SC, Perry S. *J. Am. Coll. Surg.* 1998; 186: 1-9.

[7] Vladkova TG. *Int. J. Polym. Sci.* 2010: 1-22.

[8] Yeo Y, Kohane DS. *Eur. J. Pharm. Biopharm.* 2008; 68: 57-66.

[9] Brüggmann D, Tchartchian G, Wallwiener M, Münstedt K, Tinneberg HR, Hackethal A. *Dtsch. Arztebl. Int.* 2010; 107: 769-75.

[10] Al-Musawi D, Thompson J. *Gynaecol. Endosc.* 2001; 10: 123-30.

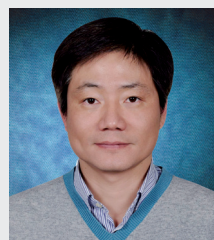[11] Risberg B. *Eur. J. Surg. Suppl.* 1997; 577(suppl): 32-9.

[**Feature Articles**]

Immunoassay of Oligomer Amyloid β with Magnetic Beads for the Diagnosis of Alzheimer's Disease

Jeong Ah Kim
Center for BioMicrosystem

Ji Yoon Kang
Center for BioMicrosystem
jykang@kist.re.kr

Introduction

Alzheimer's disease (AD) is a chronic, neurodegenerative disorder and a major cause of progressive dementia in the aged population. AD accompanies pathologic hallmarks by accumulation of extracellular amyloid plaques and intracellular neurofibrillary tangles, leading to neuronal degeneration. When clinical symptoms of dementia emerge, such as memory loss and functional decline, significant and irreversible brain damage has already occurred, and there is no cure. Therefore, early diagnosis of AD is an urgent prerequisite for therapeutic treatment and preventative therapies [1, 2].

Current diagnostic imaging techniques for AD, such as magnetic resonance imaging (MRI) and F-18 fluorodeoxyglucose positron emission tomography (FDT-PET) imaging, are sensitive for visible neuronal damage, but they are inadequate for early diagnosis because they are too expensive for use in conducting regular screening tests. Early diagnosis with body fluids is better suited for early diagnosis. Assays of phosphorylated tau (pTau) or amyloid beta (Aβ) from cerebrospinal fluid (CSF) have been demonstrated to be highly sensitive and selective, but they are not good candidate methods for early diagnosis due to the invasive lumbar puncture required for CSF sampling. Therefore, blood-based diagnosis is an attractive option, and many groups are trying to identify reliable biomarkers in blood [3]. It has been reported that soluble Aβ oligomers are toxic to neuronal cells and principle pathogenic species [4-6]. Therefore, oligomer Aβ is a potentially promising candidate biomarker for the diagnosis and pre-clinical prediction of AD, although the method used to measure its exact concentration is still controversial [7-9]. Some groups have used the same antibody-sandwich, enzyme-linked immunosorbent assays (ELISA) to detect oligomer Aβ in CSF [4, 5, 10]. Recently, a sandwich assay referred to as the multimer detection system (MDS) was developed in which two antibodies are used to target the same or overlapping epitope to detect oligomer prion protein in blood samples as well as oligomer amyloid β [11, 12]. This assay utilized a magnetic bead-based ELISA assay, and it had the advantages of utilizing less reagents and analyzing multiple samples for the detection of oligomer Aβ [13]. However, it is still labor-intensive and costly because it involves a multi-step process that includes mixing, blocking, incubation, and washing [14].

Microfluidic techniques have allowed the miniaturization of conventional ELISA for the development of point-of-care (POC) diagnostics [15–17]. The advantages of microfluidic devices include their portability and the small volume of samples and reagents required, the reduced likelihood of contamination, low cost, low power consumption, and enhanced sensitivity and reliability. Moreover, utilization of a microfluidic channel or magnetic nanoparticles for an ELISA assay can reduce the assay time significantly due to their high surface-to-volume ratio and small diffusion distance [16, 18-20]. Some microfluidic devices have micropumps and microvalves to control the fluid flow in a microfluidic chamber [14, 18], but this approach has disadvantages in that large and complex external equipment is required to operate them, impeding miniaturization and ease of commercialization. However, some groups have chosen the option of using stationary microfluidic systems in which a liquid droplet is fixed in an oil chamber, and magnetic beads move between the liquid droplets. Such magnetic droplet-based platforms have attracted greater attention than flow-based platforms for a variety of molecular diagnoses, purifications, and biological reactions [21-23]. The automatic manipulation of the moving magnet in droplet-based platforms simplifies the complicated assay procedures and reduces processing time because the reaction occurs in a tiny, compartmentalized droplet. The actuation of magnetic beads is required to ensure a controlled, reliable reaction because the entire motion of the magnetic droplet is affected by the mass of the beads, the handling speed of the magnet, and the surface properties of the chamber. Many groups have used their own unique approaches to separate aqueous droplets from the oil phase with magnetic force. They stabilized the water-oil interface and reduced cross-contamination or mixing between the two phases by modifying the hydrophobic or hydrophilic surface properties [15, 17, 21, 23, 24-26].

We developed a microfluidic device that contained micro-pillar structures for the magnetic bead-based MDS assay to detect oligomer Aβ that was previously developed on a 96-well plate. The MDS assay was developed with magnetic bead-based ELISA, and a manual, harsh, vortex washing step was required to reduce non-specific binding, which hinders the automation of the assay process. The microfluidic device provided gentle and effective washing using the droplet-based operation, and it was easy to automate for high-throughput diagnoses. This microfluidic device consisted of five chambers for holding aqueous reagents and oils, which create an immiscible barrier between the two different aqueous droplets. To confine the liquids stably during the ELISA assay, the micro-pillars were fabricated with specific features to improve the surface tension at the two-phase interface. These micro-pillars enhanced the operational flexibility and subsequently increased the reliability of results of the assay. We quantitatively analyzed the fluorescence signal depending on the concentration of oligomer Aβ. It was demonstrated that this device can be compatible with an ELISA protocol on a 96-well plate with ease of operation and a high probability of being able to automate the process.

Materials and methods

For the detection of oligomer Aβ using magnetic beads, we basically followed the slightly modified MDS protocol. For an assay, two different monoclonal antibodies (Covance, USA) targeting the overlapping epitopes in the N-terminus of human Aβ were used for their competitive reaction. One of the antibodies was conjugated with the magnetic beads as a capture bead for Aβ, and the other was conjugated with horseradish peroxidase (HRP) to detect Aβ and generate a fluorescence signal by an enzymatic reaction with the HRP substrate. For stable and reproducible assay of oligomer Aβ in this study, we used synthesized oligomer mimicking standard protein (OMSP), a stable synthesized molecule where several Aβ monomers are attached to an albumin preventing the aggregation of Aβ (donated by Prof. Ahn of Gachon University, Korea).

Basically, each chamber in a microchip was filled alternatively with water-based reagents and mineral oils (Figure 1). The first chamber (i) is for the loading and incubation of the antibody-conjugated magnetic beads with HRP-detection antibody and antigen (oligomer Aβ), and chamber (iii) is for the washing buffer (TBST); the last chamber (v) is for fluorescence detection after enzymatic reaction with its substrate. Chambers (ii) and (iv) contained a mineral oil solution for separating the water-based reagents. Diluted OMSP solution was added into the mixture of magnetic beads and HRP-detection antibody with an appropriate concentration (0-400 μg/mL) just before use. Then 7 μL of this mixture was pipetted into the first chamber through the inlet hole in the PMMA layer. The washing buffer and detection HRP substrate were used to fill the designated chambers, and finally, the rest of the chambers were filled with oil solutions. After finishing the antigen-antibody reaction, a cylinder-shaped magnet was placed on the bottom surface of the cover glass and then moved linearly toward the subsequent chambers. The magnetic beads were aggregated by the gradient of the magnetic field and then moved through the
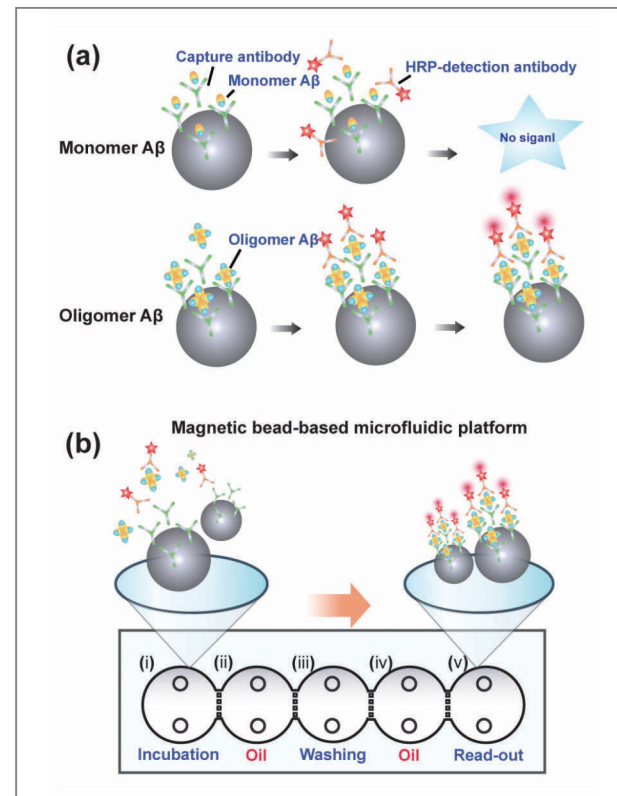

Figure 1. A simple principle of magnetic bead-based oligomer Aβ assay in a microfluidic device: (a) schematic drawing of the multimer detection system (MDS) for oligomer Aβ assay using magnetic beads. Overlapping N-terminal anti-Aβ monoclonal antibodies were used for both capture and detection. Monomeric species are not able to bind both capture and detect antibodies, but oligomer forms have two or more epitopes for antibodies, and they react with the HRP substrate, generating a fluorescence signal. (b) Chamber (i) is for the incubation of antigen, capture antibody-conjugated magnetic bead, and HRP-conjugated detection antibody. Chamber (ii) is for washing. Chambers (iii) and (iv) contain mineral oil for separating reagents. Chamber (v) is for the detection of signal, which contains the HRP substrate to produce red fluorescence through the HRP enzyme catalytic reaction.

chambers in order. In the washing chamber, the magnetic beads were rotated gently 10 times for about 1 min within a washing buffer by manual handling of the magnet. When the magnetic beads reached the read-out chamber, they also were rotated gently to disperse them in the HRP substrate with which they reacted, so that fluorescent products were mixed homogeneously. At 5 min after reaction with HRP substrate, the fluorescence intensity was measured using a fluorescence microscope with a

2× objective lens. The linear actuation of the magnet took only about 7 min, but the total assay time, including the incubation of antigen-antibody, was about 40 min.

Results and discussion

Principles of MDS assay and fabrication of the Aβ assay chip

As mentioned above, many researchers have tried the sandwich assay using a single epitope or overlapping epitopes of anti-Aβ antibodies to detect the oligomeric form of Aβ for pre-clinical diagnosis of AD. Once the epitope binds to one of the antibodies, it is shielded. Consequently, monomeric Aβ having one epitope is not detectable because it cannot bind to both the capture antibody and the detection antibody simultaneously. The monomeric Aβ is washed out in the washing step process although it binds to detection antibody, or it does not generate a fluorescence signal when it binds to capture antibody since it cannot bind to the detection antibody. In contrast, oligomeric Aβ having more than two epitopes can bind to both capture antibody and detection antibody, and generate fluorescence signals on the beads (Figure 1a).

We developed a microfluidic platform to specifically detect oligomer Aβ based on magnetic beads, which follows the principle of MDS. MDS assay with magnetic beads can detect oligomer Aβ sensitively, and it simplifies the complicated ELISA process. To implement an MDS assay of Aβ in a microfluidic chip (Figure 2), antigens were incubated simultaneously with capture antibody-conjugated magnetic beads and HRP-conjugated detection antibody in the first chamber (i). After 30 min of incubation, the beads were collected and moved to the oil chamber (ii) by magnetic manipulation, followed by the washing step (iii). In the washing chamber, dispersed magnetic beads were rotated smoothly and soaked completely in the washing buffer. Then, the beads reached the read-out chamber (v) for reacting with the
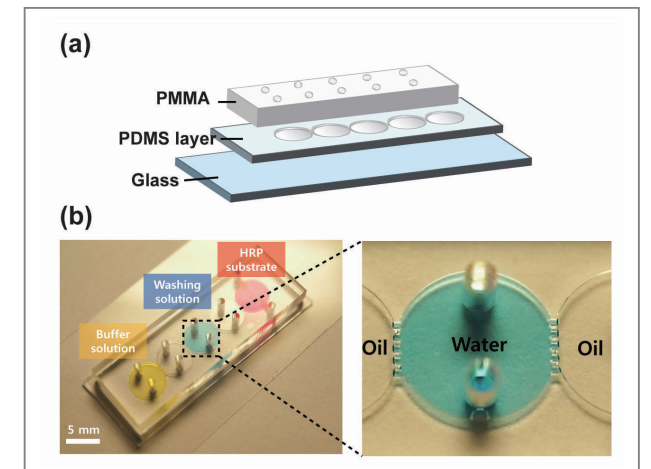

Figure 2. A microfluidic platform with micro-pillar structure for Aβ assay: (a) schematic drawings of a microfluidic device in exploded view; (b) photos of the assembled device (right) and top view of the device observed microscope (left); the scale bar is 5 mm. This chip measures 10 × 30 mm and consists of three layers, i.e., PMMA (top, 2-mm thickness), PDMS layer (600 μm), and cover glass (bottom). The PDMS layer contains five reaction chambers (5 mm in diameter) cast by Si master mold, and the top layer contains two holes for inlets. Each chamber contains liquids with typical volumes of 7 μl. Between the two chambers, four rectangular pillars (200 μm width, 200 μm length, and 300 μm height) were fabricated to serve as a robust interfacial barrier.
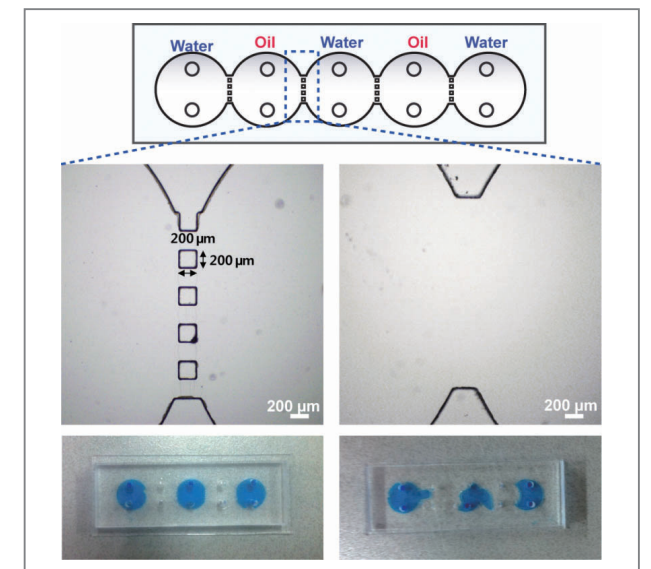

Figure 3. Influence of micro-pillars on the robust interfacial tension of two reagents: blue liquid indicates the water mixed with food dye, and the rest of the chambers contain mineral oil. The water-oil interfaces were maintained better in the presence of pillars as opposed to having no pillars. The pictures were taken immediately after filling the chambers with reagents.

HRP substrate and generated a fluorescence signal through enzymatic reaction. The interface between oil and water was maintained with the micro-pillars located at the border of two immiscible fluids (Figure 3) .

Detection of Aβ with MDS assay in the microfluidic chip

Quantitative assays of the serially-diluted OMSP solution and the OMSP-negative control were performed. The beads with capture-antibody mixed with OMSP and HRP-conjugated detection antibody were loaded in the first chamber and incubated for 30 min. After incubation, the magnetic beads were transported through the first oil chamber, followed by rotational washing. Then, the beads finally reached the read-out chamber. Consequently, oligomer Aβ and monomer Aβ competitively bound to the
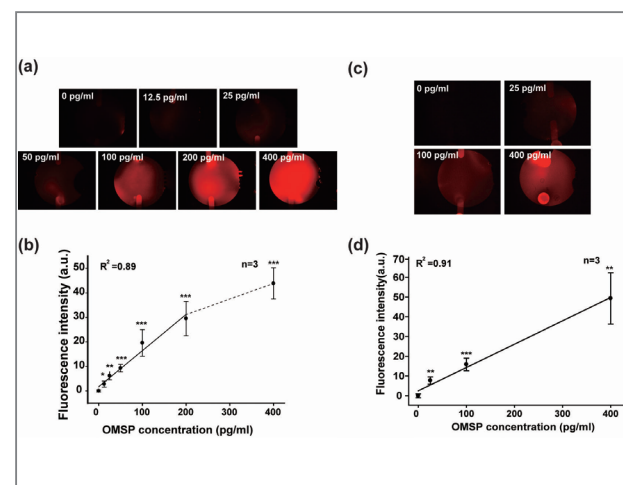

Figure 4. Quantification of oligomer Aβ in the reaction buffer (a, b) and in the human serum (c, d) using a magnetic bead-based microfluidic platform. The overall procedure was performed in the chip as depicted in Figure 1. A serial dilution of OMSP (12.5-400 pg/mL) in the reaction buffer was used. For the assay of Aβ in a human serum, a serial dilution of OMSP was spiked in a blood serum and diluted in the reaction buffer by 10% (v/v). Final concentration of OMSP in the reaction buffer was 25-400 pg/mL. (a, c) Typical fluorescence photographs of the read-out chambers for each sample and (b, d) the graph plotted from the fluorescence values. Each bar represents the average of three independent experiments. The error bars indicate the standard deviation. The detection was performed at 5 min after reaction with the HRP substrate. Statistical tests showed significant increases (∗ < 0.05, ∗∗< 0.01, and ∗∗∗< 0.001) in the signal for oligomer Aβ compared to the negative control.

antibody immobilized on the magnetic beads. The binding of oligomer Aβ increased in proportion to the amount of spiked Aβ (OMSP), resulting in increased fluorescence of the enzyme product (Figures 4a and 4b). In this case, the response was linear over the range of 12.5-200 pg/mL, and the limit of detection might be lower than the measurement limit since the level of the signal was significantly higher than that of the negative control. The limit of detection in detecting OMSP in a buffer solution was 10.7 pg/mL, calculated from a linear fitting model. However, RSD ranged from 7.2% to 21.7%, which are relatively high values because the reproducibility of the fluorescence signal between different sets was influenced by the time required for the overall assay and the variation in the amount of magnetic beads. An automatic system would be required to enhance the accuracy of the overall procedure.
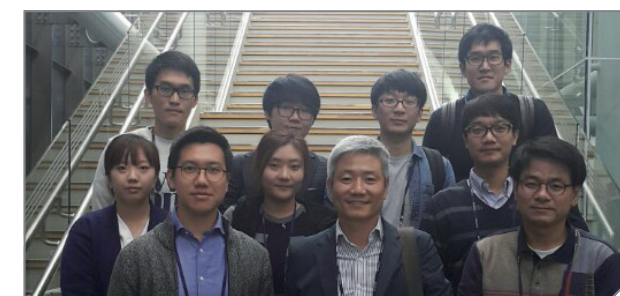
Conclusions

We developed a magnetic-bead-based Aβ assay platform using a microfluidic chip in which micron-sized pillars were fabricated to sustain the stability of the oil-water interface. The micro-features enhanced the stability of the interfacial tension of the two immiscible liquids at the boundaries of adjacent chambers of the microchip and enabled the magnetic beads to pass through stably without loss. It also increased the degrees of freedom in fluid handling and the capability to work with small sample volumes. Only 4 μg of magnetic beads were used in a chamber, consequently, a small amount of antibody was required for the AD diagnosis (10-30 ng of antibody per single assay). Also, the assay time was reduced significantly to 40 min, including incubation. However, a motorized automation system is required to minimize deviations while an external incubation step is better for batch diagnosis.

Note

This article and images are drawn from "Magnetic bead droplet immunoassay of oligomer amyloid β for the diagnosis of Alzheimer's disease using micro-pillars to enhance the stability of the oil–water interface" in *Biosensors and Bioelectronics*, Vol. 67, pg. 724.

References

[1] Ewers M, Sperling RA, Klunk WE, Weiner MW, Hampel H. *Trends Neurosci.* 2011; 34(8): 430-442.

[2] Seshadri S, Beiser A, Au R, Wolf PA, Evans DA, Wilson RS, Petersen RC, Knopman DS, Rocca WA, Kawas CH, Corrada MM, Plassman BL, Langa KM, Chui HC. *Alzheimers Dement.* 2011; 7(1): 35-52.

[3] Mapstone M, Cheema AK, Fiandaca MS, Zhong X, Mhyre TR, Macarthur LH, Hall WJ, Fisher SG, Peterson DR, Haley JM, Nazar MD, Rich SA, Berlau DJ, Peltz CB, Tan MT, Kawas CH, Federoff HJ. *Nat. Med.* 2014; 20(4): 415-418.

[4] Fukumoto H, Tokuda T, Kasai T, Ishigami N, Hidaka H, Kondo M, Allsop D, Nakagawa M. *FASEB J.* 2010; 24(8): 2716-2726.

[5] Hölttä M, Hansson O, Andreasson U, Hertze J, Minthon L, Nägga K, Andreasen N, Zetterberg H, Blennow K. *PLos One* 2013; 8(6): e66381.

[6] Santos AN, Ewers M, Minthon L, Simm A, Silber RE, Blennow K, Prvulovic D, Hansson O, Hampel H. *J. Alzheimers Dis.* 2012; 29(1): 171-176.

[7] Cleary JP, Walsh DM, Hofmeister JJ, Shankar GM, Kuskowski MA, Selkoe DJ, Ashe KH. *Nat. Neurosci.* 2005; 8(1): 79–84.

[8] Lacor PN, Buniel MC, Chang L, Fernandez SJ, Gong Y, Viola KL, Lambert MP, Velasco PT, Bigio EH, Finch CE, Krafft GA, Klein WL. *J. Neurosci.* 2004; 24(45): 10191–10200.

[9] Shankar GM, Bloodgood BL, Townsend M, Walsh DM, Selkoe DJ, Sabatini BL. *J. Neurosci.* 2007; 27(11): 2866-2875.

[10] Xia W, Yang T, Shankar G, Smith IM, Shen Y, Walsh DM, Selkoe DJ. *Arch. Neurol.* 2009; 66(2): 190-199.

[11] An SS, Lim KT, Oh HJ, Lee BS, Zukic E, Ju YR, Yokoyama T, Kim SY, Welker E. *Biochem. Biophys. Res. Commun.* 2010; 392(4): 505-509.

[12] Kang S, Lim K, Lee B, Kim GJ, Kang M, Jang M, Yang YS, Na HR, Youn YC, An S, Kim SY. *Alzheimer's & Dementia: The Journal of the Alzheimer's Association* 2010; 6 (4): e43.

[13] Herskovits AZ, Locascio JJ, Peskind ER, Li G, Hyman BT. *PLos One* 2013; 8(7): e67898.

[14] Herrmann M, Veres T, Tabrizian M. *Anal. Chem.* 2008; 80(13): 5160-5167.

[15] den Dulk RC, Schmidt KA, Sabatté G, Liébana S, Prins MW. *Lab Chip* 2013; 13(1): 106-118.

[16] Park H, Hwang MP, Lee KH. *Int. J. Nanomedcine* 2013; 8: 4543-4552.

[17] Zhang RQ, Liu SL, Zhao W, Zhang WP, Yu X, Li Y, Li AJ, Pang DW, Zhang ZL. *Anal. Chem.* 2013; 85(5): 2645-2651.

[18] He H, Yuan Y, Wang W, Chiou NR, Epstein AJ, Lee LJ. *Biomicrofluidics* 2009; 3(2): 22401.

[19] Lim CT, Zhang Y. *Biosens. Bioelecton.* 2007; 22 (7): 1197-1204.

[20] Rossier JS, Girault HH. *Lab Chip* 2001; 1(2): 153-157.

[21] Lehmann U, Vandevyver C, Parashar VK, Gijs MA. *Angew. Chem.* 2006; 45(19): 3062-3067.

[22] Ohashi T, Kuyama H, Hanafusa N, Togawa Y. *Biomed. Microdevice* 2007; 9(5): 695-702.

[23] Teste B, Malloggi F, Siaugue JM, Varenne A, Kanoufi F, Descroix S. *Lab Chip* 2011; 11 (24): 4207-4213.

[24] Adel Ahmed H, Azzazy HM. *Biosens, Bioelectron.* 2013; 49: 478-484.

[25] Long Z, Shetty AM, Solomon MJ, Larson RG. *Lab Chip* 2009; 9(11): 1567-1575.

[26] Shikida M, Takayanagi K, Inouchi K, Honda H, Sato K. *Sens. Actuators B Chem.* 2006; 113(1): 563-569.

Innovative Advances in the Development of Carbon-Based Composite Materials

Jaesang Yu
Carbon Convergence Material Research Center
jamesyu@kist.re.kr

Seung Min Kim
Carbon Convergence Material Research Center
seungmin.kim@kist.re.kr

Seong Yun Kim
Carbon Convergence Material Research Center
sykim82@kist.re.kr

Sungho Lee
Carbon Convergence Material Research Center
sunghol@kist.re.kr

Introduction

KIST Jeonbuk is taking a leadership role in the development of the composite materials industry as part of Korea's regional strategic industry growth initiatives. The institute researches and develops new source materials and trains professionals in the field of composite materials, a field deemed critical for 21st century industrial advancement. Composite materials are made by mixing two or more types of materials. By doing so, the advantages of each material can be combined to form a stronger structure with properties such as light weight, durability, extreme versatility, high strength and stiffness. KIST Jeonbuk is working intensively to develop innovative and dynamic composite materials, including carbon composites, and plans on becoming the R&D hub for advanced industries. The Carbon Convergence Materials Research Center (CCMRC) at KIST Jeonbuk is developing high-performance and high-value carbon-based composite materials by investigating carbon nanotube (CNT) fibers, carbon fibers (CFs), and carbon fiber reinforced plastics (CFRP) in hopes of improving the strength and stiffness of materials. This article presents an overview of these topics.

Synthesis of carbon nanotube fibers

CNT fiber is a macroscopic and continuous assembly of CNTs. Its continuous and macroscopic characteristics make it easy to handle compared to as-synthesized CNT powder, thus allowing it to be easily adapted into various applications. In addition, since CNT fiber is made up of multiple CNTs, it can take advantage of the excellent mechanical, electrical and thermal properties found in CNTs, even though the best performance of CNT fiber, to date, still falls short of its potential. However, several recent studies [1-5] have reported that CNT fiber can exhibit as high a mechanical strength as commercialized high performance fibers such as carbon fiber and Kevlar, with comparable electrical conductivities to conventional metals.

Three distinct methods have been developed for synthesizing CNT fibers. One route is to spin CNT fibers from CNT forests grown on planar substrate [6, 7]. This method is not scalable, but has been utilized extensively for model studies. The second method, known as direct spinning, draws CNT fibers directly from CNT aerogels synthesized in a chemical vapor deposition (CVD) reaction zone using a floating catalyst method [8]. The third method involves wet spinning, in which a CNT solution is injected through a spinneret and coagulated into CNT fibers [2, 9, 10]. This is the most widely used method for producing high performance fibers such as Kevlar and Twaron. The last two methods are easily scalable, but CNT fibers produced by these methods have quite different characteristics. A research group at KIST Jeonbuk has been focusing on the direct spinning method for developing high performance CNT fibers for the last two and a half years.

Figure 1 is a schematic showing the direct spinning process. In direct spinning, a precursor solution consisting of acetone as a carbon feedstock, ferrocene as a catalyst, and thiophene as a growth promoter is injected from the top of the reactor at a controlled feed rate. Then,
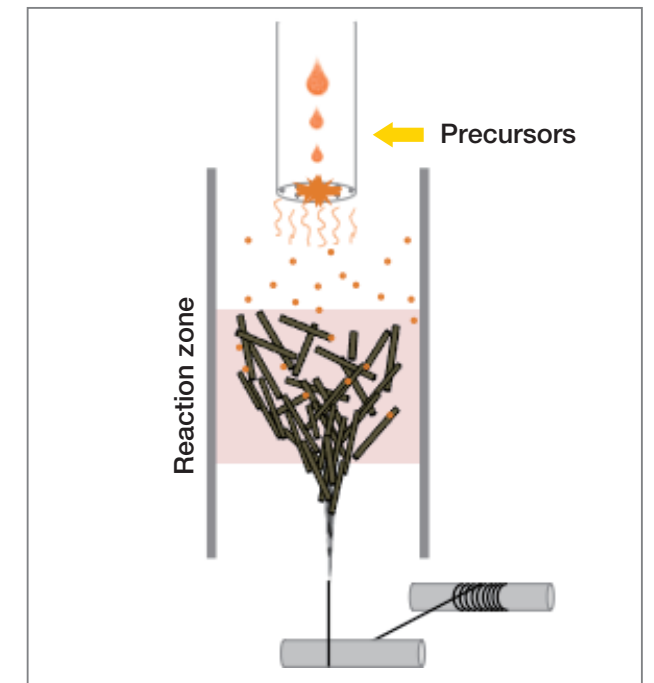
Figure 1. A schematic Schematic showing the direct spinning method.

the precursor solution is decomposed to produce CNT socks or aerogels in the reactor and the CNT socks are directly and continuously spun into the fibers. The biggest advantage of this method over other techniques is its rapid speed, since the growing of CNTs to spinning of CNT fibers entails only one process. One recent work [11] reported a spinning speed of 55 m/min at optimum conditions.

Figure 2 shows how a CNT sock or aerogel can be spun into two different forms. A CNT sock or aerogel is a hollow cylinder composed of a CNT network; therefore, if it is spun just below the reactor without any densification, it forms a CNT film or CNT paper. This is a simple route for producing CNT film without any solution processing. If there is a densification step using water or organic solvents before spinning, CNT fibers are produced. As-synthesized CNT fiber is held together primarily through van der Waals force between CNT bundles, so if chemical cross-linking through the covalent bonding is induced into as-synthesized CNT fibers, cross-linked CNT fibers

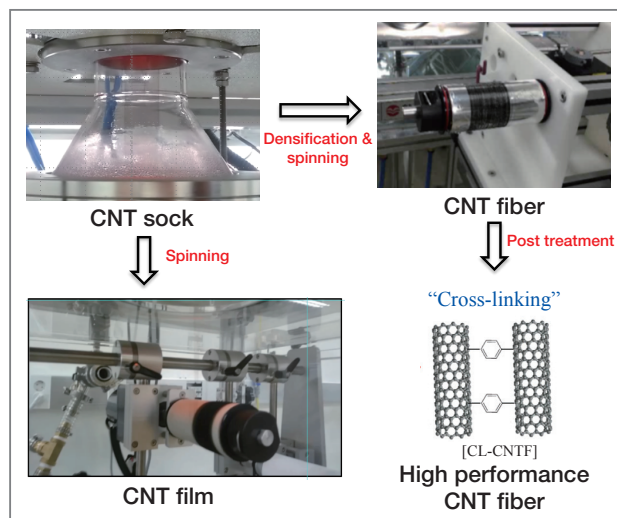**Figure 2.** Digital images of CNT socks, CNT fiber, and CNT film synthesized by the direct spinning method. The scheme of high performance CNT fiber produced by introduction of chemical cross-linking between CNT bundles.

Figure 3. (a) SEM image of CNT fiber and (b) TEM image of a double walled CNT composing CNT fiber. (c) Mechanical and (d) electrical properties of as-synthesized CNT fibers.

Figure 4. Structures of PAN and mesophase pitch base carbon fibers.

possess much higher mechanical properties. All these types of processing have been performed at KIST Jeonbuk.

Figure 3(a) is a SEM image of as-synthesized CNT fiber. This SEM image shows that CNT fiber consists of bundles of CNTs, which are roughly aligned along the direction of the CNT fiber. The TEM image in Figure 3(b) proves that CNT fiber indeed consists of double-walled (few-walled) CNTs. Types and diameters of CNTs can be roughly controlled by optimizing growth parameters such as growth temperature, composition of precursor solution, flow rate of carrier gas, etc. Figures 3(c) and 3(d) show the mechanical and electrical properties of as-synthesized CNT fibers. The average tensile strength is about 0.4 N/tex and the average electrical conductivity is 2.5×10^4 S/m. While these properties of raw CNT fibers are still inferior to the best properties of CNT fibers reported from the leading research groups [1-5], every effort is being made at KIST Jeonbuk to produce CNT fibers with much improved properties.

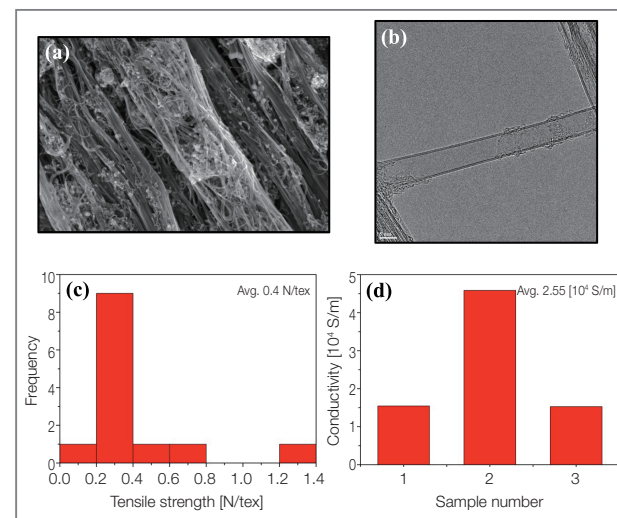CNT fiber is a very promising material that could possibly exhibit much better mechanical and physical properties than conventional engineering materials, with much lower density. Therefore, the successful development of CNT fiber technologies would open up a variety of new applications and vitalize the CNT industry.

Carbon fibers

CF is a carboneous material about 5–10 micrometres in diameter and composed of more than 90% carbon atoms. Historically, the first CFs from cellulose precursors were developed by Thomas Edison who used them as filaments in incandescent light bulbs. In 1941, DuPont produced polyacrylonitrile (PAN) spun fibers for textiles under the name of Orlon. The first industrial-scale structural CFs from the pyrolysis of rayon fiber were manufactured by Union Carbide in the late 1950s. In 1959, Akio Shindo began developing a process to utilize PAN fibers as precursors for CFs. This process improved the carbon yield about 50-60% compared to rayon-based CFs. Due to the low productivity of rayon-based CF, PAN and mesophase pitch have generally been preferred, but
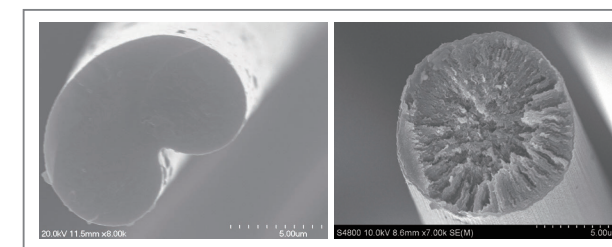
mesophase pitch-based CFs are inferior to PAN-based CF in terms of tensile strength, as shown in Figure 4. Furthermore, the difficulty of mesophase pitch synthesis represents another drawback due to its high average molecular weight with no or small side groups required for the melt spinning process. Consequently, PAN has been the most widely used material as a CF precursor over the last thirty years. Approximately 90% of CFs produced in the world are PAN-based CF.

PAN for CF precursors is a co-polymer containing acrylontrile (>90%) and various comonomers, e.g., methyl acrylate, methyl metharcylate, metharcrylic acid, vinylacetate, itaconic acid, and sodium methallyl sulphonate. The manufacturing process of PAN-based CFs involves three main steps: spinning, stabilization, and carbonization. The spinning of PAN solution or dope is a complicated process which involves rheological and diffusional phenomena. To form multiple PAN filaments, the dope is extruded through a spinnerrete with multiple small holes. The ability of the dope to successfully extrude is referred to as spinnability. The spinnability depends heavily on many rheological properties of the dope such as spinnerrete shape, diameter, capillary length and shear rate within the capillary. When the extruded dope containing 80-90% of solvent is exposed to a coagulation bath with a solvent/non-solvent mixture, the mass transfer of solvent/non-solvent concurrently occurs between the dope and coagulation bath. Consequently, the PAN solution is solidified and fibers are formed as the coagulation proceeds. It is important that the diffusion rate be controlled to obtain a fine round-shaped fiber

with uniform properties across its diameter. Technical parameters for the diffusion rate are the concentration gradients and temperature in both the coagulation bath and dope [12]. After coagulation, washing or extraction of solvent is performed via multiple baths, steaming, and winding. These requirements make wet spinning of PAN solution a complicated process.

In the stabilization process, the spun fibers undergo heat treatment at 200 to 300℃ in air, which leads to a thermally stable ladder structure through cyclization, dehydrogenation, and oxidation. This provides heat endurance at carbonization temperatures. It is known that nitrile groups in PAN are initiated thermally through a free radical mechanism, leading to a cyclized network of hexagonal carbon-nitrogen rings. Further, the nitrile groups in PAN with a large dipole moment provide high cohesive energy density and chain stiffness, which result in excellent tensile strength. Stabilization is one of the most important factors in determining the mechanical strength of PAN-based CFs. Fitzer et al. [13] reported the optimization of PAN fiber stabilization and effect of carbonization on resulting fibers as regards tensile strength. In conventional processes, stabilization takes place over many hours, which is an expensive and time-consuming process. Therefore, research has been aimed at achieving effective stabilization with less time/energy consumption in order to reduce the total cost of CF manufacturing which has been an obstacle for extensive applications in various industries.

Stabilized PAN fibers are heat treated up to 1500℃ under an inert gas atmosphere for carbonization with a yield of 50-60%. In commercial processes, carbonization consists of two steps: low temperature treatment (LTT) at 600-800℃ and high temperature treatment (HTT) at ~1500℃ for 5-10 min at each step. Evolution of gas species during carbonization needs to be considered for optimizing tensile strength because carbonization is a process to remove elements such as nitrogen, oxygen, and hydrogen in the form of volatile byproducts such as H_2O, HCN, and N_2; this results in CFs with a content of

at least 90 wt% carbon. Therefore, a number of steps and holding times for each step have been studied in the hopes of yielding high performance CFs.

These days, structural CF research conducted around the world generally falls into two categories: low-cost CFs and high performance CFs with high tensile strength modulus. For low-cost CF development, lignin precursors are studied as natural renewable sources which are much cheaper than using PAN or pitch precursors. Also, meltable PAN and new aromatic polymers have been synthesized to utilize melt spinning to reduce spinning cost. While these approaches are more cost-effective, more research is needed to increase the tensile properties of resulting CFs. Recently, novel methods of CF manufacture using plasma technology have been reported [14]. Using plasma discharge in the vicinity of the PAN fiber, air or a specific gas used for the process can be ionized or dissociated to make reactive oxidizing species such as atomic oxygen, reflected in Figure 5. Atomic oxygen, smaller than diatomic oxygen molecules, can diffuse inside the fiber more rapidly because of its smaller size and can shorten the total processing time needed for oxidation. In addition, the reactive oxidative species diffused into the fiber tow will stabilize the fibers more actively than diatomic oxygen since the dissociation energy of the diatomic oxygen can further be used to activate the reactions. Therefore, the use of plasma in CF manufacture is promising for cutting down the processing
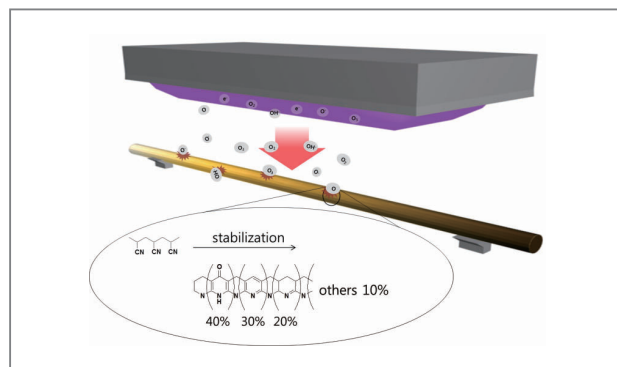

Figure 5. Scheme of plasma-assisted stabilization process [14].

time and price of CF when homogeneous process control can be utilized. Kumar et al. have developed CNT-incorporated CFs for high performance CFs [15]. These CFs provide high tensile strength as well as high tensile modulus up to 460 GPa due to the synergetic effect of CNT on crystalline structure development in CFs. Well aligned CNT in PAN fibers help to prevent thermal shrinkage of PAN molecules during stabilization and carbonization, and highly developed graphitic layers on CNT-induced graphitic structure in CFs from PAN fibers. However, dispersion of CNT in PAN solution and orientation control of CNT during spinning are key factors to maximize the reinforcing effect of CNTs.

During the last five years, the Carbon Composite Research Center at KIST Jeonbuk has worked extensively on solving both of the above mentioned issues with the support of KIST's institutional program and a government grant. Technology transfer has been successfully accomplished based on a facile methodology for preparing modified CNTs to enhance the degree of dispersion in PAN solution.

Carbon fiber reinforced plastic composites

All-composite vehicles, which emerged as a concept decades ago, have become a reality with the introduction by BMW of CFRP for all parts in i3 and i8 electric vehicles. Compared to metal, CFRP is lightweight and has outstanding mechanical properties. CFRP-based lightweight vehicles are expected to have improved fuel efficiency and lower CO_2 emissions. The development of all-composite cars was previously undermined by two problems: the high cost of carbon fiber and a slow CFRP manufacturing process. BMW resolved these issues by using high-pressure resin transfer molding (HP-RTM), a process that can be fully automated at high speed. By reducing the existing 10-minute resin transfer molding process to a 2-minute process, BMW opened up new

possibilities for CFRP to be used as a key material in vehicles.

Despite the successful implementation of all-composite vehicles based on HP-RTM, including a high pressure nozzle optimized for the mixing of epoxy resin and hardener, CFRP may take some time to be applied to mass-produced cars due to its limited repairability and recyclability. Repairability and recyclability are important requirements for vehicle parts, but the current technology for thermosetting epoxy resin is unsatisfactory in fulfilling such conditions. Key R&D trends for the future will include producing an epoxy resin with reduced cost and processing time, repair and recycling technology for thermosetting CFRP, and thermoplastic resin-based CFRP manufacturing technology that is superior to thermosetting resin in terms of manufacturing time, repairability and recyclability.

Korea's manufacturing technology for lightweight vehicle parts lags behind world-class standards. While German and Japanese car makers started developing all-composite vehicles at least ten years ago, Korea is still focused on technology for aluminum-based lightweight materials. Although the government launched an R&D project in 2011 for HP-RTM thermosetting CFRP manufacturing, Korea has lacked a full set of HP-RTM equipment, which is produced by the German firm Krauss Maffei (KM). It was only in 2015 that the government began supporting R&D into thermoplastic CFRP manufacturing.

The equipment deficit ended in September 2015 when KIST Jeonbuk installed HP-RTM equipment made

Figure 6. HP-RTM equipment at KIST Jeonbuk.

by KM (Figure 6), the same equipment used by BMW. Local companies used to spend millions of dollars and more than two weeks in HP-RTM process trials, but now the newly installed KIST equipment minimizes resource waste while improving R&D efficiency. Moreover, the equipment is expected to stimulate and facilitate research on the repairability and recyclability of thermosetting CFRP materials based on the HP-RTM process.

KIST Jeonbuk has studied high-speed manufacturing of thermoplastic CFRP for vehicles since 2012. Kim et al. [16-18] found that it is possible to produce vehicle parts from cyclic butylene, a low-viscosity thermoplastic oligomer resin. Since CBT resin is a ring-shaped oligomer ester comprised of 2-7 repeating units, ultra low viscosity of 0.02 Pa·s and outstanding filler impregnation are observed when oligomer resin first melts in the range of 130-150℃. The resin is polymerized at temperatures above 160℃ and exhibits physical properties similar to those of engineering plastic [19-24]. Significantly, polymerization is completed within two minutes at high temperatures above 250℃. These studies have served as the basis of a government R&D project, launched in 2015, on polymerizing monomers and oligomers to ultimately produce thermoplastic CFRP.

As shown in Figure 7, KIST Jeonbuk has also recently acquired a thermoforming injection molder (TIM) produced by KM. This TIM is capable of high-speed manufacturing of thermosetting CFRP. This involves IR heating of carbon fiber sheets followed by insertion of the sheets into metal molds and back injection of long carbon fiber composites, an LFT technology sought after by Germany's Audi in

Figure 7. TIM equipment at KIST Jeonbuk.

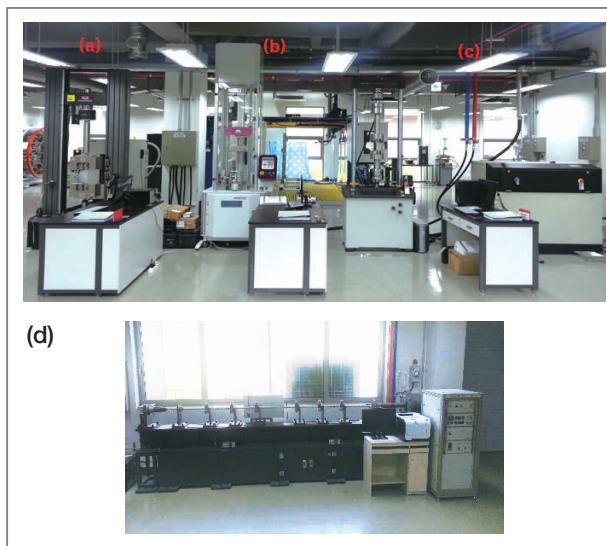**Figure 8.** (a) 3D C-Scan and (b) Micro CT equipment at KIST Jeonbuk.

Figure 9. Specialized equipments at KIST Jeonbuk. (a) High-load tensile tester. (b) Fatigue testing system. (c) High-performance shock tester. (d) Hopkinson bar tester.

mass production. Synergistic effects are expected with the novel technology in the high-speed manufacturing of thermoplastic CFRP vehicle parts, and the institute will continue to take the lead in related research in Korea.

KIST Jeonbuk has installed optimized equipment for the analysis of CFRP-based vehicle parts. As shown in Figure 8, 3D C-Scan and micro CT equipment are non-destructive CFRP analysis devices required for CFRP manufacturing. 3D C-Scan, usually used in the inspection of CFRP aircraft parts, is based on ultrasound and is capable of rapidly analyzing pores and other defects in CFRP. The micro CT equipment is a high-resolution non-destructive inspection device that enables high-precision observations of pores and carbon fiber orientation. Since CFRP will be applied to vehicle parts, KIST Jeonbuk has acquired high-performance equipment for the analysis of related mechanical properties, as shown in Figure 9. A high-load tensile tester, capable of evaluating the tensile, compressive, and flexural characteristics of CFRP, includes NADCAP (National Aerospace Defense Contractors Accreditation Program) alignment options to support the evaluation of aircraft parts. A fatigue testing system has been set up to enable precise evaluation of CFRP fatigue characteristics. To evaluate shock characteristics, a high-performance shock tester has been acquired. In addition, KIST Jeonbuk has become the nation's third institute to introduce a Hopkinson bar tester, which is necessary for destructive analysis of vehicle parts during accident testing.

Since 2012, KIST Jeonbuk has accumulated novel technology in the field of thermoplastic CFRP manufacturing while playing a leading role in related research. In addition to being the first institute in Korea to use HP-RTM and TIM equipment produced by Germany's KM, KIST has installed the best non-destructive analysis equipment and mechanical property analysis equipment to facilitate high-precision CFRP manufacturing. Through the continuous acquisition of novel technology and expansion of core processes, KIST seeks to be the world's best facility for the manufacturing of lightweight vehicle parts.

Conclusions

The CCMRC at KIST Jeonbuk is developing high-performance and high-value carbon-based composite materials primarily through the investigation of CNT fibers, CFs, and CFRP with high strength and stiffness. CCMRC has worked extensively to support the domestic carbon industry, which generates most of its income from these high performance composite materials. CCMRC will continue its research with the goal of developing source technology for high-value carbon composite materials.

References

[1]   Koziol K, Vilatela J, Moisala A, Motta M, Cunniff P, Sennett M, Windle AH. *Science* 2007; 318: 1892-1895.

[2]   Behabtu N, Young CC, Tsentalovich DE, Kleinerman O, Wang X, Ma AWK, Bengio EA, ter Waarbeek RF, de Jong JJ, Hoogerwerf RE, Fairchild SB, Ferguson JB, Maruyama B, Kono J, Talmon Y, Cohen Y, Otto MJ, Pasquali M. *Science* 2013; 339: 182-186.

[3]   Wang JN, Luo XG, Wu T, Chen Y. *Nat. Commun.* 2014; 5: 3848.

[4]   Gspann TS, Smail FR, Windle AH. *Faraday Discuss.* 2014; 173: 47-65.

[5]   Wu AS, Nie XN, Hudspeth MC, Chen WW, Chou T, Lashmore DS, Schauer MW, Tolle E, Rioux J. *Carbon* 2012; 50: 3876-3881.

[6]   Jiang K, Li Q, Fan S. *Nature* 2002; 419: 801.

[7]   Zhang M, Atkinson KR, Baughman RH. *Science* 2004; 306: 1358-1361.

[8]   Li Y, Kinloch IA, Windle AH. *Science* 2004; 304: 276-278.

[9]   Vigolo B, Penicaud A, Coulon C, Sauder C, Pailler R, Journet C, Bernier P, Poulin P. *Science* 2000; 290: 1331-1334.

[10] Ericson LM, Fan H, Peng H, Davis VA, Zhou W, Sulpizio J, Wang Y, Booker R, Vavro J, Guthy C, Parra-Vasquez ANG, Kim MJ, Ramesh S, Saini RK, Kittrell C, Lavin G, Schmidt H, Adams WW, Billups WE, Pasquali M, Hwang W, Hauge RH, Fischer JE, Smalley RE. *Science* 2004; 305: 1447-1450.

[11] Aleman B, Reguero V, Mas B, Vilatela JJ. *ACS Nano* 2015; 9: 7392-7398.

[12] Frank E, Steudle LM, Ingildeev D, Sporl JM, Buchmeiser MR. *Angew. Chem. Int. Ed.* 2014; 53: 5262.

[13] Fitzer E, Frohs W, Heine M. *Carbon* 1986; 24: 387.

[14] Lee SW, Lee HY, Jang SY, Jo SM, Lee HS, Choe WH, Lee S. *Carbon* 2013; 55: 361.

[15] Chae HG, Minus ML, Rasheed A, Kumar S. *Polymer* 2007; 48: 3781.

[16] Noh YJ, Lee SH, Kim SY, Youn JR. *Macromol. Res.* 2014; 22: 528-33.

[17] Kim SH, Noh YJ, Ko YW, Kim SY, Youn JR. *Polym. Eng. Sci.* 2014; 54: 2161-9.

[18] Lee HS, Kim SY, Noh YJ, Kim SY. *Compos. Pt. B-Eng.* 2014; 60: 621-6.

[19] Noh YJ, Joh HI, Yu JS, Hwang SH, Lee SH, Lee CH, Kim SY, Youn JR. *Sci. Rep.* 2015; 5: 9141.

[20] Noh YJ, Pak SY, Hwang SH, Hwang JY, Kim SY, Youn JR. *Compos. Sci. Technol.* 2013; 89: 29-37.

[21] Kim SY, Noh YJ, Yu JS. *Compos. Sci. Technol.* 2014; 101: 79-85.

[22] Kim SY, Noh YJ, Yu JS. *Compos. Sci. Technol.* 2015; 106: 156-62.

[23] Kim SY, Noh YJ, Yu JS. *Compos. Pt.. A-Appl Sci. Manuf.* 2015; 69: 219-25.

[24] Noh YJ, Kim SY. *Polym. Test.* 2015; 45: 132-8.

[**Feature Articles**]

Inverted Quantum Dot Light Emitting Diodes Using Polyethylenimine Ethoxylated Modified ZnO

Hong Hee Kim

Materials and Life Science Research Division
t12551@kist.re.kr

Won Kook Choi

Materials and Life Science Research Division
wkchoi@kist.re.kr

Do Kyung Hwang

Center of Opto-Electronic Materials and Devices
dkhwang@kist.re.kr

Introduction

In the past decade, colloidal quantum dots (QDs) have been a subject of active research due to their unique physical properties of size-dependent energy band gap, narrow spectral emission bandwidths, broad spectral photo response from ultraviolet to infrared, and compatibility with solution processes [1–6]. In particular, colloidal QD based light emitting diodes (QDLEDs) have attracted considerable attention as an emerging technology for next-generation displays and solid-state lighting [2, 3, 7–9]. Much effort has been devoted to enhance the luminous efficiency of QDLED, and as a result, its performance has been approaching that of organic light emitting diodes (OLEDs) [3, 7, 10–17]. While a number of approaches to improve the performance of the device have been proposed, the most practical proposal involves the optimization of charge transport and charge balance in the recombination region by carefully selecting the charge injection/transport layer and engineering interface between the QD emitter and transport layer [2, 3, 7, 15–17]. Using this approach, B. S. Mashford et al. recently reported on the state-of-the-art performance of a QDLED (maximum luminance over 50,000 Cd/m^2 and current efficiency over 10 Cd/A), comparable to that of phosphorescent OLEDs [7]. Polyethylenimine ethoxylated (PEIE) is a promising surface modifier to enhance electron injection into the QD emission layer and control the interfacial property for uniform film formation of the QD layer [18]. PEIE can be easily incorporated on top of metal, transparent conducting oxide, and conducting organic materials to modulate their electronic structures by lowering the work functions (WFs) [19]. In addition, a PEIE layer also induces uniform surface density of QDs by the coupling of aliphatic amine functional groups in PEIE with sulfur in CdSe-ZnS QD [18]. Therefore, in our previous study, we adopted PEIE as the electron injection layer material in an inverted structure QDLED [18]. The PEIE layer substantially reduced the WF of the ITO electrode while playing a significant role in the formation of a uniformly distributed CdSe–ZnS QDs monolayer. The resulting device exhibited a maximum luminance of 2900 cd/m^2 and luminance efficiency of 0.51 cd/A, but there was still room for further performance enhancement by optimizing charge balance in the QD emitter.

In this study, we incorporate the PEIE layer onto a colloidal ZnO nanoparticles (NPs) film as an electron injection/transport layer (EIL/ETL) on top of the ITO electrode. The ZnO NPs film has been widely used to improve electron injection and charge balance of QD emitters [7, 16, 17]. The PEIE surface modifier, incorporated on the top of the ZnO NPs film, facilitates the enhancement of both electron injection into the CdSe-ZnS QDs emissive layer by lowering the WF of ZnO from 3.58 eV to 2.87 eV and charge balance on the emission layer. As a result, red CdSe-ZnS QDLEDs with the ZnO NPs/PEIE layer exhibit a low turn-on voltage of 2–2.5 V, with a maximum luminance value of 8600 cd/m^2 and current efficiency of 1.53 cd/A, which is at least three times higher than the previous device with a PEIE single layer. Furthermore, the same scheme with the ZnO NPs/PEIE layer has been used to successfully fabricate green, blue, and white QDLEDs.

Results and discussion

Inverted red QDLED fabrication and material characterizations

A schematic cross-sectional view of an inverted red QDLED and corresponding cross-sectional high-resolution transmission electron microscopy (HRTEM) images are shown in Figure 1. The device consists of a patterned ITO (cathode), ZnO NPs/PEIE film as the EIL/ETL, CdSe-ZnSQDs as the emission layer (EML), the poly(N,N9-bis(4-butylphenyl)-N,N9-bis(phenyl)benzidine) (poly-TPD) and poly(N-vinylcarbazole) (PVK) blend layer as the hole transport layer (HTL), molybdenum trioxide (MoO$_3$) as the hole injection layer (HIL), and Ag (anode). ZnO NPs were synthesized per procedures in previously reported literature [17] and other materials were commercially available. PEIE, ZnO NPs, CdSe-ZnS QDs, and poly-TPD:PVK layers were prepared by spin coating. In the cross-sectional TEM image (left side of Figure 1b), the boundaries of the three layers of ZnO/PEIE/CdSe-ZnS QDs were difficult to distinguish, while those of the Ag, MoO$_3$, and poly-TPD:PVK layers were clear. In order to
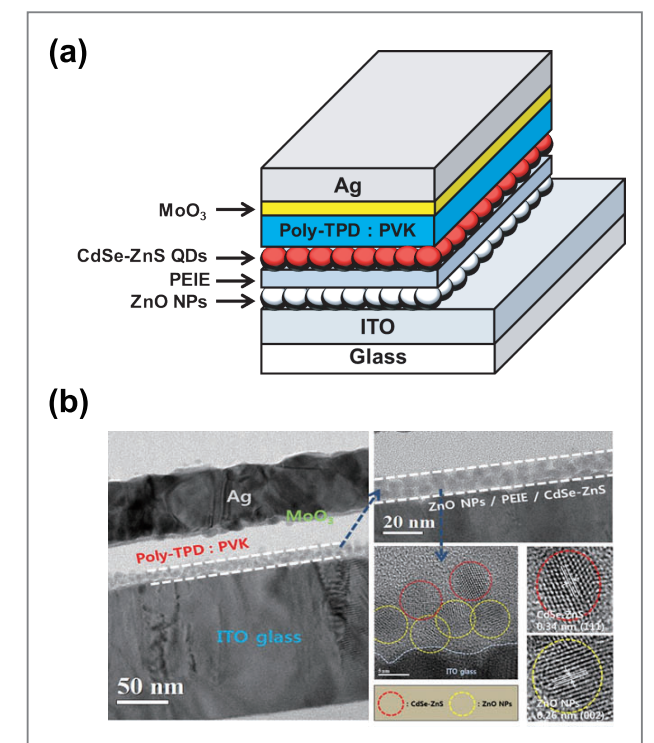

Figure 1. Device structure and TEM images. (a) A schematic cross-sectional view of an inverted red QDLED and (b) corresponding cross-sectional high-resolution transmission electron microscopy (HRTEM) images.
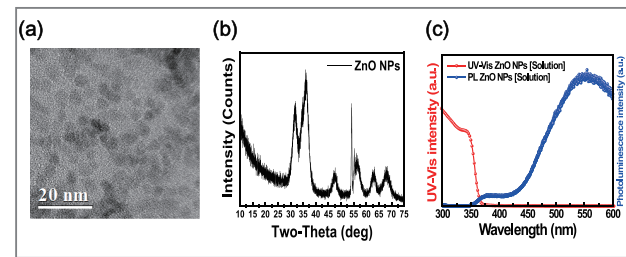
Figure 2. (a) XRD pattern from ZnO NPs film on Si substrate. (b) TEM image of ZnO NPs. (c) Absorption and photoluminescence spectra obtained from colloidal ZnO NPs solution dispersed in butanol. Excitation wavelength is 300 nm.

clarify boundaries, lattice fringes in magnified TEM images (right side) were carefully analyzed. ZnO NPs and CdSe-ZnS QDs have different crystal structures, resulting in clearly different lattice fringes as indicated by the red and yellow circles. CdSe-ZnS QDs have a zinc blend structure, and an interplanar distance of 0.34 nm corresponding to the (111) plane has been observed [20]. By contrast, our synthesized ZnO NPs have a wurtzite structure, which was confirmed by its X-ray diffraction (XRD) pattern, although the small particle size (average diameter of 4–5 nm) led to a significant broadening of the characteristic diffraction (see Figures 2a and 2b) [16]. The interplanar distance of 0.26 nm between lattice fringes corresponded to the (002) plane of ZnO [8]. It is interesting to note that the PEIE layer in-between ZnO NPs and CdSe-ZnS QDs is indistinguishable, which is attributed to infiltration by PEIE into ZnO NPs during the solution process. However, the significant change in ultraviolet photoemission spectroscopy (UPS) spectra of ZnO NPs and ZnO NPs/PEIE films shows that PEIE had covered the top surface of ZnO NPs, as reflected below.

Electronic energy level of ZnO NPs/PEIE

Figures 3a and 3b display the results of UPS spectra taken from ZnO NPs, PEIE, and ZnO NPs/PEIE spin coated on ITO and the corresponding energy level diagrams. The work functions could be calculated between the incident light energy (hn 5 21.22 eV) and the energy (E_{off}) of the secondary cutoff. In the case

of ZnO NPs film on top of ITO, the WF is estimated to be 3.58 eV, which is much lower than that of a normal ZnO film (more than 4.0 eV)21. Valence band maximum (VBM) is measured to be 7.49 eV. Considering the optical energy bandgap of 3.58 eV obtained from the absorption spectrum (see Figure 2c), the conduction band maximum (CBM) is calculated to be 3.91 eV, which is higher than the WF of 3.58 eV.

The origin of the lowered WF of ZnO NPs is still unclear, but could be correlated with the surface state of ZnO NPs. The photoluminescence (PL) spectrum shows a broad blue-green emission (see Figure 2c) that would be relevant to oxygen vacancies [7]. The synthesized 4–5 nm ZnO NPs have a very high surface area, indicating that many oxygen vacancies may exist in the surface. As a result, the oxygen-deficient surface of ZnO NPs leads to significantly lowered WF, which is consistent with a previously reported result from another study [7]. In the case of PEIE coated on ITO, the PEIE modifier substantially reduced the WF of ITO as low as 3.11 eV, consistent with our previously reported value [18]. PEIE also lowered energy levels of ZnO NPs, as shown by the measured values of WF at 2.87 eV, CBM at 2.91 eV, and VBM at 6.49 eV in the ZnO NPs/PEIE layer. Based on the above UPS results, the inverted QDLEDs adopting the ZnO NPs/PEIE layer would be most favorable for electron charge injection into the QD emission layer. The energy band diagram of the inverted QDLEDs consisting of ITO/ZnO NPs/PEIE/CdSe-ZnO QDs/poly- TPD:PVK/MoO₃/Ag is illustrated in Figure 3c (note: except for ZnO NPs/PEIE, other energy level values are taken from literature [22, 23]).

Red QDLED device performance.

Figure 4a shows the current density-voltage (J–V) characteristics of two inverted QDLED types, one adopting PEIE and another adopting ZnO NPs/PEIE layers. The QDLED with a ZnO NPs/PEIE layer has a lower turn-on voltage of 2.0–2.5 V and higher current density than the device with only a PEIE single layer (3.0–3.5 V), which is consistent with the UPS results. The
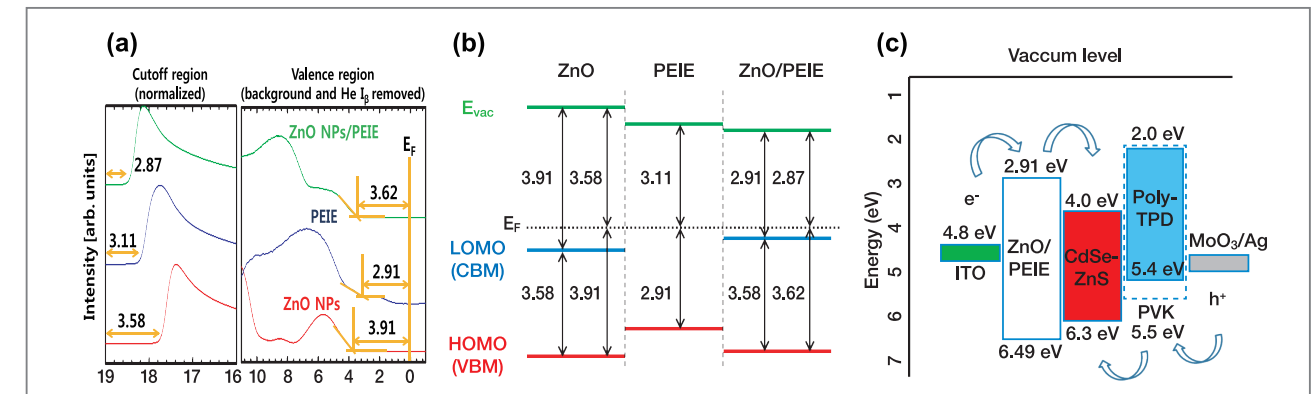

Figure 3. Electronic energy level. (a) Secondary cut-off region and valence (or HOMO) region after background removal obtained via UPS spectra of ZnO NPs, PEIE and ZnO/PEIE films deposited on ITO glass substrate, respectively, and (b) corresponding energy level diagrams. (c) Schematic illustration of energy band diagram of inverted QDLEDs consisting of ITO/ZnO NPs/PEIE/CdSe-ZnO QD/poly TPD:PVK/MoO3/Ag. The ZnO NPs/PEIE energy level was estimated from UPS and optical absorption measurement. Other energy level values are taken from literature. The pathways of the holes and electrons are indicated by the arrows.

ZnO NPs/PEIE layer also improved luminance and current efficiency characteristics. As shown in Figures 4b and 4c, the device with a ZnO NPs/PEIE layer displayed the maximum values of luminance of 8600 cd/m² at 7 V and current efficiency of 1.53 cd/A at 4.5 V, which are at least three times higher than those of the device with a PEIE single layer (2400 cd/m² at 7.5 V and 0.42 cd/A at 6 V). These enhancements in luminance and current efficiency properties could be correlated with the improvement of charge balance in the QD emission layer because the ZnO NPs functions not only as an electron transport layer but also as an efficient hole-blocking layer. PEIE as a surface modifier can modulate the WF of host material such as ITO or ZnO NPs to improve electron injection, but cannot play a role as a hole-blocking layer by itself. Therefore, the use of a ZnO NPs/PEIE layer facilitates

the enhancement of both electron injection into the QD emissive layer and charge balance on the QD emitter, resulting in improvement of device performance.

Full color QDLED demonstration

Figure 5a exhibits the PL spectrum of dilute red CdSe-ZnS QDs solution (dashed line) and electroluminescence (EL) of the device adopting the ZnO NPs/PEIE layer. The EL spectrum centered at 640 nm presents saturated emission from QD and is red-shifted by about 15 nm relative to the peak position of solution PL spectrum (625 nm).

The red shift is attributed to the enhanced interdot interactions arising from the reduced interdot distance in close-packed CdSe-ZnS film and/or to the electric-field-induced Stark effect [7]. The inset of Figure 5a is a photograph of the red light emission at 7 V with the Commission Internationale de l9Eclairage (CIE) color coordinate of (0.68, 0.31). The same scheme with the ZnO NPs/PEIE layer can be applied in fabrication of full-color inverted structure QDLEDs. We demonstrated green, blue and white inverted QDLEDs (note: for white color emission, red, green, and blue CdSe-ZnS QDs were mixed in a weight ratio of 1:3:10). The EL spectra and photographs of green, blue, and white QDLEDs
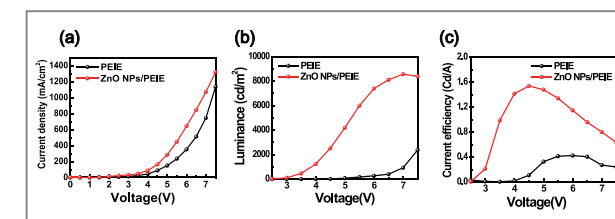

Figure 4. QDLED device characteristics. (a) Current density versus voltage, (b) luminance versus voltage, and (c) current efficiency versus voltage characteristics of QDLEDs with PEIE and ZnO NPs/PEIE layers.
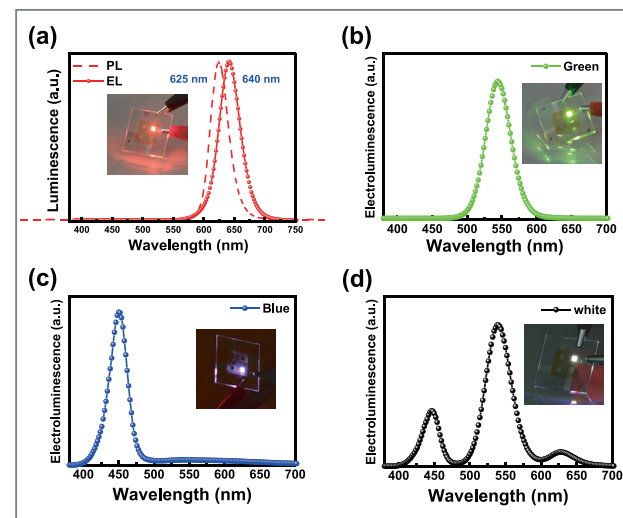
Figure 5. Red, green, blue, and white full color QDLED. (a) Photoluminescence spectrum of CdSe-ZnS QDs solution (dashed line) and electroluminescence spectra (solid line with circle symbol) of red QDLEDs adopting the ZnO NPs/PEIE layer. Electroluminescence spectra of (b) green, (c) blue, and (d) white QDLEDs with ZnO NPs/PEIE layers. Insets show photographs of red, green, blue, and white devices with a ZnO NPs/PEIE layer at applied voltages of 6.5–7.5 V.

Figure 6. Luminance versus voltage and current efficiency versus voltage characteristics of (a) green, (b) blue, and (c) white QDLEDs.

are shown in Figures 5b–5d. The devices reached the maximum values of luminance and current efficiency at 6.5–7.5 V: 18000 cd/m^2 and 1.26 cd/A with the CIE coordinate of (0.26, 0.70) for the green QDLED, 150 cd/m^2 and 0.006 cd/A with the CIE coordinate of (0.17, 0.6) for the blue QDLED, and 4500 cd/m^2 and 0.48 cd/A with the CIE coordinate of (0.25, 0.46) for the white QDLED. Details on luminance-voltage and current efficiency-voltage characteristics of green, blue and white CdSe-ZnS QDs are reported in Figure 6. As can be seen, the simple addition of a ZnO NPs layer to our PEIE-modified QDLED design has brought significant improvements to the device. However, the maximum device performance is yet to be realized as further optimization of the device design is still warranted.

Conclusion

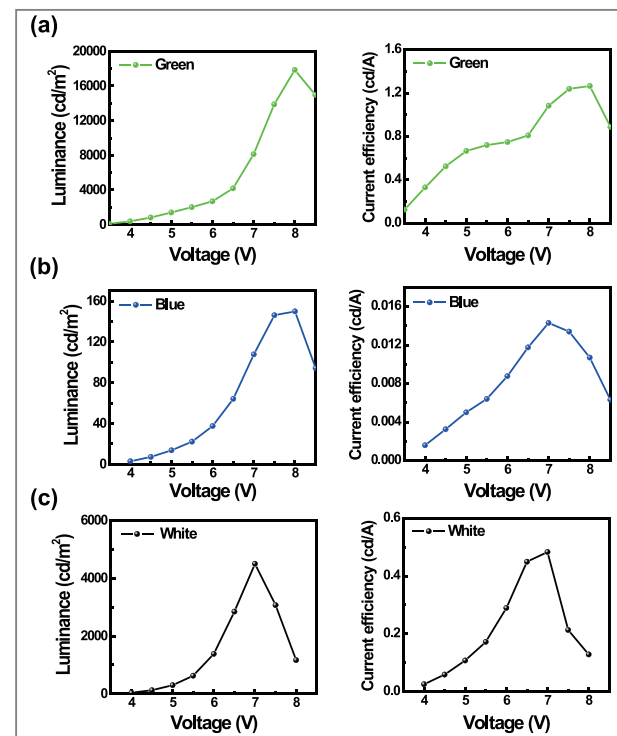In conclusion, we introduce a PEIE-modified ZnO NPs electron injection/transport layer for inverted red QDLEDs. The combination of PEIE and ZnO NPs facilitates the enhancement of both electron injection into the CdSe-ZnS QD emissive layer and charge balance on the emission layer. As a result, the device with the ZnO NPs/PEIE layer exhibits a low turn-on voltage of 2–2.5 V and maximum values of luminance of 8600 cd/m^2 at 7 V and current efficiency of 1.53 cd/A at 4.5 V, which are at least three times higher than those of a device with a PEIE single layer (2400 cd/m^2 at 7.5 V and 0.42 cd/A at 6 V). Furthermore, the same scheme with the ZnO NPs/PEIE layer was applied in the fabrication of full-color inverted structure QDLEDs, and we demonstrate green, blue and white inverted QDLEDs. We thus conclude that the use of ZnO NPs/PEIE is a promising and practical approach to realization of high performance, easy-to-fabricate, large-area inverted QDLEDs, paving the way for development of next-generation displays and solid-state lighting.

Note

References

[1] Coe S, Woo WK, Bawendi MG, Bulovic V. *Nature* 2002; 420: 800–803.

[2] Cho KS, Lee EK, Joo WJ, Jang EJ, Kim TH, Lee SJ, Kwon SJ, Han JY, Kim BK, Choi BL, Kim JM. *Nat. Photonics* 2009; 3: 341–345.

[3] Shirasaki Y, Supran GJ, Bawendi MG, Bulovic V. *Nat. Photonics* 2013; 7: 13–23.

[4] Jason PC, Gerasimos K, Keith WJ, Sjoerd H, Larissa L, Edward HS. *Nat. Nanotechnol.* 2009; 4: 40–44

[5] Jiang T, Kyle WK, Sjoerd H, Kwang SJ, Huan L, Larissa L, Melissa F, Xihua W, Ratan D, Dongkyu C, Kang WC, Armin F, Aram A, John BA, Edward HS. *Nat. Mater.* 2011; 10: 765–771.

[6] Semonin OE, Joseph ML, Sukgeun C, Hsiang YC, Jianbo G, Arthur JN, Matthew CB. *Science* 2011; 334: 1530–1533.

[7] Mashford BS, Stevenson M, Popovic Z, Hamilton C, Zhou Z, Breen C, Steckel J, Bulovic V, Bawendi MG, Sullivan SC, Kazlas PT. *Nat. Photonics* 2013; 7: 407–412.

[8] Son DI, Kwon BW, Park DH, Seo WS, Yi YJ, Angadi B, Lee CL, Choi WK. *Nat. Nanotechnol.* 2012; 7: 465–471.

[9] Kim TH, Cho KS, Lee EK, Lee SJ, Chae JS, Kim JW, Kim DH, Kwon JY, Amaratunga G, Lee SY, Choi BL, Kuk Y, Kim JM, Kim KN. *Nat. Photonics* 2011; 5: 176–182.

[10] Xie R, Kolb U, Li X, Basché T, Mews A. *J. Am. Chem. Soc.* 2005; 127: 7480–7488.

[11] Steckel JS, Snee P, Sullivan PC, Zimmer JP, Halpert JE, Anikeeva P, Kim LA, Bulovic V, Bawendi MG. *Angew. Chem. Int. Ed.* 2006; 45: 5796–5799.

[12] Anikeeva PO, Halpert JE, Bawendi MG, Bulovic V. *Nano Lett.* 2007; 7: 2196–2200.

[13] Sun, Q. et al. *Nat. Photonics* 2007; 1: 717–722.

[14] Bae WK, Char K, Hur H, Lee S. *Chem. Mater.* 2008; 20: 531–539.

[15] Caruge JM. et al. *Nat. Photonics* 2009; 2: 247–250.

[16] Qian L, Zheng Y, Xue JG, Holloway PH. *Nat. Photonics* 2011; 5: 543–548.

[17] Kwak JH, Bae WK, Lee DG, Park IS, Lim JH, Park MJ, Cho HD, Woo HJ, Yoon DY, Char KH, Lee SH, Lee CH. *Nano Lett.* 2012; 12: 2362–2366.

[18] Son DI, Kim HH, Hwang DK, Kwon SN, Choi WK. *J. Mater. Chem.* C 2014; 2: 510–514.

[19] Zhou Y, Hernandez CF, Shim JW, Meyer J, Giordano AJ, Li H, Winget P, Papadopoulos T, Cheun HS, Kim JB, Fenoll M, Dindar A, Haske W, Najafabadi E, Khan TM, Sojoudi H, Barlow S, Graham S, Brédas JL, Marder SR, Kahn A, Kippelen B. *Science* 2012; 336: 327–332.

[20] Sudhagar P, Pedro VG, Seró IM, Santiago FF, Bisquertb J, Kang YS. *J. Mater. Chem.* 2012; 22: 14228–14235.

[21] Mora-Sero I, Bertoluzzi L, Gonzalez-Pedro V, Gimenez S, Fabregat-Santiago F, Kemp KW, Sargent EH, Bisquert J. *Nat. Commun.* 2013; 4: 2272.

[22] Bae WK, Kwak JH, Lim JH, Lee DG, Nam MK, Char KH, Lee CH, Lee SH. *Nanotechnology* 2009; 20: 075202.

[23] Son DI, Park DH, Le SY, Choi WK, Choi JW, Li F, Kim TW. *Nanotechnology* 2008; 19: 395201.

[**Feature Articles**]

Structural and Optical Properties of Solid Solution II-VI Semiconductor Nanostructures
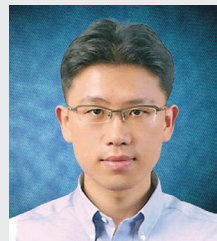
S. Joon Kwon

Nanophotonics Research Center
cheme@kist.re.kr

Introduction

There are various methods for fabricating semiconductor nanostructures with band gap (E_g) engineering to meet the requirements of applications in photonic devices. These methods include doping, quantum confinement effects, and alloying. In particular, alloying II-VI chemical compound single crystalline semiconductors with nano-scale structures provides facile ways of tuning optical and electronic transport properties and enhancing photo-converting properties with reliable engineered modulation of E_g over a broad range of the visible-IR spectrum. As we had reported in a former study on the structural and optical properties of binary alloy CdS_xSe_{1-x} nanowires (NWs), the geometrical confinement accompanied by formation of a thin and elongated single crystalline structure requires the alloy NWs to relax residual strain [1, 2]. This strain relaxation results in optical property anomalies, such as the disappearance of optical bowing. Being without optical bowing effects, the alloy NWs were found to be relevant for E_g modulation between 1.75 and 2.45 eV in a linear manner [1]. For quaternary alloy nanostructures composed of ZnS, ZnSe, CdS, and CdSe, it is expected that the facile E_g modulation and wide coverage is more promising than with simple binary alloy nanostructures. However, there are several factors which could work together in limiting design of the arbitrary composition for the stable form of quaternary alloys. These factors also affect the morphological evolution of the alloy nanostructures, not only the NWs, but other forms as well,

such as nanosheets (NSs) and nanobelts (NBs). Thus, it is important to understand the correlations among the composition, structural stability, morphology, crystallinity, and optical properties of the quaternary alloy nanostructures prior to designing an E_g modulation strategy.

In this article, we report summarized findings on a structure-related optical anomaly in the quaternary alloy $Cd_xZn_{1-x}S_ySe_{1-y}$ nanostructures that involve NWs, NBs, and NSs in the nearly full visible spectrum [3]. Given different compositions (x and y), we observed three different morphologies including NWs, NBs, and NSs, which covered a broad range of E_g of 1.96-2.88 eV. These different nanostructures showed different optical properties, such as the disappearance of optical bowing for NWs [1], maximum optical bowing for NBs and slightly smaller bowing for NSs. We used a computational method to determine the structural origin underlying the observed structure-dependent E_g anomaly. We found that the intrinsic atomic disorder decreased as the morphology of the nanostructures evolved from NWs via NBs to NSs. A semi-empirical equation determining the structure-E_g anomaly correlation as a function of morphological parameter was found to agree with the experimental observation.

Results and Discussion

Shown in Figure 1(a) are SEM images of alloy $Cd_xZn_{1-x}S_ySe_{1-y}$ nanostructures with different compositions. The different growth temperatures give rise to different geometries from NWs at higher growth temperatures intervened by NBs in an intermediate temperature range to NSs at lower temperatures. The NWs have diameters ranging from 85 to 105 nm and lengths attaining 25-40 μm, while the width of the NBs was up to 0.85-1.45 μm and thickness and length attaining 95-110 nm and ~12 μm, respectively. For the NSs, thickness ranged from 90-110 nm and the area of the sheets
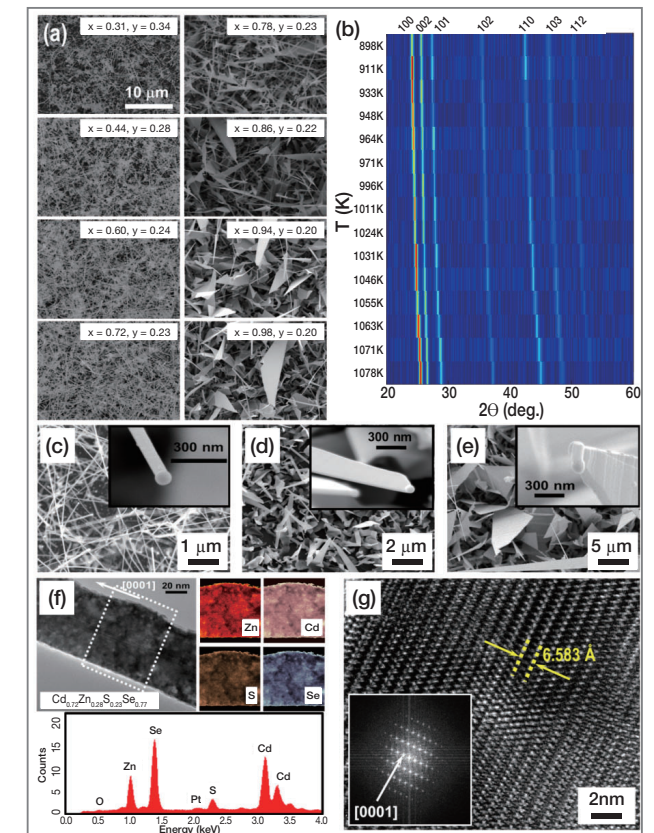
Figure 1. (a) SEM images of quaternary alloy nanostructures grown at different temperatures (T). (b) Color-mapped XRD data. (c)-(e) Representative SEM images with insets showing magnified SEM images of the edges of structures that are attached to Au alloy tips. (f) A bright field TEM image. (g) HR-TEM image for the alloy NWs with an inset of the SAED pattern showing the crystallinity identified as HWZ.

was up to 480-930 μm². The XRD data presented in Figure 1(c) for the alloy nanostructures indicate that the nanostructures form solid solution phases. To check the growth mechanism of the alloy nanostructures, we further explored the morphological evolution as shown in SEM images in Figures 1(c)-1(e). We can observe a clear interface between a small Au alloy tip and the end or the edge of the nanostructures. One of the representative analysis results is given in Figure 1(f) from which we can confirm that there is no spatial or elemental correlation in the elemental distribution data obtained from EDS mapping. Finally, we used HR-TEM to observe the single crystallinity and measure lattice parameters of the alloy

nanostructures directly. As shown in the HR-TEM image with SAED pattern in Figure 1(g), we can confirm that the alloy nanostructures have single crystallinity. To calculate the composition of the alloy nanostructure, we employed a linear approximation. x decreases and y increases with increases in growth temperature. Combining the composition and the component fraction analysis with XRD and HR-TEM analysis, we analyzed the dependence of the hexagonal Wurtzite (HWZ) lattice parameters as a function of the growth temperature. The calculated lattice parameters indicate that the solid solution alloy nanostructures satisfy the virtual crystal approximation (VCA) model [4].

We further explored optical properties of the alloy nanostructures by using photoluminescence (PL) and UV-visible absorbance (Abs) spectra. As shown in Figure 2(a), a clear red shift in PL can be observed when the fractions of the CdS and CdSe are relatively abundant
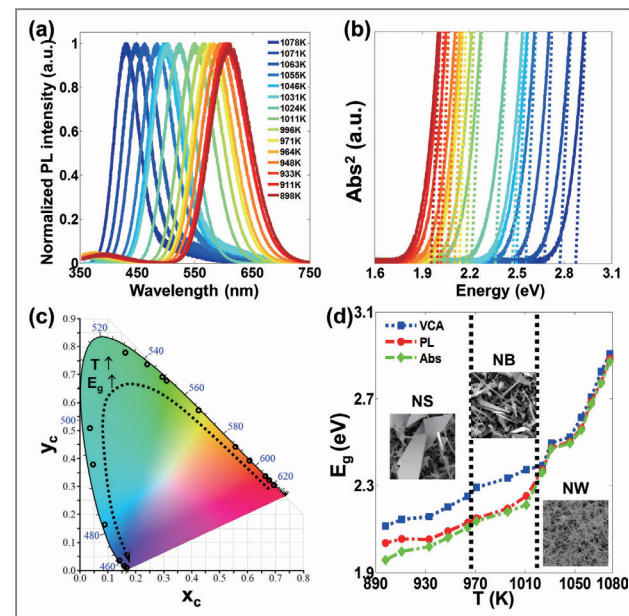
with decreasing growth temperature. From the PL analysis, the capability of E_g modulation was observed to cover nearly the full range of the visible spectrum. The observed values of E_g obtained from the Abs (Figure 2(b)) are slightly smaller than those from the PL spectra. We matched the observed PL spectra with the visible color obtained from the CIE-1931 color map (Figure 2(c)). As pinned in the map, continuously varying color coordinates of the alloy nanostructures clearly indicate that the alloy nanostructures can cover nearly the full visible spectrum. Finally, we tried to compare the expected value of E_g from the VCA model with the experimentally measured values. As is apparent from Figure 2(d), $E_{g,VCA}$ is larger than the experimentally observed values. This difference in E_g is the optical bowing in the alloy semiconductor. For alloy semiconductors, the bowing effect is ascribed to intrinsic bowing due to disorder. The bond-length disorder confined in the unit cell can result in the notable bowing. From the perspective of a simple VCA model, the disappearance of E_g bowing for the alloy NWs indicates that the residual strain would be negligible. In contrast, the bowing in the alloy NBs and NSs indicates that there is residual strain. From these observations, we can suggest that the optical bowing effect due to residual strain depends on the morphology and intrinsic atomic disorder.

To examine how the different morphologies and atomic disorders would affect the residual strain and the optical bowing effect in the alloy nanostructures, we tried to find a correlation between the optical bowing factor and the structural properties of the alloy nanostructures. For the quantitative analysis, we used a simple computational method based on the empirical pseudopotential method (EPM) to calculate electronic band structure with different compositions. Shown in Figures 3(a) and 3(b) are the calculated electronic band structures of the single HWZ crystalline alloy NBs with different residual strains. In Figure 3(c), the calculation result is summarized as a function of the growth temperature. As is apparent from the figure, there is a continuous but abrupt change in the residual strain in the alloy nanostructures at a certain growth
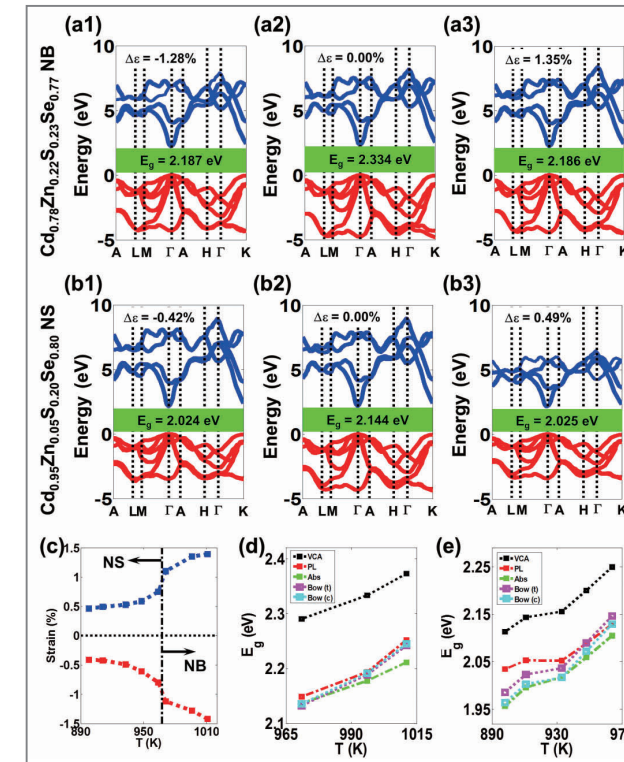

Figure 2. (a) Normalized photoluminescence (PL) and (b) squared UV-Vis absorbance (Abs) spectra of the alloy nanostructures grown at different T. (c) Visible colors from the PL spectra fixed on the CIE-1931 color map. (d) Dependence of E_g as a function of T: expected values from the VCA model (blue marks and dotted line) and experimentally measured values obtained from the PL (red marks and dash-dot lines) and Abs (green marks and dash-dot lines) spectra.

Figure 3. Calculated electronic band structures of the quaternary alloy NBs with different residual strains ($\Delta\varepsilon$) and NSs with different residual strains. (c) Dependence of $\Delta\varepsilon$ at different T. (d) Dependence of E_g with increasing T. Calculated values of E_g (black dotted lines) are compared with the experimentally observed values (PL (red) and Abs (green) dash-dot lines) and calculated values obtained by the bowing equations with different parameter sets for the alloy NBs with tensile (t, maroon lines) and compressive (c, cyan lines) residual strains, respectively. (e) As (d), but for the alloy NSs.

Figure 4. (a) 2D map for the variations of the volumetric ratio between the concentration-weighted summation of unit cell volumes of HWZ CdS, CdSe, ZnS, and ZnSe and the unit cell volume of HWZ alloy $Cd_xZn_{1-x}S_ySe_{1-y}$ $(1 + \Delta\varepsilon_v)$ as a function of x and y. In the map, black circles are the composition data extracted from the observed alloy nanostructures. (b) Dependence of $1 + \Delta\varepsilon_v$ as a function of T. (c) As (a), but for the biaxial strain factor $\Delta\varepsilon_{bi}$. (d) Dependence of $\Delta\varepsilon_{bi}$ as a function of T. (e) As (a), but for the bond length mismatch parameter $(\Delta b^2/c^2)$. (f) Dependence of $\Delta b^2/c^2$ as a function of T. (g) Ratio between the width and thickness of the nano-plate shaped alloy nanostructures (L/D) as a function of T. (h) Dependence of $(\Delta b^2/c^2)$ as a function of L/D. The data is fitted with a power-law function such that $\Delta b^2/c^2 \sim (L/D)^\alpha$.

temperature between 964K and 971K. This point implies the existence of a transition point between the NBs and NSs. The bowing parameters are mainly determined by intrinsic structural properties such as atomic disorder and residual strain. The optical bowing relationship agrees with the experimental observations for both alloy NBs and NSs (Figures 3(d) and 3(e)).

Next, we investigated the structural origin that governs the observed anomaly of the optical properties of the alloy nanostructures. In Figures 4(a) and 4(c), we provide 2D maps for the distribution of strain change as a function of the composition. From the maps, it can be seen that the strain factors decrease with decreasing compositional
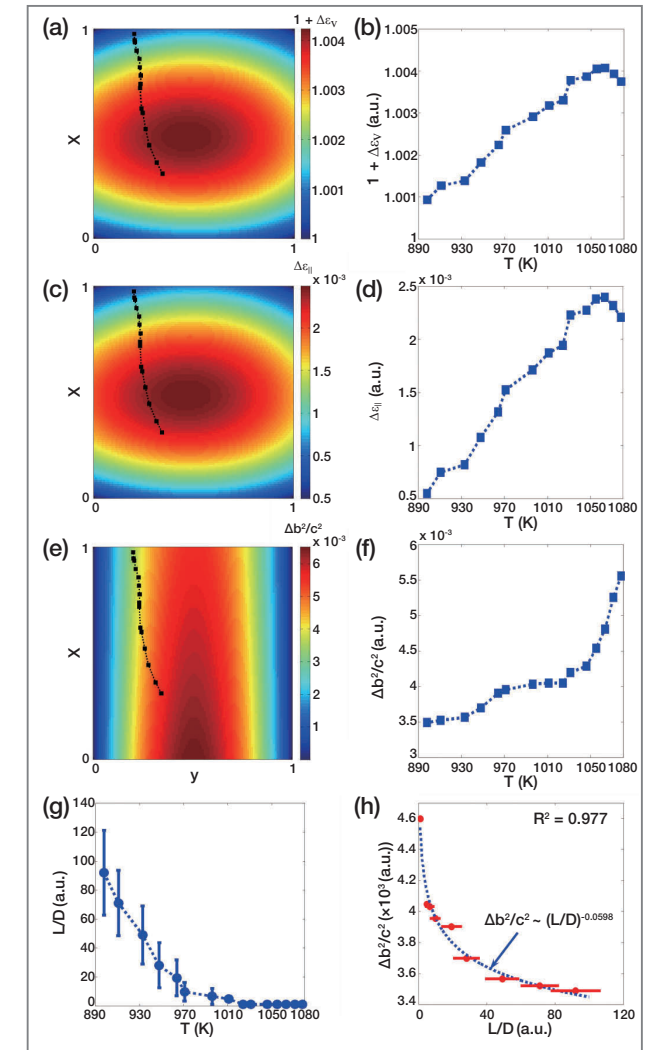
entropy. Given the observed composition at different growth temperatures, we can analyze the strain changes as shown in Figures 4(b) and 4(d). It is evident from these figures that the strain factors decrease from the alloy NWs

via NBs to NSs. It should be noted that the decreasing behaviors of the strain factors from the NWs to NBs are contrary to the observations of optical bowing.

In addition, we can analyze atomic disorder by calculating bond-length mismatch, which originates from the atomic displacement of the anions from the designated center coordinates of the HWZ unit cell. We constructed a 2D map (Figure 4(e)) for the distribution of bond length mismatch and analyzed its variations at different growth temperatures (Figure 4(f)). As shown in Figure 4(f), it is evident that the atomic disorder generated by the bond-length mismatch decreases with decreasing growth temperature, as in the context of the strain factors. Thus, it is contrary to the experimental observations of no optical bowing for the alloy NWs and high bowing for the alloy NBs. This implicates the existence of a counterpart that describes the increasing behavior of the degree of bowing reduction from NSs to NWs.

We translated the behavior between the bond length mismatch and the growth temperature into a relationship between shape and bond length mismatch (Figures 4(h) and 4(g)). In Figure 4(h), we found a simple scaling law for this relationship. As a semi-empirical method, we propose the strain and atomic disorder relaxation factor. In the case of single crystalline and structurally stable NBs or NSs, in contrast to NWs, it is not required for the alloy nanostructure to relax the biaxial strain over the plane direction. Thus, it is expected that the strain relaxation factor increases for NSs, and saturates for the alloy NSs of sufficiently wide sheets. By combining the strain relaxation factor and the scaling behavior of the bond-length mismatch, it is possible to construct a semi-empirical structural disorder-bowing factor correlation, which predicts no bowing for NWs, but increasing bowing for NBs and NSs. As shown in Figure 5, we can find that the semi-empirical correlation describes the observed behaviors of the structure-dependent E_g anomaly such as the disappearance of the bowing for NWs, maximum bowing for NBs, and smaller yet notable bowing for NSs with a good statistical fitting coefficient. It is also notable
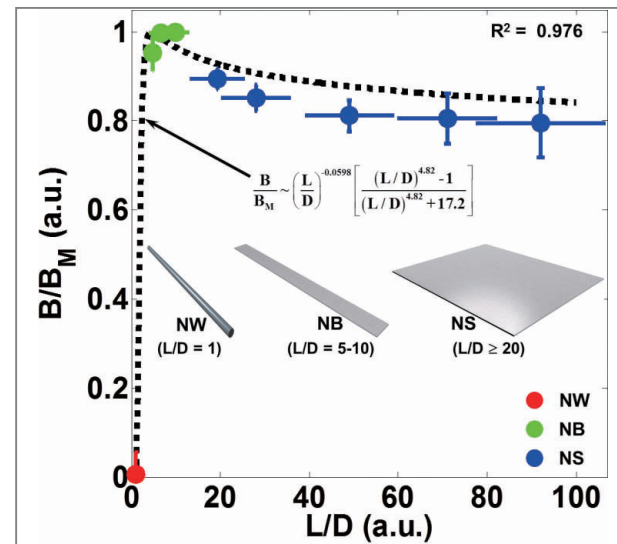
Figure 5. Dependence of the experimentally observed normalized bowing factor (B/B_M) as a function of L/D.

that the difference between the NBs and NSs are clearly observable: maximum and nearly constant values for the NBs, smaller and nearly constant values of the NSs.

Conclusion

As shown above, it is evident that there is a structure-dependent optical anomaly, represented by the peculiar optical bowing behaviors of the NWs, NBs, and NSs. It is also possible to distinguish NBs from NSs by examining their structural and optical properties. In terms of E_g modulation engineering, it is highly desirable to find a semi-empirical yet quantitative correlation on the structure-bowing relationship. Thus, the present experimental study, supported by computational studies with a mathematical model, is beneficial to accurately modulate E_g of II-VI alloy nanostructures to cover the full visible spectrum.

Note

This article and images are drawn from "Structural

Origin of the Band Gap Anomaly of Quaternary Alloy $Cd_xZn_{1-x}S_ySe_{1-y}$ Nanowires, Nanobelts, and Nanosheets in the Visible Spectrum" in *ACS Nano* (2015) Vol. 9(5), pp.5486~5499.

References

[1]   Kwon SJ, Choi YJ, Park JH, Hwang IS, Park JG. *Phys. Rev. B.* 2005; 72: 205312/1-205312/7.

[2]   Zunger A, Jaffe JE. *Phys. Rev. Lett.* 1983; 51: 662-665.

[3]   Kwon SJ, Jeong HM, Jung K, Ko DH, Ko H, Han IK, Kim GT, Park JG. *ACS Nano.* 2015; 9: 5486-5499.

[4]   Vegard L. *Z. Phys.* 1921; 5: 17-26.
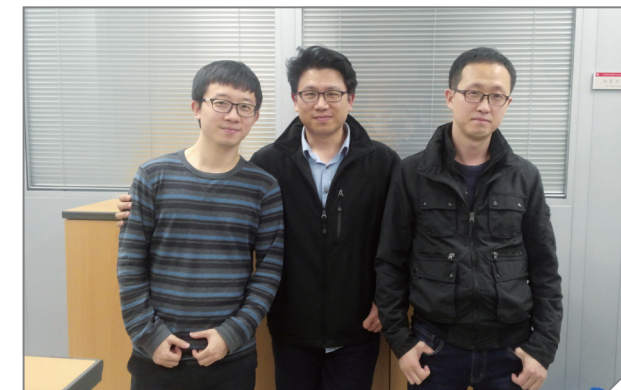
Using Indoor Farming Systems to Increase Food Production in Response to Global Environmental Changes

Chu Won Nho
Natural Products
Research Center
cwnho@kist.re.kr

Jai-Eok Park
Natural Products
Research Center
j-park@kist.re.kr

Sung-Yul Chang
Natural Products
Research Center
schang8@kist.re.kr

Introduction

The production of food crops throughout the world has become more challenging due to the shrinking of arable areas resulting from urban expansion, increasing desertification, and water shortages. To make matters worse, projected climate changes and the rapid growth of world population will put an additional burden on future food production. Indoor farming offers some hope for alleviating the strains imposed by environmental changes and population pressure.

Most crops are produced outside, so unfavorable weather conditions can significantly reduce crop yields. Therefore, to minimize unfavorable weather effects, indoor farming has long been practiced for agricultural production. However, even when using an indoor farming system, growers need lots of environmental data to produce quality food. Essentially, different approaches should be applied to each crop in order to optimize production in terms of quality and quantity. Two types of technology are required to produce the best possible vegetable crops in closed environments. First, a sensing device is needed to diagnosis and gather plant information. This device acts as an environmental sensor to assess surrounding conditions and control the physiologic status of plants through adjustments to the indoor environment. Second, it is necessary to analyze data in great detail to understand the interaction between the genetic composition of a plant and different environments.

Indoor farming is not a new concept, but the development of new convergence technologies has the potential to significantly improve agricultural production systems. The following review focuses on these emerging technologies and how they may enable more stable and customizable food production for a rapidly expanding population.

Indoor farming system overview

A closed environment plant production system is referred to as an "indoor farming system." It is a fully controlled plant production system using artificial light, air conditioning, carbon dioxide, a water supply and cultivation solutions. These systems consume less water, fertilizer and labor than in outdoor fields and produce more crop per area. They also generate a more stable annual output free of typical exterior influences, such as plant disease, insect damage, seasonal changes, light limitations and natural disasters because the systems can control airborne factors (temperature, relative humidity, air flow, carbon dioxide and light quality) and root influences (temperature and nutrients) in the environment which surrounds the plants (Figure 1). An indoor farming system can be run systematically, with planned production almost as standardized as a manufacturing system. Moreover, plants produced from these systems are more

Figure 1. Automated indoor farming system (Osaka Prefecture University, 2012)

environmentally friendly because they are pesticide-free. According to the theory of Kozai, a closed plant production system is less of an environmental burden than other plant production systems, such as open and semi-closed systems, because the production system transforms all of the input material resources into the output (crop) and additional products without using or emitting environmental pollutants. Moreover, 90% of the evapotranspirated water from plants is recovered through the air conditioning system [1]. The photosynthesis function is a complex one determined by many factors. Therefore, integrated environmental controls for the maximization of photosynthesis is the first priority in establishing a successful indoor farming system.

Table 1. Image-sensing techniques for obtaining phytobiological information on plants and soils [6].

Image-sensing techniques	Phytobiological information
• Multi- or hyperspectral image sensing (near UV to near-0 infrared, including color)	• Color, shape, and growth of individual plants and parts, plant pigments, water status, soil properties
• Thermal image sensing	• Temperature, evapotranspiration, stomatal response
• Fluorescence image sensing (laser-induced fluorescence, chlorophyll fluorescence, etc.)	• Bleaching of plant pigments, movement of fluorophores in mesophylls, photosynthetic system
• 3-D surface image sensing(stereo, shape-form-x, laser scanner)	• 3-D surface structure and biomass of plants and canopy
• 3-D light microscopic imaging	• 3-D structure and functions of cells and tissues
• CT (X-ray CT, MRI, optical CT, etc.)	• 3-D structure and content, transfer and metabolism of biochemical components of/in tissues and plants

Indoor farming systems are an area of active research and commercialization opportunities in Asia, especially in Korea, China, Taiwan and Japan. In addition, studies related to plant functionality through control of the growing environment in closed plant production systems are increasing with a greater understanding of the potential benefits of secondary metabolites generated from plants.

In Japan, indoor farming systems have been actively studied with more than 150 commercial systems up and running in 2011 [2]. Another form of indoor farming, space farming, has been investigated for many years by NASA in the United States [3]. However, these kinds of studies are focused on environmental control based on ambient environmental information. Recently, other approaches to environmental control engineering have been attracting a lot of attention in plant production systems [4, 5]. For example, phytobiological information can be gathered through image sensing which can measure wider areas at a time, and mathematical modeling can be used for engineered metabolic control. Table 1 details the image sensing techniques available to obtain phytobiological information depending on the desired information.

Chlorophyll fluorescence sensing is an active sensing technique for obtaining phytobiological information by measuring the fluorescence emitted from living plants [6]. Plants dissipate residual light energy, which is not used for photosynthesis, as heat or re-emitted as red light. So, the accurate measurement of chlorophyll fluorescence emission can evaluate photosynthetic function [7]. With this technique, Takayama and Nishina developed a chlorophyll fluorescence imaging robot to monitor the health of tomato crops in a large scale greenhouse [8]. Fukuda et al. developed a technique for the early assessment of productivity using clock gene promoter activity, which demonstrated a higher correlation to productivity based on biomass and LUC protein than leaf area under various growth conditions [9].

Applying plant phenotyping to indoor farming systems

The term "phenotype" was originally defined as the observable traits arising from the genetic composition of an organism. In the simplest terms, the genetic composition of a plant was the key factor in determining the final phenotype of a plant. However, phenotype can be influenced not only by genetic variation but also by interaction with environmental factors. For example, levels of anthocyanin, a health-promoting compound produced by various plant species [10], can be influenced by environmental factors such as temperature and lighting conditions [11].

Plant growth data is important for producing the highest quality fruits and vegetables in an indoor farming system. The data is inherently complex because each plant has a very unique genetic composition which is constantly influenced by environmental factors. Traditionally, the collection of data was highly labor intensive, involving the linking of individual gene functions
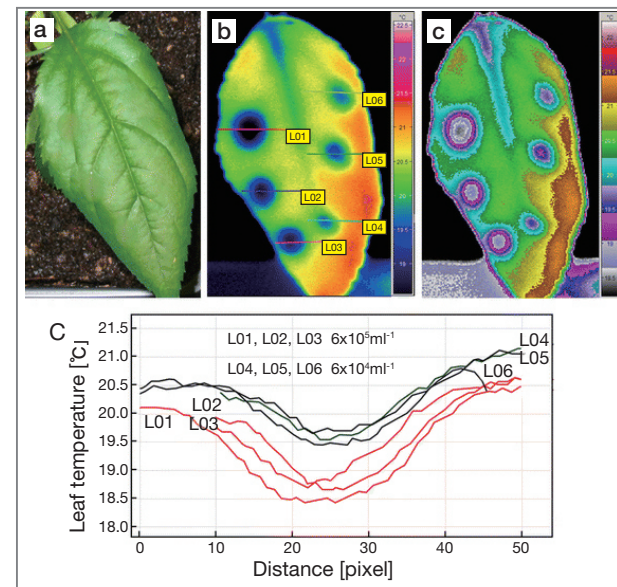

Figure 2. Effect of developing scab lesions caused by *Venturia inaequalis* on spatial heterogeneity in leaf temperature of apple leaves. First thermal effects became detectable 6 days after inoculation. RGB image (a), thermogram with transects (b), temperature profiles of transects through scab lesions (c).

with a specific phenotype. However, the emergence of omics (the collection of related data in a subject field) has provided a deluge of data to better understand phenomena that were previously elusive. Study of the interaction between phenomics and genomics has led to decoding the network of plant growth and yield. This information makes it possible to control a plant's growth with controlled environmental factors in an indoor farming system.

The observation of a phenotype involves a time-consuming and labor-intensive process because a person must observe and quantify results based on his/her knowledge of a certain trait. Even though traditional data gathering processes can produce some data points, the quality of data is often poor so that results are of questionable accuracy. Moreover, it is very difficult to convert human-collected data to homogeneous digital data. Recently, induvial plant leaf images were used to quantify the damaged caused by a pathogen present in certain plant diseases (Figure 2) [12]. This process represents digital phenotyping because it uses digital images to quantify a trait of interest. However, a more robust and high throughput manner of phenotyping is needed to study the interaction between phenotype and genotype.

A field within genetics involves the study of the function of individual genes in a given environment. This field has provided very rich information on gene function in the animal and plant kingdoms for a long time. During the last 15 years, genetic information has exploded due to the development and utilization of next-generation sequencing technologies. Second-generation sequencing technology captured lots of short-length DNA fragments while third-generation sequencing technology was able to capture very long DNA fragments. Both technologies were able to generate many data points and expedited the discovery of many gene functions, ushering in the era of genomics. As a result, a "phenotype bottleneck" has occurred because there is far less phenotype data than genotype (genomics) data [13]. This is one of

the key reasons for developing high throughput digital phenotyping called "plant phenomics" because only a small portion of genomics data has been utilized.

Development of plant phenomics system

A plant phenomics system for capturing the phenotypes of plants requires three key elements: a data acquiring system, sample position system, and analytical
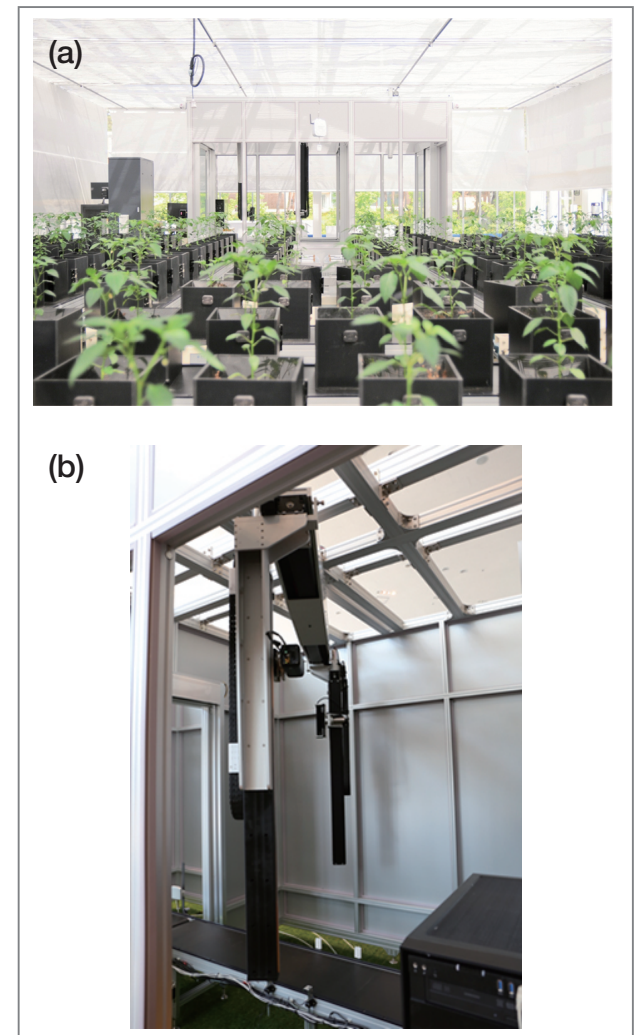

Figure 3. KIST's custom built plant-to-sensor type plant phenotyping platform: (a) layout of the whole system, (b) plant sample moved to the three dimensional (3D) stereo camera to obtain 3D images.

Figure 4. KIST's custom built sensor-to-plant type plant phenotyping platform.

software. Currently, the phenotypes of plants are measured by visible spectrum and non-visible spectrum. Visible digital images are utilized to examine plant growth patterns, disease susceptibility and yield outcomes, such as color and quantity of fruits. Non-visible images or outcomes are determined through energy displacement in a plant due to gas exchanges or photosynthetic activities. Early detection of biotic or abiotic stress from the environment is also possible with this approach. The phenotypes of plants can be acquired with two types of plant position systems, one where the samples are moved to a measuring device (Figure 3) or another where a device is moved to the samples (Figure 4). The first option produces better quality images because the images are obtained in the same location with the same setting, but the second option analyzes a greater number of samples.

Visible spectrum digital images distinguish observable traits with precision. The leaf area of a plant represents many traits at any growth stage. For example, one study linked leaf formation in the model plant *Arabidopsis* to enzymatic activities which were regulated by means of a feedback system [14]. The development of rosette-shape leaves was captured by taking high quality images every hour to provide fine detail of how leaf shapes and areas change over time. Another application tests a large number of plant samples inoculated against foliar disease.

This is important because to grow a large number of plants in a closed environment, plant diseases must be prevented by detecting symptoms at the earliest stages of infection.

Non-visible spectrum digital images provide key information about the physiology of a plant. Photosynthetic activities are essential to the health and yield of any crop. Photosynthetic activities are not detectable in visible spectrum ranges since two photosynthetic reactors are out of the visible spectrum. Specialized cameras, such as a pulse amplitude-modulated (PAM) fluorometry-enabled camera, are needed to study photosynthetic activities in a non-destructive way. In a gas exchange process, a plant has different temperature points due to water exchange activities. A thermal image captures temperature differences which can help to understand plant physiology. Multi-spectral image cameras detect plants' physiological changes, including stress responses from environmental factors. It uses wide ranges of a spectrum to detect plant images. The layers of images (different spectra) are more effective in distinguishing a plant's physiological responses than a single spectrum image (Figure 5) [15].

To date, there is no universal software to analyze the interaction between phenomic and genomic data. The main reason for this is that phenomics is new to many researchers and data do not yet have any standard to follow, unlike genomics data which can be evaluated via Phred quality scores. Some software has been developed
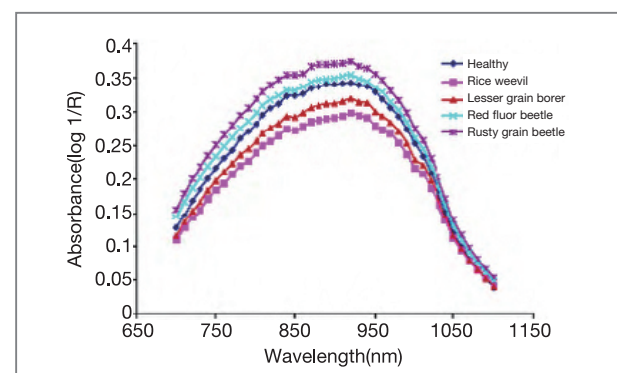

Figure 5. Short-wave near infrared absorbance mean spectra of healthy and insect-damaged wheat kernels.

to look at phenomics with genomics data, but only for limited functions. For example, PheWAS (phenome-wide association scan) has tried to capture single nucleotide polymorphism (SNP) association with disease phenotypes in humans [16]. Another software system, TraitCapture, utilizes genome-wide association studies (GWAS) with high throughput data to discover the genes underlying phenotype changes [17]. Both these software systems, however, are able to handle only two dimensional (2D), not three dimensional (3D) images, but 3D plant images provide very fine detail with multi-dimensional information on traits of interest. The software to handle such data has not yet been developed.

The phenomic approaches to find traits of interest in high throughput methods are gaining popularity. For example, a plant species called *Youngia denticulata* is known for health promoting effects such as protecting oxidative stress in a liver [18]. The species is from a wild and natural population growing in a mountainous area. In order to grow wild species in an indoor farming setting, many plant samples are needed to screen the shape of the plants due to genetic diversity within populations. A sensor-to-plant type plant phenomic system was utilized at KIST to screen seedlings of these plants (Figure 4). This method enables the screening of a large number of samples with precision. Later, a customized data analysis pipeline was selected for discarded plants from the processed dataset.

Conclusion

Even though indoor farming systems are not feasible for growing every crop, many vegetable crops can be grown well in such systems. The cost of growing crops in an indoor farming system is not inexpensive; however, a grower has the capacity to produce high quality vegetable crops and is not limited by seasonal constraints, so the investment cost can be recovered by the availability and high quality of the crop produced. Indoor farming has the

potential to be an important part of the food production process since the environment can be controlled. In order to control the indoor environment to support the continuous growth of crops, growers need to understand the optimal conditions for producing good quality fresh products. Continuous data should be acquired by studying the interaction between genomic and phenomic data every day. The concept of vertical indoor farming is also gaining popularity since it can scale up easily in urban environments. Regardless of the type of indoor farming system, data systems for growing plants with optimal quality and quantity are at the heart of the indoor farming system.

Finally, it is troubling but necessary to raise the spectre of worldwide food shortages. Climate change and the decrease of arable land space are threatening the world's crop production. Indoor farming represents one of the best options for raising crops to mitigate a potential global food crisis.

References

[1] Kozai T. Ohmsha 2012; *Plant Factory with Artificial Light*: 37-42.

[2] Kozai T. Ohmsha, 2012; *Plant Factory with Artificial Light*: 87.

[3] Wheeler RM, Martin-Brennan C. *NASA Tech. Mem.* 2000: 208577.

[4] Takayama K, Omasa K. *Handbook of closed ecological system and ecological engineering*; 2015: 367-371.

[5] Fukuda K. *J. SHITA* 2015; 27(2): 55-60.

[6] Omasa K. ASABE, 2006; *CIGR Handbook of Agricultural Engineering* (IV Information Technology): 217-230.

[7] Nishina H. *Agriculture and Agricultural Science Procedia*. 2015; 3: 9-13.

[8] Takayama K, Nishina H. *Environ. Control Biol.* 2009; 47(2): 101-109.

[9] Fukuda H, Ichino T, Kondo T, Murase H. *Environ. Control Biol.* 2011; 49(2): 51-60.

[10] He J, Giusti MM. *Annual Review of Food Science and Technology* 2010; 1(1): 163-187.

[11] Chalker-Scott L. *Photochemistry and Photobiology* 1999; 70: 1-9.

[12] Mahlein AK, et al. *European Journal of Plant Pathology* 2012; 133(1): 197-209.

[13] Furbank RT, Tester M. *Trends in Plant Science* 2011; 16(12): 635-644.

[14] Bilsborough GD, et al. *Proceedings of the National Academy of Sciences* 2011; 108(8): 3424-3429.

[15] Singh CB, et al. *Computers and Electronics in Agriculture* 2010; 73(2): 118-125.

[16] Denny JC, et al. *Bioinformatics* 2010; 26(9): 1205-1210.

[17] Brown TB, et al. *Current Opinion in Plant Biology* 2014; 18: 73-79.

[18] Kang K, et al. *Journal of Medicinal Food* 2011; 14(10): 1198-1207.

[**Feature Articles**]

A Monolithic and Standalone Artificial Photosynthetic Device for Solar-Chemical Production

Byoung Koun Min
Clean Energy Research Center
bkmin@kist.re.kr

Introduction

The focus of this article is on KIST's efforts in investigating ways to produce energy and/or chemicals by using the most abundant energy resource on our planet, solar energy. Such a conversion method is often called artificial photosynthesis because it mimics the photosynthesis process in plants to produce hydrocarbon fuels, referred to as solar fuels, from sunlight, CO_2, and water [1].

Current energy as well as chemical production still depend heavily on traditional fossil fuels which can precipitate global climate changes due to their emission of greenhouse gases. However, harnessing solar energy to produce energy and/or chemicals from water and CO_2 could significantly alleviate a source of climate changes; therefore, artificial photosynthesis is an excellent candidate for future chemical production technology.

There have been various attempts to produce solar fuels artificially using multi-functional photocatalysts or photoelectrochemical devices [2, 3]. However, none of the solar fuel-generating systems developed to date have yet to perform efficiently, and in fact, show a poorer performance than natural photosynthesis. Photosynthesis efficiencies of common plant leaves are known to be lower than 1% due to inconsistent insolation and limited CO_2 concentration in the atmosphere [4]. Therefore, the first challenge is to make an artificial solar-fuel device whose efficiency is comparable to that produced in nature.

Design of artificial photosynthetic device

To design an efficient artificial photosynthetic device, it is worth revisiting the concept of solar-water splitting systems because significant research has been accomplished in this area over the 40 years since it was first demonstrated by Fujishima and Honda [5]. Rigid material requirements for solar-water splitting make it impossible to reach high solar-to-hydrogen (STH) conversion efficiencies solely with metal oxide photocatalytic materials in spite of the benefits associated with their low cost. On the other hand, solar-water splitting systems using photovoltaic (PV) technology incorporated within photoelectrodes have revealed relatively high efficiencies.

There are two approaches that can be applied to enhance STH efficiency. The operating point can be shifted to a higher current (short circuit current, I_{sc}, is the maximum) and lower voltage (minimizing input-energy) by: (1) reducing overpotentials for overall water-splitting on either an anode or cathode with a highly efficient electrocatalyst (EC) or (2) combining photocatalyst (PC) materials with a (photo)anode or (photo)cathode to utilize the charge separation at the photocatalyst/electrolyte junction. Notably, the use of PC is preferable over EC since water splitting at zero bias (in the absence of PV) is theoretically possible. This has triggered tremendous efforts to develop semiconductor PC materials, despite the technical difficulty with tandem integration [6, 7]. Therefore, structures for efficient solar-fuel devices have to be deliberately designed with a variety of material choices to be applicable for both systems (PV cell integrated with EC or PC).

KIST-developed artificial synthetic device

After closely reviewing the representative solar-water splitting systems mentioned above, we found that the PV part (p-n junction of semiconductors) and photocatalyst or electrocatalyst films ohmically connected in the electrolyte by a transparent conducting film, such as an indium tin oxide (ITO) layer, had much in common, as described schematically in Figure 1a. If a substrate such as glass has conductive properties on both sides, the substrate itself can be used as an ohmic contact between PV and photocatalytic or electrocatalytic film instead of the thin layer of a conducting material, suggesting that the PV part can be placed out of the electrolyte while still maintaining an ohmic connection with photocatalytic or electrocatalytic film through a conductive substrate, such as glass with an ITO layer on both sides, as shown in Figures 1b and 1c. This configuration has merit in terms of the durab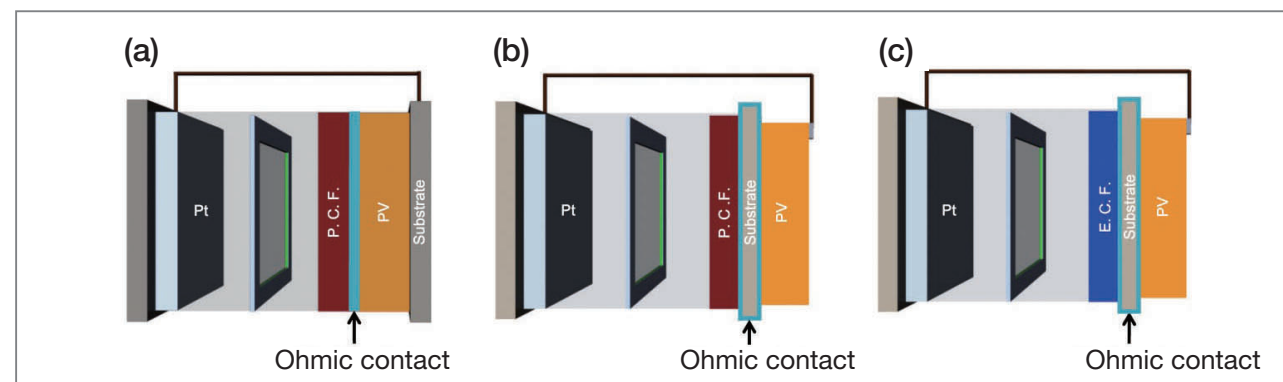ility of the PV part because it does not have direct contact with the electrolyte. In general, semiconductor materials, such as silicon and GaAs used in PV, are vulnerable in an aqueous electrolyte environment. In addition, the incident light can now reach the PV and PC films without absorption or scattering loss by the aqueous electrolyte, thus minimizing the efficiency loss of each integrated component.

To test the proposed configuration for artificial photosynthetic devices, we developed a model system, reflected in Figure 1c, that incorporates PV technology with EC. Specifically, we demonstrated a solar-fuel device with a parallel series connection of single junction PV cells as a module using a well-established module fabrication process to supply high enough energy for both water splitting and CO_2 reduction in the device, although there was some photocurrent loss due to reduction of the active area of the absorber film compared to the vertical series connection of single cells.

In our long journey to realize a highly efficient, low cost, outstandingly stable monolithic and standalone solar-fuel device, we herein demonstrate the first model of a solar-fuel device which has comparable solar-to-fuel conversion efficiency to that of photosynthesis in nature. In this device, $Cu(In_xGa_{1-x})(S_ySe_{1-y})_2$ (CIGS) thin film solar cell technology was applied in the PV part. On the reverse of this PV, electrocatalytic film (Co_3O_4) for water oxidation was monolithically prepared using a low-temperature coating method and nanostructured gold was applied as the electrocatalyst for selective reduction of CO_2 to CO.

Fabrication of the 1st model of the KIST-developed artificial synthetic device

One of the most important components in an artificial photosynthetic device is a photoelectrode that is capable of producing power by absorbing light. In this study, we employed a photoelectrode that was a combination of PV and electrocatalytic film on a single conducting glass substrate; one side formed the CIGS module for light absorption, the other side made the anode using Co_3O_4 nanoparticles as a catalyst for water oxidation (see Figure 2a). Moreover, in order to realize a cost effective fabrication of CIGS film, we adapted a paste-coating method which had been developed by our lab [8]. The average open circuit voltage (V_{oc}) of a single solar cell was measured to be 550 mV, and five single cells in parallel achieved a V_{oc} of over 2.70 V. The CIGS module was fabricated on a laser-patterned Mo substrate. The current–voltage (I–V) characteristic of the CIGS module had an efficiency of 8.58% with an open circuit voltage (V_{oc}), short circuit current (I_{sc}), and fill factor of 2.77 V, 9.74
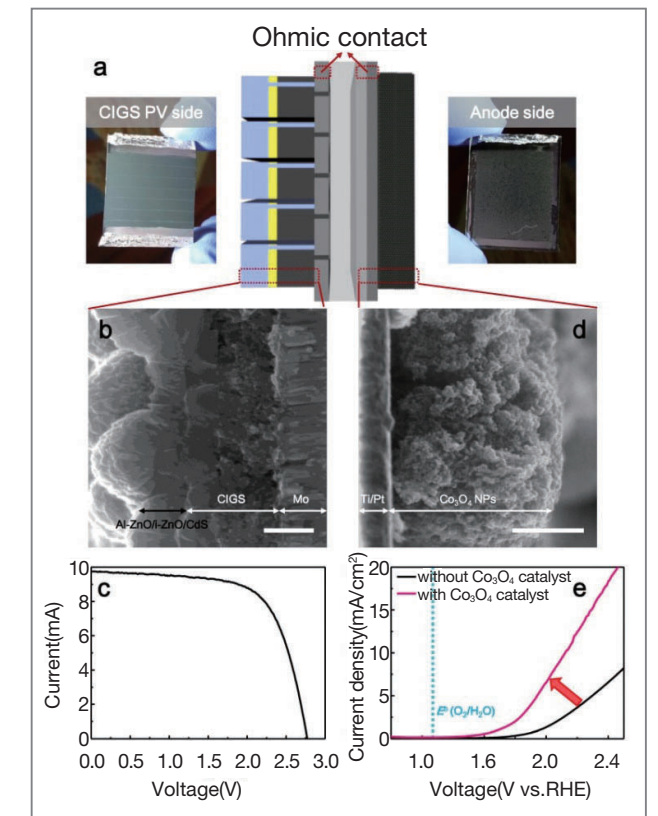
Figure 2. Monolithic CIGS module and Co_3O_4 anodic catalyst for photoelectrode. (a) Schematic diagram and photograph of a monolithically stacked photoelectrode with a CIGS PV module and Co_3O_4 film on each side of the glass substrate. (b) Cross-sectional SEM image of a CIGS PV cell (scale bar is 1μm). (c) Typical I-V characteristic of a CIGS module. (d) Cross-sectional SEM image of Co_3O_4 film on the glass/Ti/Pt substrate (scale bar is 1 μm). (e) Typical J-V characteristic with and without Co_3O_4 catalyst films.

Figure 1. (a) Solar-fuel device with photocatalytic film (P.C.F.) and internal PV. (b) Solar-fuel device with photocatalytic film (P.C.F.) and external PV. (c) Solar-fuel device with electrocatalytic film (E.C.F.) and external PV.

Figure 3. Nanostructured Au for cathodic catalyst. (a) SEM images of nanostructured Au cathodic catalyst. (b) Faradaic efficiency of H_2, CO, and formate at varying potential on nanostructured Au cathode for CO_2 reduction. (c) Total and partial current densities of H_2, CO, and formate at varying potential on nanostructured Au cathode for CO_2 reduction.

mA, and 66.9%, respectively (Figure 2c), implying that the V_{oc} of the individual single CIGS cell was successfully maintained in the module configuration.

Next, the electrocatalytic film for water oxidation was monolithically integrated with the prepared CIGS module. The catalytic function of the anode side for oxygen evolution is important for achieving a highly efficient reaction because of a large overpotential involved with the four-electron water oxidation process. A low-temperature coating method to deposit the catalyst at the reverse side is required to protect the pre-made CIGS module on the obverse side. For our device, we developed the catalyst film on glass/Ti/Pt substrate using a doctor blade coating method which employs Co_3O_4 nanoparticles as the oxygen evolution reaction (OER) catalysts and a Nafion solution as the binder material and subjected the film to a heat treatment at 70℃ [9]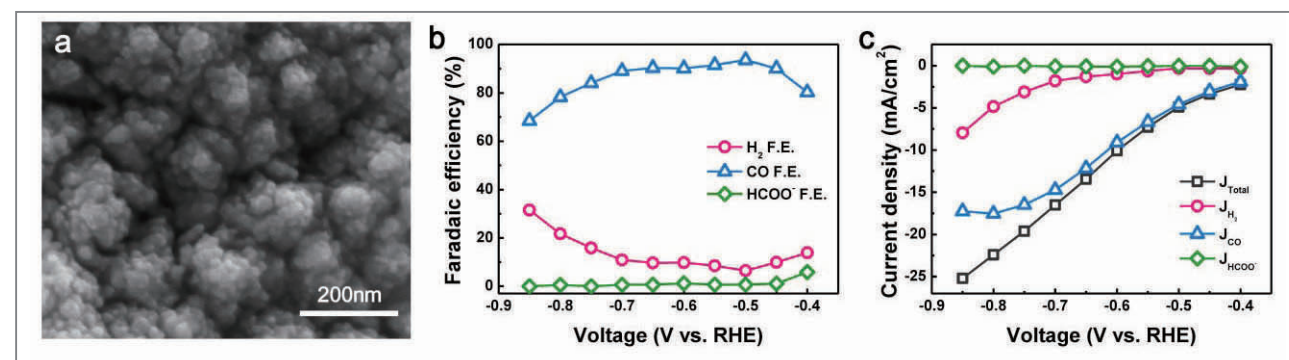. A thick film of approximately 2 μm of agglomerated Co_3O_4 nanoparticles of ~50 nm was observed in a cross-sectional SEM image (see Figure 2d), characterized by a porous morphology with high surface area. To investigate OER catalytic performance, linear sweep voltammetry (LSV) was performed in CO_2-saturated 0.5 M $KHCO_3$ electrolyte (see Figure 2e). The overpotential corresponding to 5 mA/cm^2 was decreased by 360 mV in the presence of the Co_3O_4 nanoparticle catalysts (from 2.30 V to 1.94 V vs. RHE).

A cathode for CO_2 reduction was fabricated with nanostructured gold foil which was synthesized based on the method developed by Chen et al. [10]. The synthesized nanostructured Au morphology was characterized by SEM, as shown in Figure 3a. We confirmed the surface layer formation with agglomerated tens of nanometer-sized Au particles. Figures 3b and 3c show Faradaic efficiencies for H_2, CO, and $HCOO^-$ and steady-state current densities of nanostructured Au with respect to potential from -0.39 V to -0.84 V vs. RHE in CO_2-saturated 0.5 M $KHCO_3$ electrolyte. Faradaic efficiency for CO had an optimal potential window from -0.44 V to -0.69 V, maintained at around 90 - 94%, but this started to decrease from potentials higher than -0.70 V. Considering that the thermodynamic equilibrium potential for CO_2 reduction to CO is -0.10 V vs. RHE, the overpotential at 5 $mA\ cm^{-2}$ was 400 mV.

The photoanode (CIGS PV + Co_3O_4 OER catalyst) and cathode (nanostructured Au) were then put together to be a monolithic solar-fuel device (see Figure 4a). Nafion membrane was installed between the anode and cathode to separate products from both electrodes and transfer protons from the anode to cathode as well. CO_2-saturated 0.5M $KHCO_3$ solution was used for both the anolyte and catholyte. The acrylic spacer was customized to hold the solution and the spacer and the electrodes were assembled with epoxy resin so that the produced gases could be collected. The device was directly connected
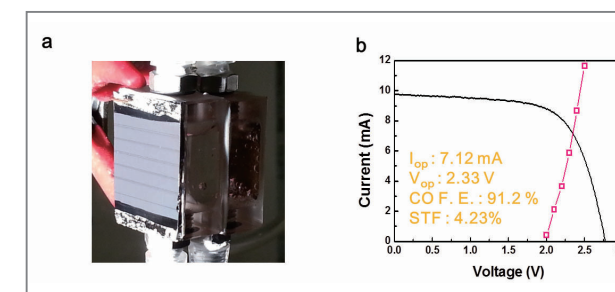

Figure 4. Solar-fuel device performance. (a) Photograph of illuminated solar-fuel device in operation, in which the CIGS module was incorporated at the external side of the PEC cell. (b) The operating point of the solar-fuel device under chopped light illumination.

to a gas chromatograph (GC) in order to determine the performance of the device in generating products.

To confirm the performance of the artificial photosynthetic device, the photocurrent was measured as matching the PV module and H_2O/CO_2 electrolysis current (see Figure 4b). Based on this data, the operating current was 7.32 mA with 91.2% CO F.E. A solar to CO conversion efficiency of 4.23% was achieved, which means that CO gas was produced at a rate of 0.4 uL s^{-1} cm^{-2}.

Conclusions

By using a low-cost solution-processed CIGS thin film solar cell module technology, low-temperature paste coating method of electrocatalytic film for water oxidation, and nanostructured Au cathode for CO_2 reduction, we developed a single solar-fuel device operating only by sunlight with a solar-to-fuel conversion efficiency of over 4%. This demonstration is just our first step in producing a highly efficient monolithic and standalone solar-fuel device. Our work to achieve even higher efficiency by reducing the overpotential for water oxidation in the electrolyte will continue.

Note

This article and images are drawn from "A monolithic and standalone solar-fuel device having comparable efficiency to photosynthesis in nature" in *J. Mater. Chem. A*, Vol. 3, pg 5835.

References

[1] Gust D, Moore TA, Moore AL. *Acc. Chem. Res.* 2009; 42(12): 1890-1898.

[2] Tong H, Ouyang S, Bi Y, Umezawa N, Oshikiri M, Ye J. *Adv. Mater.* 2012; 24(2): 229-251.

[3] Bensaid S, Centi G, Garrone E, Perathoner S, Saracco G. *ChemSusChem.* 2012; 5(3): 500-521.

[4] Blankenship RE, Tiede DM, Barber J, Brudvig GW, Fleming G, Ghirardi M, Gunner MR, Junge W, Kramer DM, Melis A, Moore TA, Moser CC, Nocera DG, Nozik AJ, Ort DR, Parson WW, Prince RC, Sayre RT. *Science* 2011; 332(6031): 805-809.

[5] Fujishima A, Honda K. *Nature* 1972; 238(5358): 37-38.

[6] Nozik AJ. *Appl. Phys. Lett.* 1977; 30(11): 567-569.

[7] Minggu LF, Wan Daud WR, Kassim MB. Int. *J. Hydrogen Energy* 2010; 35(11): 5233-5244.

[8] Park SJ, Cho JW, Lee JK, Shin K, Kim JH, Min BK. *Prog. Photovolt Res. Appl.* 2014; 22(1): 122-128.

[9] Jeon HS, Park W, Kim J, Kim H, Kim W, Min BK. *Int. J. Hydrogen Energy* 2011; 36(3): 1924-1929.

[10] Chen Y, Li CW, Kanan MW. *J. Am. Chem. Soc.* 2012; 134(49): 19969-19972.

[**Feature Articles**]

Pathogen Detection Using Aptamer-Conjugated Fluorescent Nanoparticles on an Optofluidic Platform

Byoung Chan Kim
Center for Environment, Health and Welfare Research
bchankim@kist.re.kr

Jaehee Jung
Center for Environment, Health and Welfare Research
jaehee@kist.re.kr

Introduction

Water contamination with hazardous microorganisms poses serious health risks and is a critical concern in the field of public health and safety [1-3]. Thus, the early detection and identification of pathogenic microorganisms are essential for clinical diagnosis, aqueous environmental analysis, and food safety [2, 4].

Ideal sensors for the early detection of hazardous microorganisms should be selective, fast, inexpensive, and quantitative. Various approaches, such as direct culture-based colony counting methods or the polymerase chain reaction (PCR), have been used to detect hazardous microorganisms [5-7]. However, the colony-counting method lacks selectivity in detecting target bacteria with unknown samples and requires relatively long incubation times for bacteria to reach detectable levels, normally one or more days. PCR is a very sensitive method for detecting specific microorganisms at the DNA or RNA level; however, it requires pretreatment steps such as purification and cell lysis, which hinder continuity in the process of detecting bacteria. Generally, the overall PCR process requires more than two hours.

Antibodies are frequently used receptors for rapid, non-lytic, and selective detection of bacteria. Many immunoassay methods using antibodies have been developed, such as the enzyme-linked immunosorbent assay (ELISA), radioimmunoassay (RIA), and fluorescence antibody (FA) techniques [8-10]. To date, the results of several studies have demonstrated the feasibility of detecting bacteria with bacteria-specific antibodies and optofluidic systems [11, 12]. However, the production of antibodies depends first upon the generation of biological immune responses, which is not applicable in cases where the pathogens of interest are non-immunogenic [13-15]. Moreover, the process of antibody production and purification requires animal care facilities and the sacrifice of animals, which limits productivity and increases the cost of antibodies. Another disadvantage associated with antibodies is that they cannot be used under harsh conditions, such as high temperature [16].

To overcome the drawbacks of the various detection methods discussed above, we developed a bacterial target specific (*E. coli*) aptamer-conjugated fluorescent nanoparticle (A-FNP) and optofluidic detection platform for fast, continuous, and inexpensive single-cell detection without cell lysis or disruption. Aptamers are polynucleic acids capable of folding to form specific 3-dimensional structures that bind target microorganisms with nano to picomolar affinity [17-20]. Furthermore, aptamers are synthesized by *in vitro* processes that can be easily scaled up and involve lower costs than those incurred by antibody production; they can also be used under harsh conditions [21]. Optofluidic platforms, which consist of microfluidic channel and fiber optics, can provide fast particle-detection performance and continuous single-cell controllability. In addition, the amount of reagents required for labeling the target microbes is significantly reduced in microfluidics platforms (Figure 1).

Results and discussion

First, we fabricated A-FNPs, wherein *E. coli*-specific aptamers were conjugated to the surface of nano-sized fluorescence beads [22]. Because *E. coli* is frequently present in water supplies, along with other pathogenic microorganisms [2, 23], *E. coli* is regarded as an important indicator strain on the monitoring of microbial contamination in drinking water. Binding of the A-FNPs to target *E. coli* cells was verified by imaging with fluorescence microscopy and SEM. Fluorescent images were observed only in samples containing target *E. coli* cells (Figure 2A). SEM images confirmed that A-FNPs were only bound to the surfaces of *E. coli* (Figure 2B). The selectivity of A-FNPs was examined by comparing fluorescence intensities following binding to *E. coli* to those obtained using the same concentration of A-FNPs incubated with other strains of coliform bacteria (*E. aerogenes* and *C. freundii*). Fluorescence intensities

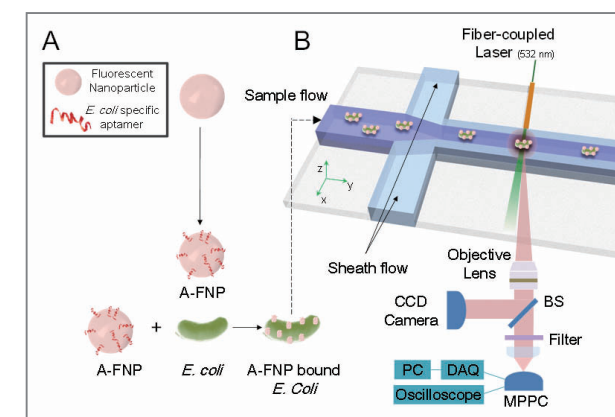**Figure 1.** Schematics of the present microbe detection system. (A) Preparation of aptamer conjugated fluorescent nanoparticles (A-FNPs). (B) Detection of A-FNP-bound *E. coli* by the microchannel and optical particle counter.
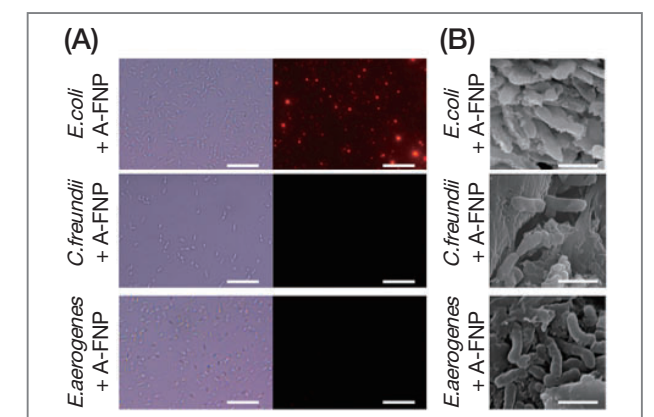

Figure 2. Digital images of A-FNPs bound to the surfaces of bacteria, using (A) a fluorescence microscope and (B) a scanning electron microscope. Scale bars: (A) 20 μm and (B) 2 μm.

of A-FNPs incubated with these species were below the detection limits of the fluorospectrometer, while the fluorescence intensity of A-FNP-*E. coli* complexes was relatively high (Figure 3A). Increasing numbers of bacterial cells were incubated with a constant A-FNP concentration to evaluate the possibility of using A-FNPs for quantitative analysis. The fluorescence intensities of A-FNPs bound to bacteria were dependent upon the number of labeled bacterial cells (Figure 3B). As the *E. coli*-specific A-FNPs displayed high affinity and selectivity, they were ready to
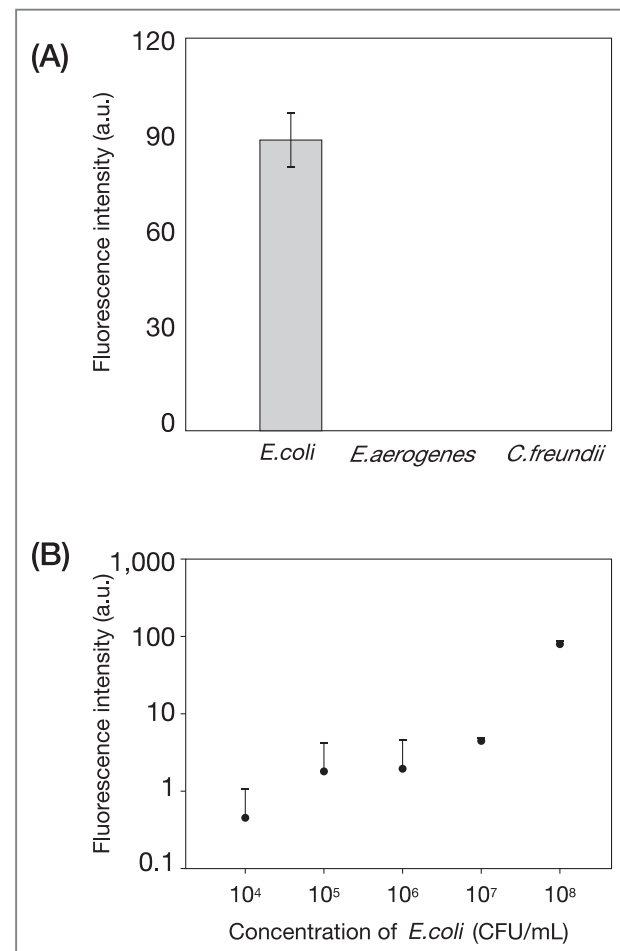
be adapted to the optofluidic system (Figure 1).

A continuous single-cell detection method based on A-FNPs was developed with a microfluidic platform and an optical system (Figure 1). In this system, target microbes bound to A-FNPs are continuously injected into a microchannel and passed into a detection zone. A-FNP-bound microorganisms continuously emit fluorescent signals when exposed to excitation light in the detection zone. Figure 4A shows the results of an experiment during the initial one second so that individual peaks
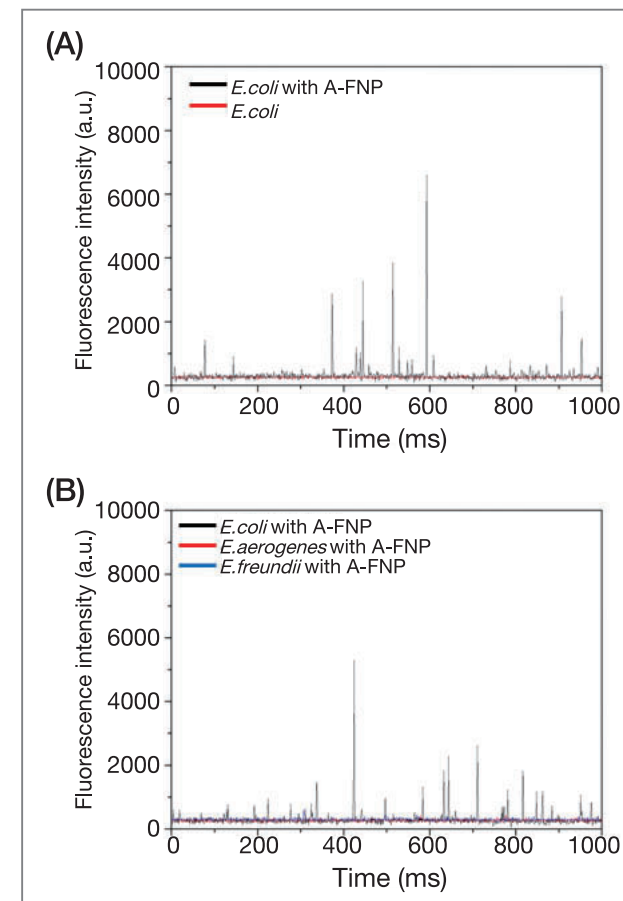

Figure 3. Characterization of A-FNP binding by (A) determining A-FNP selectivity for *E. coli* and (B) measuring A-FNP binding with increasing *E. coli* CFUs. (A) A-FNPs bound specifically to *E. coli*, but not other strains. (B) Fluorescence intensities were dependent upon the number of bacterial cells tested, indicating that A-FNPs can potentially be used for quantitative assays.

Figure 4. Continuous detection of microbes by using microfluidics and an optical particle counter. (A) Binding tendency test results for A-FNP-*E. coli* complexes or *E. coli* alone for an initial 1-second measurement period. (B) A-FNP selectivity test results of the present method using *E. coli*, *E. aerogenes*, or *C. freundii* and an initial 1-second measurement period.
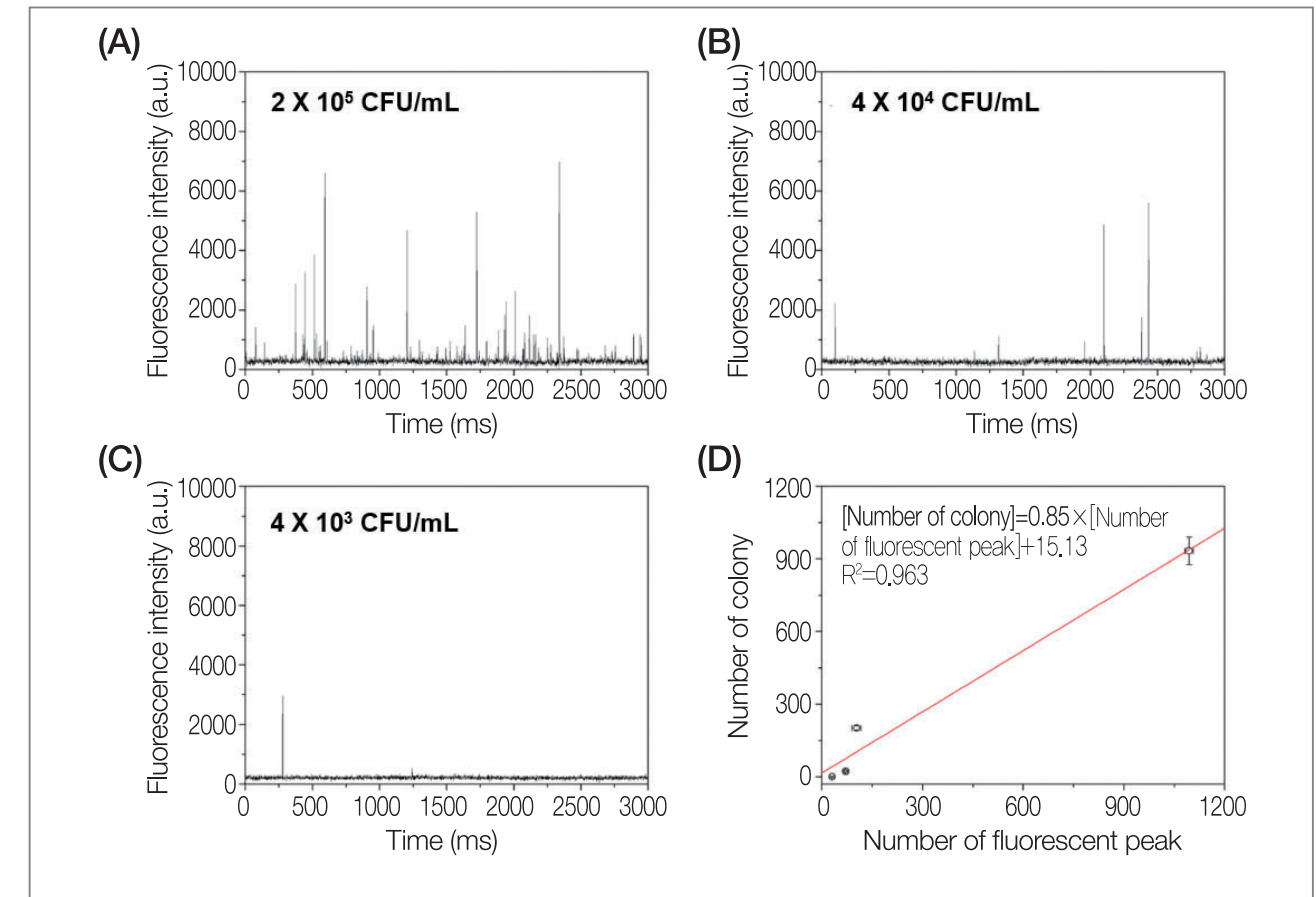
Figure 5. Detection of A-FNP binding to increasing *E. coli* CFUs over an initial 3-second measurement period. The *E. coli* concentrations of each sample were approximately (A) 2×10^5 CFU/mL, (B) 4×10^4 CFU/mL, and (C) 4×10^3 CFU/mL. (D) Comparison of results from the present microbe detection method with those of a conventional colony counting method.

can be identified. A total of 1045 fluorescent peaks were observed over 180 seconds when analyzing *E. coli* bound to A-FNPs. However, no remarkable fluorescent peaks were detected over 180 seconds for an unlabeled *E. coli* sample because the present system detects fluorescence emitted from A-FNPs bound to *E. coli*. Because unbound A-FNPs were washed away during the pretreatment process, each fluorescent peak observed was considered as a single *E. coli* cell bound with A-FNPs that passed the detection zone in the microchannel. These results indicate that the optical particle counter can continuously detect A-FNP-labeled target bacteria in real time. Figure 4B shows the results of experiments designed to test the

selectivity of A-FNPs in the continuous detection system for one second. A-FNPs bound to *E. coli* showed 1045 fluorescent peaks over 180 seconds. However, 10 and 2 peaks were observed with A-FNP-stained *E. aerogenes* and *C. freundii* samples over 180 seconds, respectively. These results directly indicate that A-FNPs selectively labeled target *E. coli* bacteria and that the optical particle counter can differentiate selectively labeled microbes in a sample.

Figure 5 shows quantitative analysis of results obtained with the present optofluidic system, using *E. coli* concentration of 2×10^5, 4×10^4, and 4×10^3 CFU/mL. The number of A-FNP-labeled *E. coli* cells detected over a

180-second measurement interval in the present system was 1045, 105, and 61, respectively, and the results for the initial three seconds are shown in Figures 5A, 5B, and 5C. To verify that the present system quantitatively detects single bacteria cells, the number of bacteria detected with the present method was compared with the colony counting method. The amount of *E. coli* used in colony counting was calculated according to the following formula: number of total bacterial colonies = concentration of each sample × microchannel flow rate × detection time. The number of fluorescent peaks measured by the present system and the number of CFUs counted by the colony counting method both increased in proportion to the increased number of single bacterial cells analyzed. The slope of the linear regression between the number of CFUs and the number of fluorescent peaks was 0.85 (Figure 5D). Thus, these results show that the single cell detection method using A-FNPs and the optofluidic system in the present study is well matched with the plate counting method.

Conclusions

In this study, we demonstrated the development of a continuous, non-lytic, and rapid single-cell *E. coli* optofluidic detection system using *E. coli*-specific A-FNPs and an optical particle counter connected to a microfluidic channel. A-FNPs bound to *E. coli* with high affinity and selectivity. Consequently, we achieved a detection rate of ~100 *E. coli* / second using single *E. coli* cells. Moreover, the number of *E. coli* cells detected by the present platform corresponded well to the results obtained using the colony counting method, a conventional culture-based detection protocol. This platform may have potential for the development of portable-sized equipment to perform on-site detection.

Note

This article and images are drawn from "Fast and continuous microorganism detection using aptamer-conjugated fluorescent nanoparticles on an optofluidic platform" in *Biosensors and Bioelectronics* 2015, Vol. 67, p. 303.

References

[1]   Katukiza AY, Ronteltap M, van der Steen P, Foppen JWA, Lens PNL. *J. Appl. Microbiol.* 2014; 116 (2): 447-463.

[2]   Leclerc H, Mossel DAA, Edberg SC, Struijk CB. *Annu. Rev. Microbiol.* 2001; 55(1): 201-234.

[3]   Szewzyk U, Szewzyk R, Manz W, Schleifer K-H. *Annu. Rev. Microbiol.* 2000; 54 (1): 81-127.

[4]   Torres-Chavolla E, Alocilja EC. *Biosen. Bioelectron.* 2009; 24 (11): 3175-3182.

[5]   Cheng JC, Huang CL, Lin CC, Chen CC, Chang YC, Chang SS, Tseng CP. *Clin. Chem.* 2006; 52 (11): 1997-2004.

[6]   de Boer E, Beumer RR. *Int. J. Food Microbiol.* 1999; 50 (1–2): 119-130.

[7]   Rodriguez GG, Phipps D, Ishiguro K, Ridgway HF. *Appl. Environ. Microbiol.* 1992; 58 (6): 1801-1808.

[8]   Czerkinsky C, Rees A, Bergmeier L, Challacombe S. *Clin. Exp. Immunol.* 1983; 53(1): 192-200.

[9]   Delehanty JB., Ligler FS. *Anal. Chem.* 2002; 74 (21): 5681-5687.

[10] Swanink CM, Meis JF, Rijs AJ, Donnelly JP, Verweij PE. *J. Clin. Microbiol.* 1997; 35 (1): 257-260.

[11] Sakamoto C, Yamaguchi N, Nasu M. *Appl. Environ. Microbiol.* 2005; 71 (2): 1117-1121.

[12] Zhao X, Hilliard LR, Mechery SJ, Wang Y, Bagwe RP, Jin S, Tan W. *Proc. Natl. Acad. Sci. USA.* 2004; 101 (42): 15027-15032.

[13] Levy-Nissenbaum E, Radovic-Moreno AF, Wang AZ, Langer R, Farokhzad OC. *Trends Biotechnol.* 2008; 26 (8): 442-449.

[14] Luzi E, Minunni M, Tombelli S, Mascini M. *TrAC-Trend Anal. Chem.* 2003; 22 (11): 810-818.

[15] Tombelli S, Minunni M, Mascini M. *Biosens. Bioelectron.* 2005; 20 (12): 2424-2434.

[16] Jayasena SD. *Clin. Chem.* 1999; 45 (9): 1628-1650.

[17] Bock LC, Griffin LC, Latham JA, Vermaas EH, Toole JJ. *Nature.* 1992; 355: 564-566.

[18] Degefa TH, Kwak J. *Anal. Chim. Acta.* 2008; 613 (2): 163-168.

[19] Du Y, Li B, Wei H, Wang Y, Wang E. *Anal. Chem.* 2008; 80 (13): 5110-5117.

[20] Kim YS, Chung J, Song MY, Jurng J, Kim BC. *Biosen. Bioelectron.* 2014; 54: 195-198.

[21] Zhou J, Battig M, Wang Y. *Anal. Bioanal. Chem.* 2010; 398 (6): 2471-2480.

[22] Kim YS, Song MY, Jurng J, Kim BC. *Anal. Biochem.* 2013; 436(1): 22–28

[23] Edberg SC, Rice EW, Karlin RJ, Allen MJ. *J. Appl. Microbiol.* 2000; 88 (S1): 106S-116S.

Characterization of topographically specific sleep spindles in mice

Dongwook Kim, Eunjin Hwang, Mina Lee, Hokun Sung, Jee Hyun Choi(jeechoi@kist.re.kr)

Study Objective: Sleep spindles in humans have been classified as slow anterior and fast posterior spindles; recent findings indicate that their profiles differ according to pharmacology, pathology, and function. However, little is known about the generation mechanisms within the thalamocortical system for different types of spindles. In this study, we aim to investigate the electrophysiological behaviors of the topographically distinctive spindles within the thalamocortical system by applying high-density EEG and simultaneous thalamic LFP recordings in mice.

Design: 32-channel extracranial EEG and 2-channel thalamic LFP were recorded simultaneously in freely behaving mice to acquire spindles during spontaneous sleep.

Subjects: Hybrid F1 male mice of C57BL/6J and 129S4/svJae.

Measurements and Results: Spindle events in each channel were detected by a spindle detection algorithm, and then a cluster analysis was applied to classify the topographically distinctive spindles. All sleep spindles were successfully classified into 3 groups: anterior, posterior, and global spindles. Each spindle type showed distinct thalamocortical activity patterns regarding the extent of similarity, phase synchrony, and time lags between cortical and thalamic areas during spindle oscillation. We also found that sleep slow waves were likely to associate with all types of sleep spindles, but also that the ongoing cortical decruitment/recruitment dynamics before the onset of spindles and their relationship with spindle generation were also variable, depending on spindle type.

Conclusion: Topographically specific sleep spindles show distinctive thalamocortical network behaviors.

Induced phenotype targeted therapy: radiation-induced apoptosis-targeted chemotherapy

Beom Suk Lee, Yong Woo Cho, Gui Chul Kim, Do Hee Lee, Chang Jin Kim, Hee Seup Kil, Dae Yoon Chi, Youngro Byun, Soon Hong Yuk, Kwangmeyung Kim, In-San Kim, Ick Chan Kwon(ikwon@kist.re.kr), Sang Yoon Kim

Background: Tumor heterogeneity and evolutionary complexity may underlie treatment failure in spite of the development of many targeted agents. We suggest a novel strategy termed induced phenotype targeted therapy (IPTT) to simplify complicated targets because of tumor heterogeneity and overcome tumor evolutionary complexity.

Methods: We designed a caspase-3 specific activatable prodrug, DEVD-S-DOX, containing doxorubicin linked to a peptide moiety (DEVD) cleavable by caspase-3 upon apoptosis. To induce apoptosis locally in the tumor, we used a gamma knife which can irradiate a very small, defined target area. The in vivo antitumor activity of the caspase-3–specific activatable prodrug combined with radiation was investigated in C3H/HeN tumor-bearing mice (n = 5 per group) and analyzed with the Student's t test or Mann-Whitney U test. All statistical tests were two-sided. We confirmed the basic principle using a caspase-sensitive nanoprobe (Apo-NP).

Results: A single exposure of radiation was able to induce apoptosis in a small, defined region of the tumor, resulting in expression of caspase-3. Caspase-3 cleaved DEVD and activated the prodrug. The released free DOX further activated DEVDS-DOX by exerting cytotoxic effects on neighboring tumor or supporting cells, which repetitively induced the expression of caspase-3 and the activation of DEVD-S-DOX. This sequential and repetitive process propagated the induction of apoptosis. This novel therapeutic strategy showed not only high efficacy in inhibiting tumor growth (14-day tumor volume [mm3] vs radiation alone: 848.21 ± 143.24 vs 2511.50 ± 441.89, P < .01) but also low toxicity to normal cells and tissues.

Conclusion: Such a phenotype induction strategy represents a conceptually novel approach to overcome tumor heterogeneity and complexity as well as to substantially improve current conventional chemoradiotherapy with fewer sequelae and side effects.

Tailor-made polyamide membranes for water desalination

Wansuk Choi, Joung-Eun Gu, Sang-Hee Park, Seyong Kim, Joona Bang, Kyung-Youl Baek, Byoungnam Park, Jong Suk Lee(jong.lee@kist.re.kr), Edwin P. Chan, Jung-Hyun Lee

Independent control of the extrinsic and intrinsic properties of the polyamide (PA) selective layer is essential for designing thin-film composite (TFC) membranes with the performance characteristics required for water purification applications in addition to seawater desalination. Current commercial TFC membranes fabricated via the well-established interfacial polymerization (IP) approach yield materials that are far from ideal because their layer thickness, surface roughness, polymer chemistry, and network structure cannot be separately tailored. In this work, tailor-made PA-based desalination membranes based on molecular layer-by-layer (mLbL) assembly are presented.

The mLbL technique enables the construction of an ultrathin and highly cross-linked PA selective layer in a precisely and independently controlled manner. The mLbL-assembled TFC membranes exhibit significant enhancements in performance compared to their IP-assembled counterparts. A maximum sodium chloride rejection of 98.2% is achieved along with over 2.5 times higher water flux than the IP-assembled counterpart. More importantly, this work demonstrates the broad applicability of mLbL in fabricating a variety of PA-based TFC membranes with nanoscale control of the selective layer thickness and roughness independent of the specific polyamide chemistry.

High-concentration boron doping of graphene nanoplatelets by simple thermal annealing and their supercapacitive properties

Da-Young Yeom, Woojin Jeon, Nguyen Dien Kha Tu,
So Young Yeo, Sang-Soo Lee, Bong June Sung,
Hyejung Chang, Jung Ah Lim(jalim@kist.re.kr), Heesuk Kim

To use graphene in various energy storage and conversion applications, it must be synthesized in bulk with reliable and controllable electrical properties. Although nitrogen-doped graphene shows a high doping efficiency, its electrical properties can be easily affected by oxygen and water impurities from the environment. We here report that boron-doped graphene nanoplatelets with desirable electrical properties can be prepared by the simultaneous reduction and boron-doping of graphene oxide (GO) at a high annealing temperature. B-doped graphene nanoplatelets prepared at 1000°C show a maximum boron concentration of 6.04 ± 1.44 at %,

which is the highest value among B-doped graphenes prepared using various methods. With well-mixed GO and g-B2O3 as the dopant, highly uniform doping is achieved for potentially gram-scale production. In addition, as a proof-of-concept, highly B-doped graphene nanoplatelets were used as an electrode of an electrochemical double-layer capacitor (EDLC) and showed an excellent specific capacitance value of 448 F/g in an aqueous electrolyte without additional conductive additives. We believe that B-doped graphene nanoplatelets can also be used in other applications such as electrocatalysts and nano-electronics because of their reliable and controllable electrical properties regardless of the outer environment.
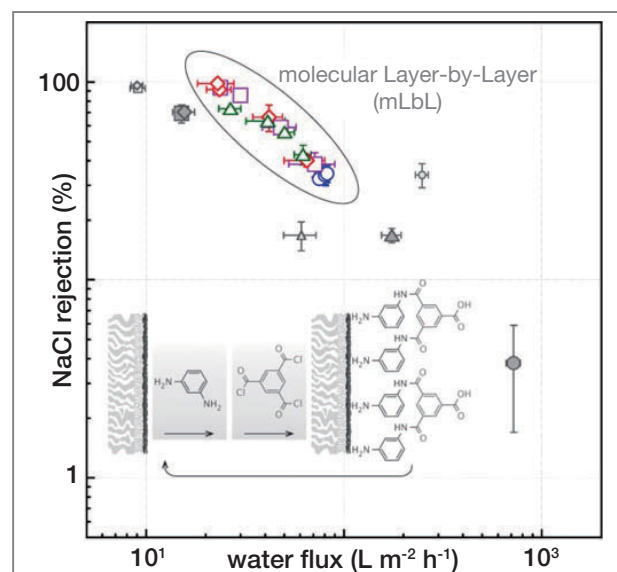
Self-assembled block copolymer micelles with silver–carbon nanotube hybrid fillers for high performance thermal conduction

Jae Ryung Choi, Seunggun Yu, Haejong Jung,
Sun Kak Hwang, Richard Hahnkee Kim, Giyoung Song,
Sung Hwan Cho, Insung Bae, Soon Man Hong,
Chong Min Koo(koo@kist.re.kr), Cheolmin Park

The development of polymer-filled composites with an extremely high thermal conductivity (TC) that is competitive with conventional metals is in great demand due to their cost-effective process, light weight, and easy shape-forming capability. A novel polymer composite with a large thermal conductivity of 153 W m^{-1} K^{-1} was prepared based on self-assembled block copolymer micelles containing two different fillers of micron-sized silver particles and multi-walled carbon nanotubes. Simple mechanical mixing of the components followed by conventional thermal compression at a low processing temperature of 160°C produced a novel composite with both structural and thermal stability that is durable for high temperature operation up to 150°C as well as multiple heating and cooling cycles of $\Delta T = 100$°C. The high performance in thermal conduction of our composite was mainly attributed to the facile deformation of Ag particles during the mixing in a viscous thermoplastic medium, combined with networked carbon nanotubes uniformly dispersed in the nanoscale structural matrix of block copolymer micelles responsible for its high temperature mechanical stability. Furthermore, micro-imprinting on the composite allowed for topographically periodic surface micropatterns, which offers broader suitability for numerous micro-opto-electronic systems.

Photo-oxidation activities on Pd-doped TiO$_2$ nanoparticles: critical PdO formation effect

Hangil Lee, Minjeong Shin, Myungjin Lee,
Yun Jeong Hwang(yjhwang@kist.re.kr)

The catalytic activities of three distinct Pd-doped TiO$_2$(PdTiO$_2$) nanoparticle samples, post-annealed (at 700, 800, and 900°C) after fabrication on silicon substrates, were analyzed with respect to the photo-oxidation of aniline and 2-thiophenecarboxaldehyde. Through a combination of Raman spectroscopy and high-resolution photoemission spectroscopy (HRPES), we demonstrated that the photocatalytic oxidation occurred only when the PdTiO$_2$ nanoparticles were annealed at temperatures above 800°C, that is,when PdO and Ti3+had partially formed on the PdTiO$_2$ nanoparticles, which indicates that the presence of PdO and Ti3+is critical for the photocatalytic oxidation. Additionally, we determined the decrease in the band gaps to visible regions with PdTiO$_2$ nanoparticles annealed above 800°C from their valence-band spectra, which resulted in photocatalytic activities even under visible light, = 540 nm.

Air foil bearing having pressure dam

US 9004765 (2015-04-14)

Lee Yong Bok / lyb@kist.re.kr

This air foil bearing has a bearing housing with a shaft hole in which a rotary shaft is inserted and a top foil is fixed to the shaft hole to support the circumference of the rotary shaft. An air flow path is formed at the top foil by means of a plurality of dams protruding on the inner surface of the top foil. The air flow path is formed so that air between the top foil and the rotary shaft flows along the circumference of the inner surface of the top foil

Molten carbonate fuel cells including reinforced lithium aluminate matrix, method for preparing the same, and method for supplying lithium source

US 8999598 (2015-04-07)

Yoon Sung Pil / spyoon@kist.re.kr

Disclosed is a molten carbonate fuel cell comprising a reinforced lithium aluminate matrix, a cathode, an anode, a cathode frame channel and an anode frame channel, wherein at least one of the cathode frame or anode frame channels is filled with a lithium source. Disclosed also are methods for producing the same and supplying a lithium source. The molten carbonate fuel cell in which a lithium source is supplied to an electrode has high mechanical strength and maintains stability of the electrolyte to allow long-term operation.

Conductive ink composition, method for manufacturing the same, and method for manufacturing conductive thin layer using the same

US 8999204 (2015-04-07)

Hong Jae-Min / jmhong@kist.re.kr

Disclosed is a conductive ink composition, a manufacturing method thereof, and a manufacturing method for a conductive thin film using the same. More specifically, a conductive ink composition is provided that includes composite metal nanoparticles, including first metal nanoparticles and second metal nanoparticles, and a polymer matrix. The polymer matrix is a composition which includes a polymer and a solvent, the first metal nanoparticles and the second metal nanoparticles are different metals, and the content of the composite metal nanoparticles is about 20 to 25 wt %, the content of the polymer is about 5 to 10 wt %, and the content of the solvent is about 65 to 75 wt %, based on the total weight of the composition.

Apparatus and method for manufacturing composite nano particles

US 8940240 (2015-01-27)

Jurng Jong Soo / jongsoo@kist.re.kr

Disclosed are an apparatus and a method for manufacturing composite nanoparticles. The apparatus comprises: a first precursor supply unit vaporizing a first precursor and supplying it to a reaction unit; a second precursor supply unit vaporizing a second precursor and supplying it to the reaction unit; the reaction unit producing composite nanoparticles by reacting the vaporized first precursor with the vaporized second precursor; an oxygen supply line supplying an oxygen source to the reaction unit; and a collection unit collecting the composite nanoparticles produced by the reaction unit. Since gas phase synthesis occurs in different stages using the U-shaped reaction chamber, aggregation is prevented and composite nanoparticles of uniform size and high specific surface area can be produced easily.

Apparatus for gas sensing by using fiber fabry-perot interferometer

The present invention relates to an apparatus for gas sensing which includes: (1) a header part to generate an interference wave to light from a light source by the principle of a fiber fabry-perot interferometer; and (2) an optical spectrum analyzer to confirm the existence of specific gases based on changes of spectrum periodicity of the interference wave. The header part includes a sensing material that expands or shrinks in the presence of specific gases and the above interference wave changes its spectrum periodicity depending on the expansion or shrinkage of the above sensing material.
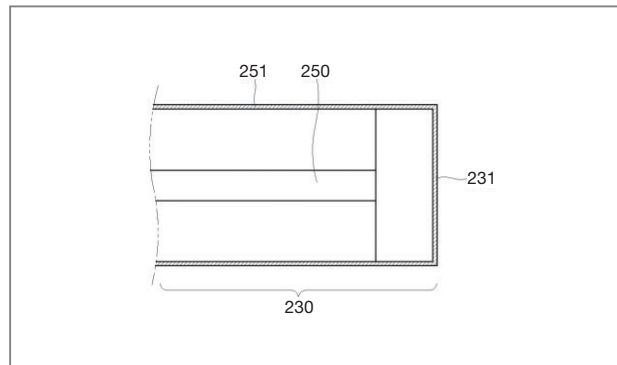
Apparatus and method for anaerobic wastewater treatment with membrane

The present disclosure relates to an apparatus and method for anaerobic wastewater treatment with a membrane, which effectively generates biogas and suppresses fouling on a membrane surface by performing anaerobic treatment to wastewater. The apparatus for anaerobic wastewater treatment with a membrane includes: an anaerobic reactor for performing anaerobic treatment to wastewater and generating biogas; an anaerobic membrane bio-reactor for filtering wastewater discharged from the anaerobic reactor by means of a membrane module and providing an additional anaerobic treatment space for the wastewater; submerged membrane modules provided in the anaerobic membrane bio-reactor to filter wastewater; rotating disks provided at both sides of the submerged membrane module to induce turbulence to the wastewater by means of rotation; and a second medium provided in the anaerobic membrane bio-reactor to circulate according to the flow of the wastewater so that foulants on a surface of the membrane module are detached.
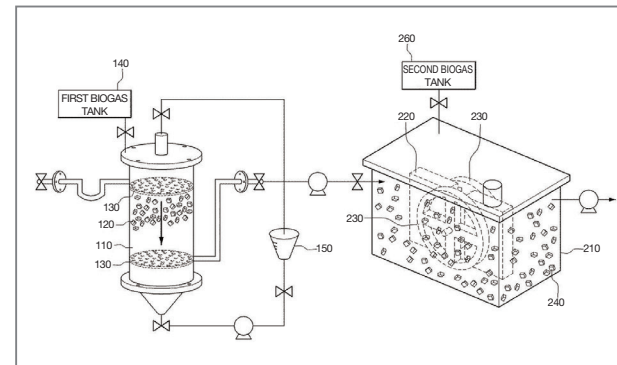
Head mounted display and method for displaying contents using the same

A head mounted display and a method of displaying content using the head mounted display are disclosed. The head mounted display includes a display unit displaying content and a first lens unit configured by a set of lens elements that refracts the content displayed on the display unit in an eyeball direction.
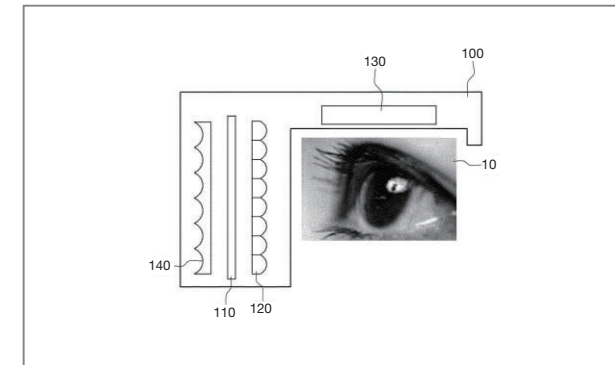
1. Nanometer Catalyst Effectively Eliminates Harmful Substances from Air in Rooms Used by Smokers
April 21, 2015

A KIST research team has developed a nano-catalyst for cleaning the air in rooms used by smokers. It removes 100% of the acetaldehyde, a first class carcinogen, which accounts for the largest portion of the gaseous substances present in cigarette smoke. The KIST-developed catalyst also removes 100% of the particle substances of cigarette smoke, such as nicotine and tar, converting those into water vapor and carbon dioxide. According to the research team, the air-cleaning equipment containing the newly-developed catalyst can purify over 80% of the cigarette smoke within 30 minutes and 100% of it within one hour in a 30 square meter room in which ten people are smoking simultaneously.

According to the KIST research team led by Drs. Jongsoo Jurng and Gwi-Nam Bae, research was conducted in cooperation with the Korean tobacco company, KT&G, to develop a nano-catalyst filter coated with a manganese oxide-based nano-catalyst for use in designated smoking areas to reduce and purify the major harmful substances in cigarette smoke.

Activated charcoal-based filters have been the most commonly used equipment in smoking areas to remove the gaseous materials in cigarette smoke. However, these filters are not effective in removing gaseous materials such as acetaldehyde, since their absorbtion performance

decreases rapidly in a closed facility, such as a smoking room, and they need to be replaced at least every other week, which is inconvenient.

The nano-catalyst filter was developed by evenly coating a manganese oxide-based (Mn/TiO_2)) nano-catalyst powder onto ceramic-based filter media. The nano-catalyst filter uses a technology that decomposes elements of cigarette smoke using oxygen radicals, which are generated by decomposing ozone in the air on the surface of the manganese-oxide-based nano-catalyst filter. An evaluation test with total volatile organic compounds (TVOC), in this case, acetaldehyde, nicotine and tar, was conducted to evaluate the performance of the newly-developed catalyst. The results showed that the new catalyst decomposes over 98% of these harmful substances.

Commercialization of this technology is expected to take about a year. As described by the lead researcher, Dr. Jurng, "This research is significant since the new air cleaning equipment based on a simple catalyst successfully processes and removes gaseous materials in cigarette smoke, which are not easily removed with existing air cleaning technologies. If the new equipment can be simplified and is economically feasible, it will be an important tool for keeping smoking rooms pleasant and clean. Also, from a convergence perspective, the new nanometer catalyst filter can be integrated with other air-cleaning products, such as air purifiers and air conditioners."
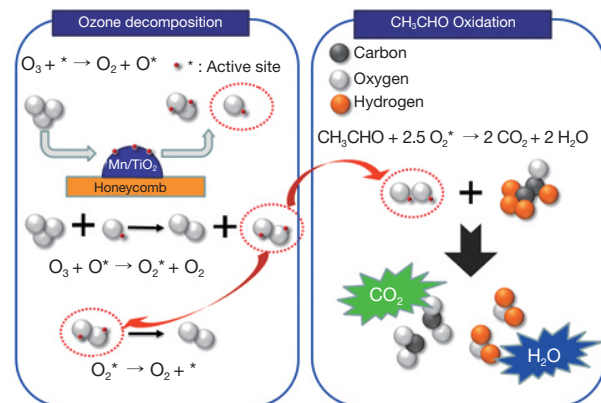
2. KIST Preparing to Launch Robotic Technologies in the Chinese Market
June 4, 2015

On June 4, KIST entered into an MOU with the Shanghai Industrial Technology Institute of China for the purpose of conducting R&D on robotic technologies and commercializing research results. With this agreement in place, KIST can prepare to introduce its robotic technologies to the Chinese market. The MOU marks an important step in Korea's push to expand its presence in

global markets in future technologies.

The Shanghai Industrial Technology Institute was established to promote the commercialization of scientific research results, and consequently, has expertise in the formulation of strategies for industrial technology development and technology dissemination.

Robotic technology is a priority research area at KIST. Earlier this year, KIST established the Robot & Media Research Institute to facilitate its intensive effort to develop robotic technologies. In fact, KIST's source technologies related to smart robots have already been applied to commercial products launched in the domestic market and Europe.

3. KIST Europe Researcher Receives Lifetime Achievement Award at the 2015 European Inventor Award Ceremony
June 11, 2015

Professor Andreas Manz, head of the microfluidics research group at KIST Europe, received a lifetime achievement award at the European Inventor Award ceremony held in Paris on June 11.

The European Inventor Award is an annual awards process held by the European Patent Office which recognizes inventions contributing to social development, technological progress and economic growth. Winners are selected out of a field of more than 300 candidates. Awards are handed out in five categories of which the lifetime achievement award is presented to a European inventor whose dedicated efforts over a long period have

had a major impact on his/her field of technology and society at large through patented landmark inventions.

This year, the European Inventor Award ceremony was held at the Palais Brongniart in Paris. During the awards ceremony, each candidate's accomplishments and a snapshot of their lives were introduced in short video clips. Prof. Manz was named the winner of the lifetime achievement award and received a sail-shaped trophy, emblematic of exploration and the way human ingenuity leads to new frontiers.

Prof. Manz was chosen in recognition of his contributions applying the lab-on-a-chip technology to analytical chemistry and bio-science. He is one of the pioneers in the area of applying micro chip technology to chemistry and was the one who coined the term, "Lab on a Chip." Prof. Manz is a recognized authority in the field of chemistry. In February 2011, *Science Watch*, the on-line weekly science magazine of Thomson Reuters (http://sciencewatch.com/), ranked Prof. Manz 48th out of the top 100 scientists of the world. He also received the Khwarizmi International Award in Iran in March this year. The European Inventor Award was yet another acknowledgment of his outstanding achievements.

Following this latest award, Prof. Manz commented, "Even though I am Swiss, I am even more pleased that my research work at KIST Europe, which is a Korean research institute in Germany, was recognized. I hope this award will become an opportunity to invigorate joint research between Korean researchers and the researchers at KIST Europe."

4. KIST Science Camp Helps Students Find Career Paths
July 20-31, 2015

Students choose career paths and prepare for the future during their high school years. For those who are interested in science, a peek into the daily lives of researchers can help them better understand the kind of work in which they may be involved someday. KIST's "Science Camp for High School Students" provides students with opportunities to experience research work in various fields firsthand.

This year's science camp was held on KIST's main campus in Seoul. Activities focused on five areas of science: brain science, life science, physics, robotics and chemistry, with the program for each area lasting one or two weeks. The programs involved attendance at lectures given by researchers, followed by discussion sessions and hands-on experience in conducting tests. At the closing ceremony on July 31, students from the five program areas shared their thoughts and experiences so that all students who participated in the program could hear about all the other areas of science covered in the camp.

Jae-Hyun Ok, a student from Yangjeong High School who attended the robot program said, "It was fascinating that I could see and experience things here that I can't elsewhere. Most of all, this science camp helped me a lot in making up my mind about what I will study in university and my further career path."

Jae-Cheon Ryu, a senior researcher at the Center for Environment, Health and Welfare Research who led the life science program said, "It seems students these days feel a vague fear when they think of their futures. During the science camp, I tried to be their mentor as well as pass on knowledge about science. The students who participate in the program have a high level of knowledge and strong passion for research. For me, as a researcher participating in the program, this is a very useful experience too."

KIST's president, Byung Gwon Lee, reflected on the program by saying, "I hope this camp program will be a good opportunity for high school students to explore careers and find ways to become next-generation scientists. Going forward, KIST will continue its efforts to maintain close communication with people by organizing various events to encourage an understanding of science."

5. KIST Offers an Interdisciplinary Program in Science and Medicine for Medical Students
August 6-8, 2015

KIST's Biomedical Research Institute hosted the 5th annual KIST-KMSA Research Camp in conjunction with the Korean Medical Student Association (KMSA) from August 6-8 at KIST's main campus in Seoul. More than 70 medical students from KMSA participated in the research camp to gain hands-on experience in a field of their choice selected from seven research areas identified by KIST. KIST researchers introduced research initiatives in each field and students went through in-depth studies on the chosen subject. The research areas included: surgical robotics, rehabilitation robotics, bio materials, theragnosis, basic brain science, brain medicine, and micro medical devices.

In addition to research activities, diverse lectures and discussion programs were offered at the camp to provide students with insights on biomedical engineering and facilitate cooperation between medical and engineering colleges. A lecture on interdisciplinary research in

medicine and engineering was provided by Dr. In San Kim, a researcher at KIST's Biomedical Research Institute. Before joining the institute, Dr. Kim was an instructor at the Medical College of Kyungpook National University.

Dr. Ik Chan Kwon, head of the Biomedical Research Institute, commented, "These experiences in convergent research fields represents an opportunity for future leaders in the medical sector to strengthen their interest in basic science." He added, "I hope the program will contribute to building closer ties between the medical and science sectors and encourage sustainable research efforts in the field."

6. KIST Expanding Cooperation with KT in Research on Disaster and Safety Management
September 14, 2015

KIST, in partnership with KT Corporation (formerly Korea Telecom), is set to build research cooperation and implement joint projects on disaster and safety management. The two parties agreed to implement demonstration and pilot projects to formulate disaster and safety management policy and develop core technologies in the field. This agreement was formalized in an MOU signed on September 14 by Tae Hoon Lim, Vice President of KIST, and Yun Kyung Lim, head of the Future Convergence Business Division of KT.

Under the terms of the MOU, KIST and KT plan to expand research cooperation on joint projects, share research equipment and facilities, provide for human resource exchanges and conduct joint seminars. Specifically, cooperation will be strengthened in the field of disaster and safety management, an area targeted by the Ministry of Science, ICT and Future Planning as a promising future core technology.

The two parties will jointly coordinate private, public and research cooperation through the entire cycle of core technology development including commercialization. KIST's sensing technology for disaster detection will be tied to KT's IoT platform and equipment. The two parties will also develop disaster forecast simulation, leveraging cloud and Big Data, and implement demonstration and pilot projects involving the convergence of science and ICT.

Tae Hoon Lim, Vice President of KIST, provided this comment on the agreement, "Cooperation with KT, the leader in the IT sector with the strongest infrastructure, will give KIST an opportunity to connect its disaster sensing technology to a new business field including IoT, and it is expected to contribute significantly to public safety as well as further advancement of the two parties." KT's Yun Kyung Lim added, "With the convergence and cooperation of KIST's technology expertise and KT's ICT technologies, including platform and Big Data, we will make every effort to respond to the needs of public safety and future changes by improving core technology at the fundamental level."

Brain Science Institute

Background

The foundation of the Brain Science Institute in 2011 was the first step taken by KIST to shift the organization of its research away from self-contained individual areas of study toward convergence research based on research themes. Researchers from different backgrounds, such as biology, physics, chemistry, psychology and engineering, work together to carry out convergence research for the common goal of identifying brain circuitry controlling the mind and behavior, thus developing technologies to help improve brain functions.

The establishment of the Brain Science Institute was the natural outcome of KIST's continuous support for brain science and its outstanding researchers. KIST hired talented researchers, such as Dr. Hee Seop Shin from POSTECH in 2002, and founded the Neuroscience Research Institute as the first Center for Excellence in 2005. Then in 2009, the Functional Connectomics Center was established as part of the World Class Institute Project (WCI). This center drew a number of brain scientists from around the world, including Dr. George Augustine who headed the center. As the result of such efforts, KIST was able to build a world-class brain research group in a short span of time.

These eminent brain specialists joined with medical researchers, chemistry researchers and micro system engineers at the Brain Science Institute, which was the first mission-oriented research institute. Until then, brain research had been conducted through individual or partial research activities. What sets the Brain Science Institute apart is the fact that it consists of four broadly-based research centers (Neuroscience, Functional Con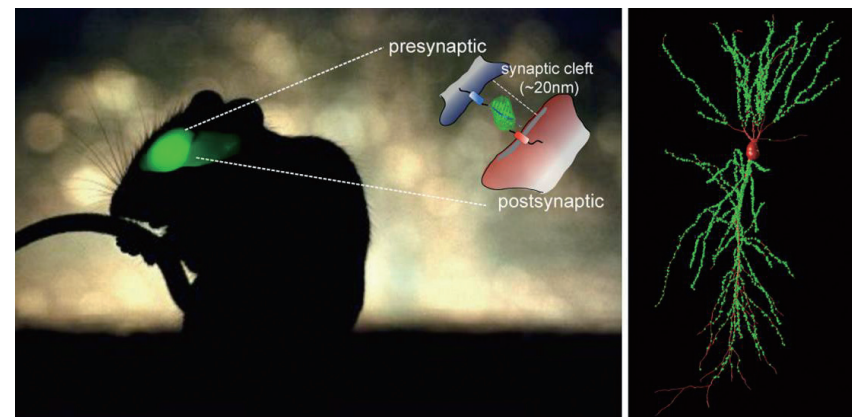nectomics, Neuro-Medicine, Bio-Microsystems) which can conduct convergent research based on a comprehensive understanding of the brain.

Director-General of the Brain Science Institute

Currently, the Brain Science Institute is headed by Dr. Dennis Choi who is a world-renowned expert in the field of brain medicine with a previous career in academics at Stanford University, University of Washington, and Emory University in the United States. He has also served as the chairman of the Neurosciences Institute and senior vice president at the research center of Merck. He is currently the chair of the Department of Neurology at Stony Brook University School of Medicine in New York. Director Choi spends two months each year in Korea, and during his absence, Dr. Dong Jin Kim steps in as deputy director-general, ensuring the stable operation of the institute.

Activities of each research center

The Center for Neuroscience carries out research on the interactions between neurons and glial cells, rather than neurons alone, in order to identify the functional mechanisms of the brain and mechanisms of brain diseases. The Center for Functional Connectomics studies functional brain circuitry based on optogenetics. The Center for Neuro-Medicine explores substitute substances after the treatment of brain diseases based on brain mechanisms and the brain map, and develops medicines. The Center for Bio-Microsystems develops MEMS-based bio-sensors and diagnosis systems related to brain diseases.

Key research outcomes

The research activities of the Brain Science Institute are primarily concentrated in basic and source technology research. The high quality of its research efforts have contributed significantly to the greater visibility and enhanced reputation of KIST. Every year, the institute's research outcomes are published in the so called "super journals" which include *Nature, Science*, *Cell* and their sister journals. 27 research papers originating from the work of the Brain Science Institute were published in these journals between 2011 and 2014. Examples of these articles include: "Observational fear learning involves affective pain system and Cav1.2 Ca2 channels in ACC" (*Nature Neuroscience*, 2010), "Bidirectional modulation of fear extinction by mediodorsal thalamic firing in mice" (*Nature Neuroscience*, 2011), "Channel-Mediated Tonic GABA Release from Glia" (*Science*, 2010) and "mGRASP for mapping mammalian synaptic connectivity with light microscopy" (*Nature Methods*, 2012). This last article was chosen by The Korean Federation of Science and Technology Societies as the best out of the top ten science and technology news items in 2012.

Meanwhile, the Brain Science Institute has carried out research on the early diagnosis of Alzheimer's disease by using blood tests as the open resource program (ORP) and will soon unveil tangible results. Its researchers have already completed the development of a technology to diagnose "beta-amyloid," a protein causing Alzheimer's disease, through blood tests, and the institute is currently in negotiations with interested companies over transfer of this technology.

In recognition of its excellent research outcomes and capabilities,

the Brain Science Institute received the Presidential Award as part of the Creative Science Technology Award process in 2013. Three outstanding researchers recruited for the WCI project in 2012, Bradley Baker, Sebastien Royer, and Keiko Yamamoto, were made regular employees, a reflection of the global nature of the research institute.

Next steps

The 20th century was the age of the human genome, and the 21st century is anticipated by many experts to be the age of the brain. More and more people are being diagnosed with brain illnesses such as depression, and populations are aging so the incidence of dementia and other age-related brain changes is on the increase. Therefore, finding fundamental solutions through brain research to combat brain diseases is of critical importance for societies worldwide as well as the scientific community. The importance of brain research is widely recognized, as evidenced by the global trend among advanced countries of investing heavily in brain research, such as the BRAIN Initiative (U.S.) and the Human Brain Project (EU).

Going forward, the Brain Science Institute will focus on research which can offer solutions for social issues. Through goal-oriented convergence research, it will explore uncharted areas of brain science and work on practical outcomes, thereby making contributions to improve the lives of people in Korea and elsewhere.

Researchers at the Brain Science Institute currently use mice for research, but will soon start using primates to develop new medicines for brain illnesses. The institute has entered into an agreement with the Jeonbuk Primates Test Headquarters of the Korea Institute of Toxicology in order to develop cures for brain diseases through tests on monkeys, and will embark on the development of treatments for Parkinson's and other major brain diseases.
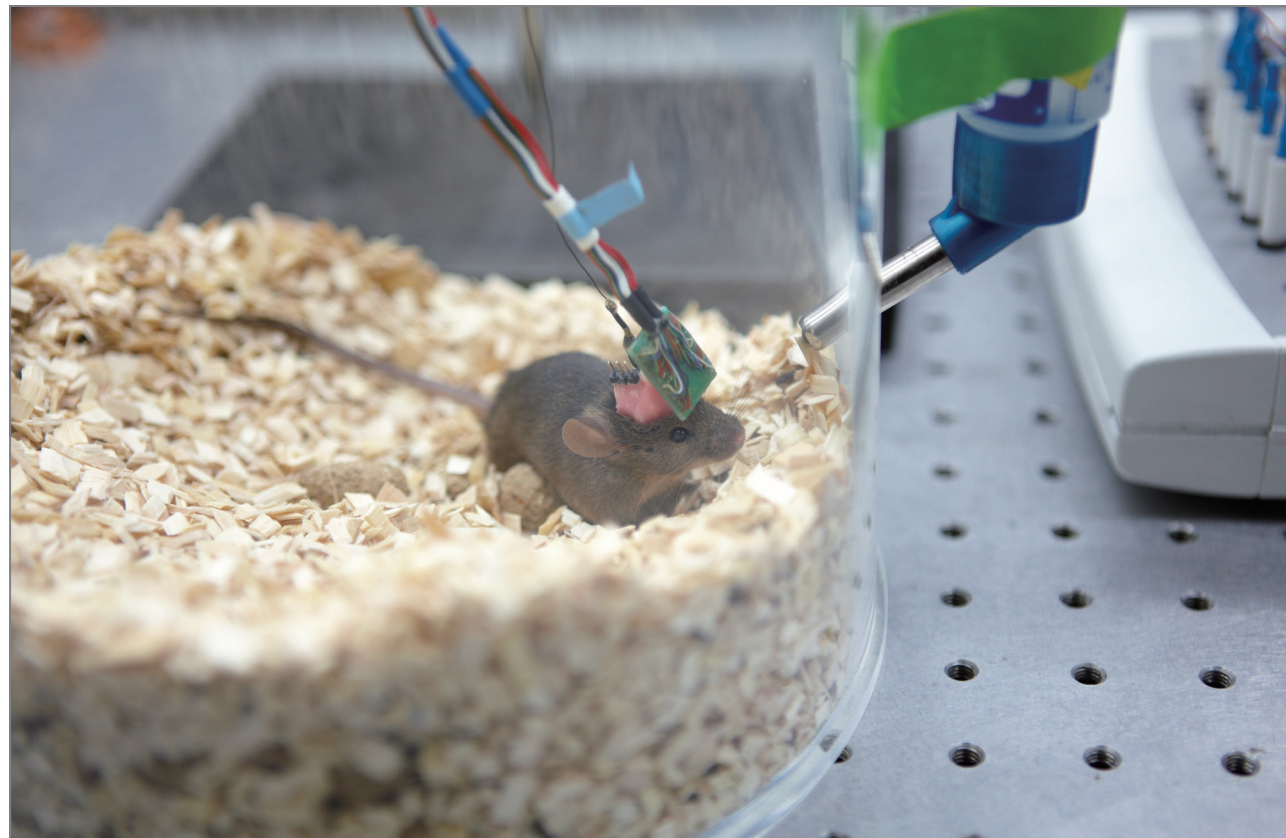
Joonyeon Chang
Director-General

Post-Silicon Semiconductor Institute

Q1 **The Post-Silicon Semiconductor Institute was founded in January 2015. The post-silicon semiconductor industry is based on a new technology widely considered of key importance to future economies. What was the background behind its establishment and what changes are apparent so far?**

I understand the concept of a "post-silicon semiconductor" may be somewhat vague, so I will use an example I am fond of relying on when explaining it to non-experts. Have you heard of the world's first-ever computer "ENIAC," which was developed in 1946? It was composed of 18,000 vacuum tubes the size of a small 100ml bottle. It weighed 30 tons, with a power consumption of 150kw, and was the size of a locomotive. Two years later in 1948, Bell Labs, based in the United States, developed a transistor using germanium (Ge) semiconductor material, which was substituted for the vacuum tubes. Afterwards, according to Moore's Law, the size of silicon semiconductor devices was reduced by half every 18 months, and today has reached a size of only 20 nanometers. We now use chips that integrate about one billion fingernail-sized transistors in our cell phones, which enable us to do just about everything we want today - whenever and wherever. By comparing the size of the computers, you will understand just how much tinier they have become. But how small do you think we can make a silicon semi-conductor? Experts estimate that about 10 nanometers will be the limit. In other words, it cannot be made smaller than that. The silicon semi-conductor will, within a few years, reach its limit in size, but experts have long wondered whether our desire to make it smaller and faster will stop there – or will a new technology for

exceeding this fundamental limit be developed? From an economic perspective, the silicon-based semiconductor industry is a major industry for Korea, acting as the driving force behind its economic growth. Therefore, the limits inherent in silicon semiconductor technology will have a direct impact on the country's economy. This is why the development of a new "post-Si" semiconductor technology is extremely vital and could determine the future of the country.

I apologize for getting carried away, but the Post-Silicon Semiconductor Institute was founded to create a core new growth driver which will play a pivotal role in Korea's economic growth by developing new semiconductor materials and devices to substitute for silicon semiconductors that are reaching their limit. Fortunately at KIST, various research teams have been devoted to developing post-silicon semiconductor technologies for many years, and as a result, KIST has managed to develop several excellent core and element technologies that can be proudly presented to the world. Against this background, we are trying to accurately forecast changing technology trends and take on the challenge of developing a new semiconductor technology based on convergence research, an area in which KIST excels. We intend to create a large-scale flagship project based on the capabilities of our young and talented researchers and develop significant source technology which will be industrialized. With the foundation of the Institute, we will move away from individual, divided research, and by gathering together researchers from various fields and adopting a practical approach, we will move toward a common goal of developing post-Si semiconductor technology. This is the greatest change we have instituted since the foundation of the Institute. The technology which developed from vacuum tubes to semiconductors over some 60 years brought monumental changes. Today calls for a second phase of technological innovation, and we intend to be its leader.

Q2 Can you tell us about the Institute's vision, the areas on which future research will be focused, and the research process?

Our vision is to lead in the development of next-generation semiconductors and innovative devices/materials for information processing and storage. To achieve this, we are trying to develop a post-Si semiconductor device using compound III-V semiconductors whose physical characteristics are superior to silicones.

We plan to acquire epitaxial growth technology which faultlessly integrates compound semiconductors on a silicon wafer, and by using this technology, we will focus on developing new electric devices that can process and store information and photoelectric convergence devices to connect devices optically, a process which involves less heat loss and faster information delivery. This research will require researchers associated with other research groups to open their doors to provide necessary elemental technologies, and thereby work together to achieve a common goal.

Additionally, we are working on developing wearable electronic devices as a convergent research task at the Institute. Future information devices are moving from being "portable" to being "attachable." Based on this, we are trying to develop electronic devices for healthcare that are flexible and harmless to the human body. We expect that collaboration by researchers in various fields will facilitate commercialization within a few years. In the case of research fields closely connected to industrial enterprises, our goal will be to achieve technology transfer ahead of time through the development of practical next-generation information electronic materials/devices, and for fields more focused on basic sciences, we will deepen expertise and promote world-leading research groups that will discover new scientific facts. Out of our basic science research, we will develop new source technology for which we will acquire intellectual property, thus enabling
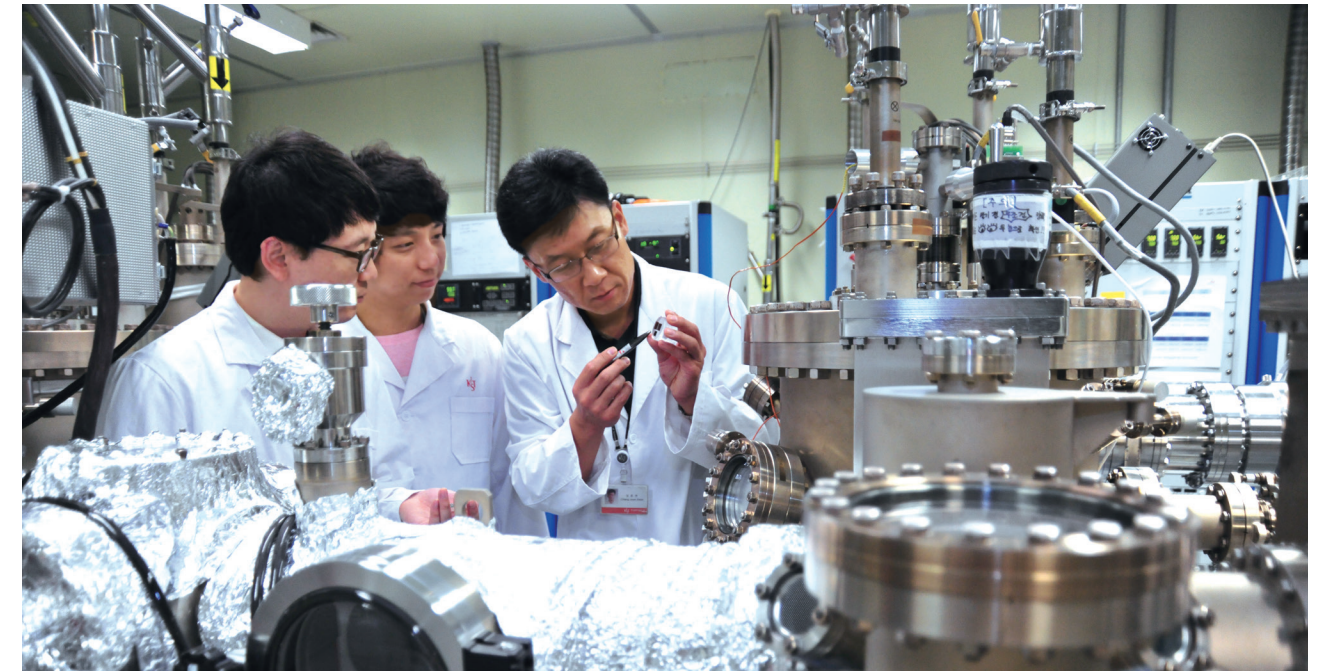
industrial technology research for the development of original, leading technologies. In this way, we will acquire technological leadership in the field of next-generation semiconductors.

At the heart of the Institute's research process is the construction of a complementary and efficient system which covers the entire cycle of research. Many of our researchers specialize in materials. Before the Institute was founded, they mainly conducted research to maximize the capability of the materials they were specializing in and had little interest in materials being researched by others. However, we are trying to develop next-generation electronic devices, which can only produce superior characteristics when various materials and processes and measurement technologies are effectively connected and optimized. Therefore, our researchers are now required to take an interest in other materials and technologies and consider how to effectively connect their own work to that of others. They will establish optimized detailed qualifications of each material and unit technology to suit the requirements of the next-generation electronic device and conduct complementary and comprehensive

research to achieve it. In other words, they will move from independent materials research toward collaborative research benefiting system goals. Furthermore, we will systematically manage the entire process of research and development, from materials development to optimal processing, development of assessment technology and next-generation electronic devices so that we can build an efficient research process where feedback can be interactively delivered to the results of each phase.

Q3 KIST adopted a special research system in 2011 so that its organization could be more duty-focused in order to conduct convergence research. It is now a leader in this type of operational management. This special research system grants broad discretionary authority to its chief for budget and human resources management, among other areas, creating an autonomous management system for each of the different institutes. What is your main focus in operating your Institute?

We believe the special research institute system is definitely an attractive system for researchers as it enables researchers in similar fields to establish a detailed and clear goal towards which they can work together in their research, while also being granted autonomy. The director-general is endowed with a great deal of discretionary authority, which represents a heavy personal responsibility. The Institute is still in its early stages, so sensitive details, such as research costs and personnel issues, still need to be determined. However, my basic principle is to exercise my authority, to the extent possible, to create an environment where the members of our Institute can intensively and enjoyably concentrate on their research. In particular, I will always try and remember my original intentions and take into consideration, as much as possible, what I personally felt as a researcher myself. In carrying out internal research projects, one researcher will undertake one or two tasks – this will be flexible. Developing a semiconductor device requires the integration of varying element technologies and materials. Therefore, we will deepen expertise in each field by conducting future source technology projects, and develop a system for flagship projects through collaborative research. Researchers undertaking two projects will be required to spend 50 percent or more of their time on flagship projects, while researchers devoted only to flagship projects will be encouraged to voluntarily participate. There are currently six researchers, and this number will eventually grow. In operating the Institute, I place the greatest value on communication. In coming up with flagship projects for the Institute, researchers from different fields will collaborate and participate in intensive brainstorming. They will first select four projects for which detailed plans will be established, and ultimately one flagship project will be selected. I believe sufficient communication and exchange of views are vital for researchers used to working independently to collaborate and produce outstanding results.

Q4 You were the first in the world to develop a spin transistor device by using the spin of an electron, which, for twenty years, had remained only a theoretical concept. With this achievement, you opened the way for the development of ULSI transistors. In 2013, you developed the world's first complementary logic device using spin injection, which integrates various functions on a single chip to minimize size and power consumption and can operate at room temperature. As an expert in next-generation semiconductors, what is your opinion on future research trends and the direction of development in research?

Developing the spin transistor and logic device using spin injection and announcing strong theses was a great honor for me. My seniors had set the goal, and all I had to do was strive towards that goal with all my might. In both cases, we were the second mover. They were such difficult research themes that when we began our research, leading research groups had already started to move away from these topics because they had not panned out. Looking back on it now, perhaps we were somewhat reckless for having started at such a phase, or maybe we were brave because we had so little knowledge of them. (Laughter) I remember that in his memoir, the founder of POSCO, Park Taejoon, said that during the early days when they worked to construct a steel mill, a project requiring a huge investment of capital and technology, all of POSCO's executives and employees worked with such fierce determination that they would have turned towards the sea and thrown themselves into
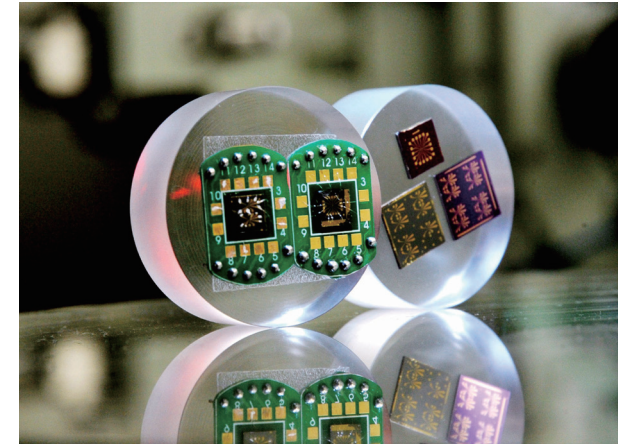
the waters of Youngil Bay if the construction had failed. The way we threw ourselves into our work reminded me of his words. Our research team worked extremely hard for a long time, and finally, we managed to develop the world's first spin transistor. I still cannot express the overwhelming joy I felt at the time. It was a major turning point in my research career.

In regards to my latest research project to develop the next-generation semiconductor, I believe I am in a better position than I was when attempting the development of a spin transistor device. The development of post-Si semiconductor devices/materials will act as a bridge between next-generation semiconductor technology, including spin devices, and today's silicon semiconductor technology. Advanced countries are competing with great intensity to acquire technological leadership in the post-Si era. Research by Intel (U.S.) and IMEC (Europe) on electronic devices using InGaAs (n-MOS) and Ge (p-MOS) has almost been completed. However, these technologies use materials with different n-types and p-types, which make it difficult to produce in large quantities – a fatal weakness. In contrast to other leading research groups, we are pursuing a technology which will make a quantum leap from the current level of technology using a different method. Our winning move will be made with new materials and world-standard epitaxial growth technology which only we possess. This may be likened to the Incheon Landing Operation during the Korean

War. (Laughter) Jesus del Alamo, an MIT professor and global scholar in compound semiconductor devices, with whom we maintain a close relationship through our overseas laboratory at MIT, has a great interest in our III-V compound semiconductor research, and we exchange views on research trends. We intend to achieve a major breakthrough with a greater focus on materials rather than devices. If we can achieve the research results that we anticipate, we will be able to shape a new industry which can lead not only memory devices, in which Korea excels, but also logic devices markets led by Apple and Intel, just as Bell Labs ushered in a new era by developing a semiconductor the size of a fist using silicon for the first time in the world.

Q5 In the post-silicon semiconductor field, it is imperative to cultivate and dominate new markets. In order to achieve this, actual research results must be applied in an industrial setting so that they can be commercialized. Cooperation with business is even more important in order to mass produce the results of research. What is necessary or must be improved in order to make research outcomes in next-generation semiconductor fields commercially successful?

As we prepared to launch the Institute, we visited major semiconductor businesses several times to exchange views on the technologies and capabilities they need. Although these businesses employ thousands of researchers, they are so focused on manufacturing process technologies to maximize efficiency and profits that they rarely think about next-generation semiconductor research, which would be a way of preparing for the future. They even confessed that when a problem occurs, they have to find the source in order to come up with a solution, but do not have the capacity to do that either. Furthermore, when growing a thin film of compound

semiconductor on a silicon wafer, the distance between atoms of the two materials differs and inevitably leads to defects in the interface. Thus, there is a large demand by companies to develop a methodology to analyze these defects and develop a standard on how many are acceptable in order for the device to operate normally. KIST has the capability to not only conduct analysis but identify the source of an issue, so we can research fields that are vital to business, and by coming up with results, we can build mutual confidence. Once the KIST Post-Silicon Semiconductor Institute offers help to businesses, and they cooperate closely through this kind of process, I believe their interest in post-Si next-generation devices will increase. We possess the know-how and experience in III-V compound semiconductors, and therefore, I think we can take on a leadership role in acquiring future source technology in areas in which businesses cannot.

materials from the bottom up. We believed we would achieve a breakthrough if we used such different materials to produce what our incumbent researchers do best – spin devices. This was how we got started, and it turned out that we were right. The results were outstanding, and we managed to acquire numerous patents at home and abroad and even announced our theses in leading journals. Based on this source technology, we are thinking of a spin-off project involving cooperation with industry. This new material is transparent and flexible, and its conductivity can be freely modified, so we plan to utilize it as a core material for wearable electronic devices or organic compound sensors, which are difficult to measure using existing methods. As such, in order to create something new, it is imperative that we think outside the box, accept the new, and develop it through convergence and cooperation.

Q6 As the former chief of the Spin Convergence Research Center (SCRC), you decided to use a researcher without experience in the spintronics field to innovatively enhance semiconductor capability. Discovering such innovative methods increasingly requires convergence and cooperation. What is your opinion on the importance of convergence and cooperation?

I would like to elaborate on the convergence research I conducted at the SCRC. We had the chance to recruit a new researcher, and instead of recruiting someone in spin devices, we deliberately hired a researcher who worked with material that we did not cover. In order to produce innovative methods and results, we needed original ideas and new approaches from researchers in various fields. There was also a researcher at our center who went to study abroad for a degree and conducted exciting research on using bio technology to alter the nature of a virus and develop semiconductor or electric conductor

Q7 What are your ambitions and plans for 2016?

I have worked at KIST for many years, but I believe that 2016 will be an especially meaningful one. Before, my job was to do my best as a researcher, but as the director-general of the Institute, although it has not been long since I took on this role, my work has changed drastically. I am very excited, just like I usually am when I start a new project. The Post-Silicon Semiconductor Institute has been launched, and under an energetically set up banner, it has taken its first steps towards a grand adventurous journey. I feel it is extremely important that I try and stabilize the staff and organization of the Institute as quickly as possible and set goals with appropriate research projects for us to carry out so that we can operate smoothly. To achieve this, I will strengthen communication among our staff members and focus on removing barriers between different research divisions. I ask for your continued interest and support as we go forward.
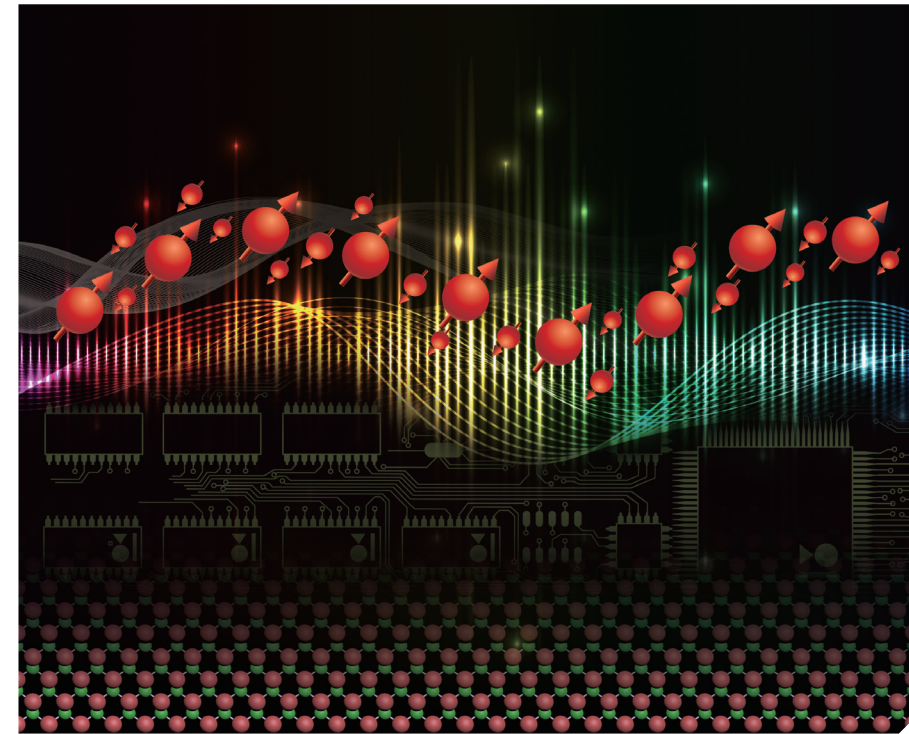
◀ Cover image :
We have developed electric field-controlled spin devices using the ballistic spin Hall effect. The ballistic spin Hall effect can be used as both spin injector and detector without spin relaxation.